OPTIMAL DESIGN OF GEODESICALLY STIFFENED COMPOSITE CYLINDRICAL SHELLS

by

Guy Gendron

Dissertation submitted to the Faculty of the

Virginia Polytechnic Institute and State University

in partial fulfillment of the requirements for the degree of

DOCTOR OF PHILOSOPHY

in

Engineering Mechanics

APPROVED:

Z. Gürdal, Chaiman

O. H. Griffin Jr.

R. T. Haftka

E. R. Johnson

D. T. Mook

J. N. Reddy

September 1991

Blacksburg, Virginia

OPTIMAL DESIGN OF GEODESICALLY STIFFENED COMPOSITE CYLINDRICAL SHELLS

by

Guy Gendron

Committee Chaiman: Z. Gürdal

Engineering Mechanics

(ABSTRACT)

An optimization system based on the finite element code CSM Testbed and the optimization program ADS is described. The optimization system can be used to obtain minimum-weight designs of composite stiffened structures. Ply thicknesses, ply orientations, and stiffener heights can be used as design variables. Buckling, displacement, and material failure constraints can be imposed on the design. The system is used to conduct a design study of geodesically stiffened shells. For comparison purposes, optimal designs of unstiffened shells and shells stiffened by rings and stringers are also obtained. Trends in the design of geodesically stiffened shells are identified. An approach to include local stress concentrations during the design optimization process is then presented. The method is based on a global/local analysis technique. It employs spline interpolation functions to determine displacements and rotations from a global model which are used as "boundary conditions" for the local model. The organization of the strategy in the context of an optimization process is described. The method is validated with an example.

ACKNOWLEDGEMENTS

The author whishes to thank Dr. Zafer Gürdal of the Engineering Science and Mechanics Department, Virginia Polytechnic University and State University. He also wishes to thank the members of his committee for their assistance and willingness to support and review this research. The author is grateful to the National Aeronautics and Space Administration for their financial support (Grant NAG1-643). The financial support of the Fonds pour la Formation de Chercheurs et l'Aide à la Recherche, Gouvernement du Québec, Canada, is also gratefully acknowledged. For many useful discussions and her technical assistance, the author is indebted to Mrs. Christine G. Lotts of the Computational Mechanics Branch at NASA Langley Research Center. The suggestions and technical assistance of Mrs. Caroline Stewart in producing this manuscript are acknowledged. The author also wants to thank the personnel and students of the Engineering Science and Mechanics Department for their assistance and friendship. Most of all, I wish to thank my wife, Céline and my son, Philippe, for their "sportsmanship" and moral support.

TABLE OF CONTENTS

LIST OF TABLES

LIST OF FIGURES

LIST OF SYMBOLS

$\mathbf{0}$	Null vector
$\mathbf{a}$	Vector of unknown spline coefficients of the interpolation function
$\mathbf{A}$	Vector of components of $\mathbf{R}$ that must be added to form F_a
b	Field being interpolated
$b_{g/l}$	Interpolated values of the field
b_i	Known values of the field being interpolated
BCi	Set of boundary conditions
d_r, d_s	Distances between the rings and the stringers, respectively
E_1, E_2	Material properties in the principal material
G_{12}, G_{23}, ν_{12}	directions
f	Objective function
$\mathbf{f}$	Load vector
F_a	Load applied to the model
F_d	Design load
$\mathbf{g}_b$	Buckling constraints
$\mathbf{g}_d$	Displacement constraints
g_k	Inequality constraints, $k = 1, 2, \ldots, n_g$
$\mathbf{g}_f$	Material failure constraints
h_g	Height of the spiral stiffeners
h_k	Equality constraints, $k = 1, 2, \ldots, n_h$
h_s	Height of the stringers
$\mathbf{K}$	Stiffness matrix

h_r	Height of the rings
$\mathbf{K}_G$	Geometric stiffness matrix
l_{ne}	Number of elements along the height of the stiffeners
L	Lenght of the cylindrical shell
m	Degree of the spline functions
m_{ne}	Number of elements along the length of the cylinder
n	Number of design variables
nncs	Number of nodes in the coarse mesh discretizing the interpolation region
nnrs	Number of nodes in the refined mesh discretizing the interpolation region
n_b	Number of buckling constraints
n_d	Number of displacement constraints
n_h	Number of equality constraints
n_{ne}	Number of elements along the circumference of the cylinder
n_p	Number of material failure constraints
N	Number of cells in the circumferential direction
N_x	Longitudinal stress resultant
N_{xy}	In-plane shear stress resultant
N_y	Transverse in-plane stress resultant
p	Number of eigenvalues contained in a specified range
q	Number of points in the interpolation region
$\mathbf{P}_j$	Critical loads
$\mathbf{P}_{ref}$	Reference load
r	Number of critical constraints
R	Radius of the cylindrical shell
R	Static Reaction Vector
s	Scale factor

$\mathbf{S}$	Spline coefficient matrix
t_g	Thickness of the geodesic stiffeners
t_r	Thickness of the rings
t_s	Thickness of the stringers
t_θ	Thickness of the skin plies oriented at θ^o
$\mathbf{u}$	$< \mathbf{u}_u, \mathbf{u}_c >^T$
$\mathbf{u}_c$	Vector of boundary conditions
$\mathbf{u}_d$	Static displacement solution corresponding to the design load
$\mathbf{u}_{dc}$	Vector of boundary conditions corresponding to the design load
$\mathbf{u}_d^i$	First-order Taylor series approximation of the perturbed displacement vector
u_{dj}	Component of $\mathbf{u}_d$
$\mathbf{u}_{du}$	Vector of unknown displacements corresponding to the design load
$\mathbf{u}_j$	jth buckling mode
$\overline{u}_k$	Limiting value of the kth displacement constraint
$\mathbf{u}_{lc}$	Vector of boundary conditions in the local model
$\mathbf{u}_{lu}$	Vector of unknown displacements in the local model
u_r	Radial component of a nodal displacement
$\mathbf{u}_u$	Vector of unknown displacements
u_x	Axial component of a nodal displacement
u_θ	Circumferential component of a nodal displacement
$\overline{v}_k$	Limiting value of the kth buckling constraint
$\mathbf{x}$	Vector of design variables
Δx_i	Perturbation in the value of x_i
ϵ_j	Component of the engineering strains
$\overline{\epsilon}_k$	Limiting value of the kth material failure constraint

$\epsilon^c_{1,allowable}$	Strength Properties in the principal material
$\epsilon^t_{1,allowable}$	directions
$\epsilon^c_{2,allowable}$	
$\epsilon^t_{2,allowable}$	
$\gamma_{12,allowable}$	
γ	Angle between the stiffeners and the axis of the cylinder
λ	Lagrange multiplier
λ_j	Eigenvalues of the buckling problem
ρ	Material density
θ	Angle of lamination
θ_r	Rotation around the radial direction
θ_x	Rotation around the axial direction
θ_θ	Rotation around the circumferential direction

Chapter 1
Introduction

In the aerospace industry, the need for weight efficient structures has led to the adoption of the stiffening concept for many structural components. The use of stiffeners results in a significant increase of stiffness for a minimum amount of added material. In most metallic structures, stiffening is provided by an array of orthogonal or near orthogonal members fabricated independently of the skin and assembled with fasteners. With the advent of composite materials, designers have instinctively been using the same practice to stiffen flat and cylindrical panels.

However, various considerations, mainly related to the cost-effective manufacturing of composite structures, suggest that other stiffening concepts might be structurally as efficient and more economical to manufacture. In recent years, concepts that employ stiffeners following the geodesic lines (a geodesic line is the shortest line between two points that lies in a given surface) have been considered, and some examples of geodesically stiffened structures are shown in Fig. 1.1. The main advantage of this stiffening pattern, compared to more conventional arrangements, is that geodesically stiffened structures can be manufactured using the filament winding technique, a cost-effective process that offers enormous potential in terms of reductions in number of parts and fasteners. This is particularly true for aircraft fuselage structures which are large continuous cylindrical shapes that lend themselves particularly well to filament winding.

One variant of the geodesic stiffening concept that has received a great deal of attention in the case of composite structures is the "isogrid" pattern [1–2]. With this concept, stiffening is provided by an array of stiffeners that form equilateral triangles. Research on isogrid-stiffened configurations has shown that the multiple load paths resulting from

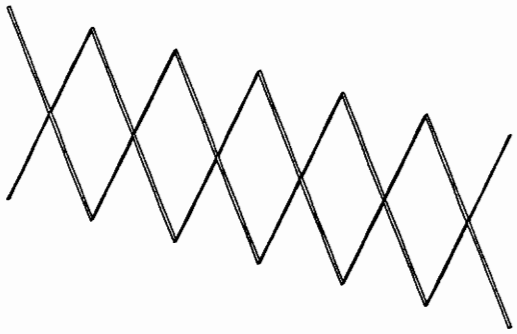

a – Open-web Truss.

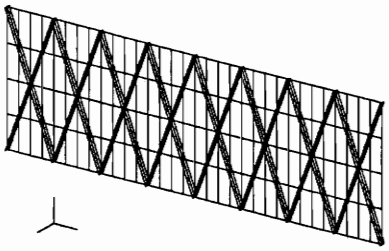

b – Flat Panel.

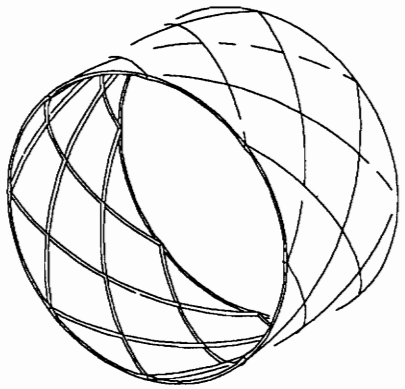

c – Cylindrical Shell.

Fig. 1.1 – Examples of Geodesically Stiffened Structures.

the redundancy of the stiffening create a highly damage-tolerant structure. Also, the equilateral triangular grid of stiffeners displays an overall isotropic nature. Therefore, many existing analytical solutions based on a smeared representation of the skin-stiffener assembly can still be used. However, it has been noted [2] that for certain applications, the uniformity of configuration and the isotropic stiffening may result in weight penalties. Hence, the need to study the geodesic stiffening concept which allows the stiffeners to intersect at an arbitrary angle. As such, this additional freedom provides the designer with more flexibility, while retaining all the benefits of the isogrid stiffening pattern in terms of structural efficiency, ease of manufacturing, and damage tolerance.

Although the geodesic stiffening concept appears promising, more work must be done to better measure its potential to become a valid alternative to the more traditional stiffening concepts. This is the subject of the present study which considers the optimal design of geodesically stiffened composite cylindrical shells. The overall objective of this work is to compare the efficiency of the geodesically stiffened concept to more traditional stiffening patterns in the case of aircraft fuselages. The specific goals are:

1. To develop a finite element based optimization system that can be used to design complex structural configurations such as geodesically stiffened shells subjected to combined loading conditions.
2. To characterize the structural behavior of geodesically stiffened cylindrical shells.
3. To obtain optimal designs for different unstiffened and stiffened shell configurations subjected to axial compression, torsion and a combination of compression and torsion.
4. To compare the optimal designs obtained with the different configurations, as well as identify trends in the design of geodesically stiffened shells.
5. To develop a methodology for the incorporation of local stress constraints into a design process.

The organization of the remainder of this dissertation is as follows. First, the configurations that will be considered in the present study are presented in Chapter 2 along with a review of the previous work that has been published on the analysis and design of geodesically stiffened shells. Then, in Chapter 3, the new optimization system that has been developed in the course of this research initiative is presented. Due to the complex geometry of the structures that are considered in the present study, the optimization system has been built around a finite element code. Until recently, the incorporation of this method into an optimization process was considered too expensive due to the large number of analyses required to achieve the optimal configuration. However, recent developments in the fields of structural optimization, numerical analysis and computer hardware, as well as the versatility of the resulting design tool tend to make this approach more and more attractive.

The presentation of the optimization system is followed in Chapter 4 by the description of the models that will be used in the design of the unstiffened, longitudinally and ring stiffened, as well as geodesically stiffened shell configurations that will be considered in the present study. For several configurations, the analysis of a nominal design is performed and mesh refinement requirements are investigated. Also, characteristics of the behavior of geodesically stiffened shells under static loading are highlighted. Then, in Chapter 5, the results of the design study are presented and used to identify trends and evaluate the efficiency of the geodesic stiffening pattern compared to the other configurations studied.

In Chapter 6, the modifications made to the optimization system presented to incorporate a global/local analysis strategy into the design process are presented and the resulting implementation is validated on an example. Results of the research work are summarized in Chapter 7, and concluding remarks are provided.

Chapter 2
Design of Geodesically Stiffened Shells

As mentioned in the introduction, the application of the geodesic stiffening concept to composite structural components results in a damage tolerant structure that can also be tailored and cost-effectively manufactured. To investigate the concept further and compare the efficiency of this stiffening pattern to more conventional stiffener arrangements, a detailed design study of a portion of an aircraft fuselage is performed. In Section 2.1, the geometry and loads for a typical aircraft fuselage are introduced. Previous works published on the analysis and design of geodesically stiffened shells are reviewed in Section 2.2. Finally, in Section 2.3, the scope of the present study is established.

2.1 Geodesically Stiffened Cylindrical Shells

The application of the geodesic stiffening concept to aircraft fuselages is promising. This is due to the automated filament winding process that can be used to cost-effectively manufacture such structures. The portion of the fuselage under consideration is similar to the section of a C-141 aircraft immediately after the wing box. The design of a fuselage is impacted by its functional as well as its strength, stiffness and life requirements. Loads due to flight maneuvers, cabin pressurization, and forces due to engines, fuel load, etc ... result in bending, twisting and membrane stretching of the fuselage structure.

For the present study, the fuselage is modelled as a circular cylinder of 100 in length and 170 in diameter. The cylinder incorporates a grid of integral blade stiffeners of constant rectangular cross-section. In view of the proposed manufacturing technique, which includes an automated winding process, the stiffeners are assumed to be composed of unidirectional material oriented along each stiffener axis. Because of aerodynamic

requirements, all the configurations studied are internally stiffened. Regarding boundary conditions, the actual degree of elastic restraint against edge rotation and expansion provided by the surrounding structure is unknown and no doubt complex. To provide realistic restraints, a ring of fixed dimensions (0.2 *in* thick and 1.5 *in* high) has been placed at each end of the cylinder. The role of the rings is to restrain the radial expansion and rotation about the circumferential direction. Further discussion of the specific boundary conditions used for each configuration and load case may be found in Section 4.2. Finally, the applied loads considered are uniform axial compression, torsion, and combined axial compression and torsion. All the loadings are introduced by specifying nonzero displacement boundary conditions for all the skin and ring nodes located at each end of the shell. Specifying the axial displacement of these nodes results in a considerable amount of rotational restraint with respect to the circumferential direction at each end of the shell.

Three configurations are considered for the fuselage: unstiffened shell, shell stiffened by rings and stringers (referred to as the "conventionally stiffened" configuration in the remainder of the present study), and geodesically stiffened shell. Because fuselage structures are typically made of a thin skin reinforced by stiffeners, their buckling resistance is a major concern. This is illustrated by several of the papers that are reviewed in the next section as well as by the design study results that will be presented in Chapter 5. The performance of the geodesically stiffened arrangement will be evaluated by direct comparison to the unstiffened, and conventionally stiffened shells. The terminology associated with the analysis and the design of stiffened shells is shown in Fig. 2.1.

2.2 Literature Review

In this section, papers published on the analysis and the design of geodesically stiffened structures are reviewed. Papers dealing with the analysis and the design of

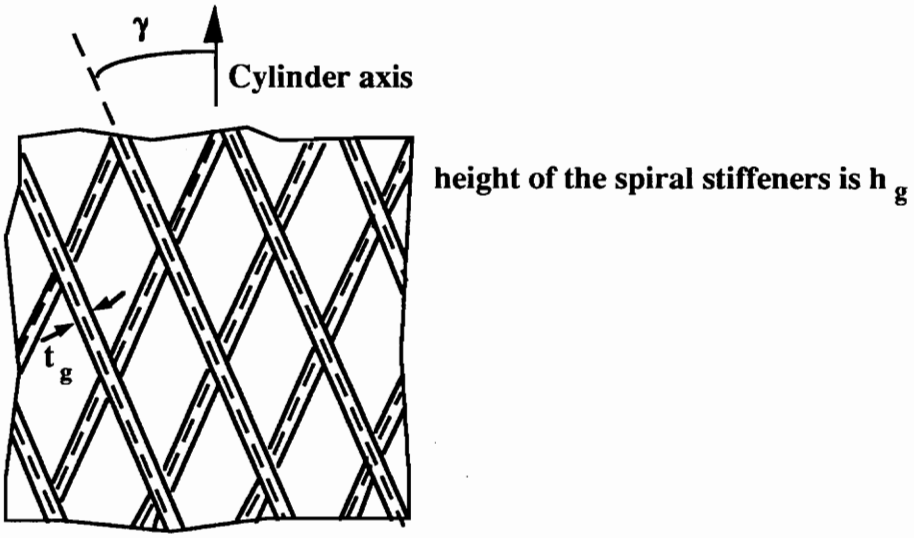

a – Geodesically Stiffened Shell.

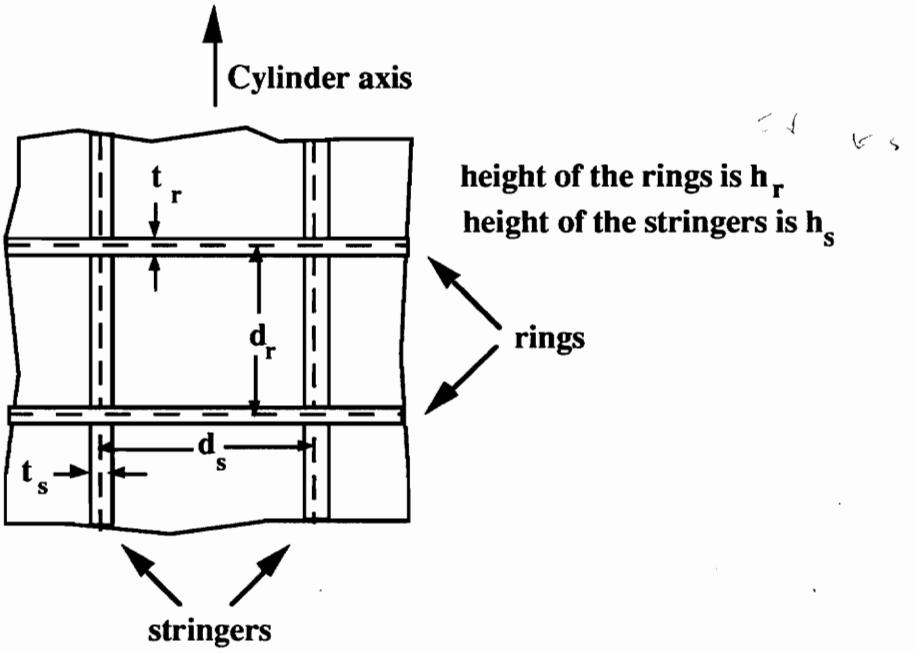

b – Shell Stiffened by Rings and Stringers.

Fig. 2.1 – Cylinder Configurations.

unstiffened and conventionally stiffened shells are not discussed here. Results of an optimal design of unstiffened cylindrical shells are given in Ref. [3]. A brief review of the vast literature on the design of stiffened shells is given by Gajewski and Zyczkowski [4] who also give an extensive bibliography on the subject.

To date, only a few papers have been published on the subject of geodesically stiffened shells. In many of these papers, simple computational strategies were used. For example, in Refs. [5–6], the properties of the stiffeners were averaged over the spacing so that the discrete nature of the stiffeners was neglected.

One of the earliest papers considering the geodesic stiffening concept is by Meyer [5] who studied 45° integrally milled-out stiffeners. The primary motivation for considering this type of stiffening was to exclude the buckling modes that occur between hoop reinforcements for ring and stringer stiffened shells. The material was isotropic and the stiffening was assumed to be continuously distributed over the shell reference surface. Test results were presented to verify the buckling loads obtained and no design study was performed.

In 1969, Soong [6] derived buckling equations for cylinders made of isotropic material and with stiffeners inclined at an arbitrary angle with respect to the axis of the shell. In his case, the primary motivation for the study was also related to the design of more efficient structures. In his formulation, discreteness of the stiffeners was also neglected. Several comparisons between conventionally and spirally stiffened shells using arbitrarily chosen dimensions were presented. Correlation of the theory with 12 test results for 45° stiffened cylinders under bending and compression was presented. Based on numerical results, the author concluded that, on equal stiffener weight or equal buckling strength bases, the spirally stiffened cylinders were about equally efficient compared to the ring and stringer stiffened cylinders for axial compression and pure bending loads. Under torsion and pressure loads, however, the spirally stiffened cylinders were superior.

Also in 1969, Lee and Lu [7] presented a study on the general instability of inclined-stiffened isotropic cylinders under bending. For the first time, the discrete nature of the stiffeners was considered. They showed that the optimum inclination varies with the rigidity of the stiffeners, and that theoretically, the buckling load should increase with the rigidity of these members. However, test data showed that the buckling strength increased little as the rigidity of the stiffeners became large. This discrepancy was attributed to imperfections in the more strongly stiffened cylinders which likely produced local rather that global buckling modes.

In 1970, Pappas and Amba-Rao [8] noted that although Soong's comparisons [6] may indicate correct trends, they were not based on minimum weight designs. Consequently, to allow for a more realistic evaluation of the different stiffener configurations, a mathematical programming method was used to compute optimal designs for isotropic ring and stringer stiffened shells as well as spirally stiffened shells. The shells were subjected to a uniform compressive loading and a lateral pressure. Skin and stiffener buckling were considered. Design studies performed using a shell length of 165 in and a radius of 60 in have shown that under pure axial compression, the optimal geodesic shell presents stiffeners that are inclined at an angle of 45°. In the case of hydrostatic pressure, angles of 90° were obtained, indicating that for this loading a ring stiffened shell corresponds to the optimum configuration. In all cases, spirally stiffened shells were inferior to shells with conventional-type stiffeners. The authors noted, however, that the superiority of a particular configuration will depend on the shell parameters, loading conditions and side constraints involved in the application, as well as on the nature of the stiffener cross section.

In 1980, Karmakar [9] used the same overall shell dimensions and properties that Pappas and Amba-Rao [8] used and performed a design study considering six types of stiffener configurations, including 45° internal and external spiral stiffening. The shell

was subjected to axial compression. Simple computational procedures that neglect the discrete nature of the stiffeners were used to predict buckling between circumferential stiffeners, local buckling of skin, local buckling of axial and spiral stiffeners, and yielding of the cylinder material. The results indicate that outside stiffened cylinders were lighter than their internally stiffened counterparts. For internally stiffened configurations, a combination of rings, stringers, and spiral stiffeners resulted in the lightest configuration followed by spiral type stiffening. Among all the stiffener configurations studied (being internally or externally stiffened), spiral type outside stiffening gave the lightest design. In all cases, stiffener spacing was considered as a design variable. In the case of spiral stiffening, the optimum stiffener spacing was around 1.4 *in* with no significant difference in the optimum stiffener spacing between internal and external stiffening.

As mentioned in the introductory chapter, in the case of composite structures, the utilization of geodesic stiffeners actually eases the manufacturing process compared to more conventional stiffener arrangements. Therefore, it was natural for the researchers to consider this type of stiffening in the search for efficient structural concepts. Rehfield and his co-workers [2,10] considered a variant of the geodesic stiffening called "isogrid" stiffening for the design of composite flat panels and cylindrical shells. Their stiffening concept used a repetitive equilateral triangular pattern of stiffening ribs. The name "isogrid" refers to the fact that the triangular grid behaves in a gross sense as an isotropic material. Therefore, simple computational procedures were used to predict the static and buckling responses of the stiffened structure. In their first paper [2], parametric studies based on such procedures were used to design a 20 *in* diameter, continuous filament advanced composite isogrid cylindrical shell. A quasi-isotropic skin of lamination sequence $[-60/0/60]_S$ was chosen and the stiffeners were made of unidirectional material. For the final design, obtained from an extensive parametric study, the skin was 0.030 *in* thick and the stiffeners were 0.058 *in* thick and 0.10 *in* high. The distance between two

stiffener intersections was 1.5 *in*. The critical buckling mode consisted of two longitudinal half waves and six circumferential full waves. In a second paper [10], the problem of determining the damage tolerance characteristics of composite isogrid structures was addressed. Since the stiffeners provide most of the bending stiffness, damage to these members was considered. Beams and flat panels were tested. As expected, due to the redundant nature of the isogrid concept, good damage tolerance characteristics were exhibited by the structures.

In Ref. [1], parametric design studies comparing the isogrid concept to other configurations that can also be manufactured using a filament winding technique were presented. Constraints on general instability, skin buckling, and rib crippling were considered. For general instability, constitutive relations for the stiffened shell were found by smearing out the stiffeners and representing the cylinder as a homogeneous shell. For local skin buckling, the inter-stiffener skin section was treated as an orthotropic triangular plate with simply-supported edges under in-plane loads. Finally, the buckling load for the ribs was estimated using an approximate formula for the buckling of an orthotropic plate with fixed ends and simply-supported and free edges. Results of the design studies conducted on a C-130 fuselage barrel subjected to combined axial compression and shear have shown that both the isogrid and orthogrid stiffening patterns result in savings over the existing metal design. For the isogrid stiffening, skin laminates with a lamination sequence of $[0/\pm\ 60]_S$ resulted in lighter designs compare to a $[0/90/\pm\ 45]_S$ sequence. The best design was obtained for a skin thickness of 0.072 *in* and stiffeners of 0.13 *in* thick and 1.3 *in* high. The results also indicated that both the isogrid and orthogrid stiffening concepts were weight competitive. However, the authors noted that the high damage tolerance characteristics of the isogrid concept would make it more attractive for aircraft fuselage applications.

In Ref. [11], equations predicting the buckling strength of cylindrical geodesic struc-

tures were presented. This represents the only available work on composite geodesic cylindrical shells. The analysis assumed that the buckling wave extended over a rather wide portion of the cylinder. Consequently, the cylinder behaved as if it were an orthotropic one and the discrete nature of the stiffeners was neglected. Based on numerical results, the author concluded that if the pitch of the geodesic members was relatively small compared to the cylinder radius, a cylindrical geodesic structure behaves as a uniform orthotropic-skin cylinder. On the other hand, if the buckling occurs over a localized portion of the cylinder, not including the buckling of a member between adjacent joints, finite element analysis must be used to predict the buckling load of the structure.

The geodesic concept was recently considered for impact-damage tolerant helicopter tail structures [12–13]. In this case, a cylindrical composite open framework in which the slender component bars follow the geodesics of the shell was considered. Only torsional loading was studied, and both linear and nonlinear finite element analyses were performed. It was found that using curved beam elements could produce a significant improvement in predicting the buckling torque over a previous analysis which used straight elements. However, large errors were still obtained compared to experimental buckling torques. Upon further detailed experimental testing of joints, the authors realized that the discrepancy was principally caused by the joint flexibility resulting from the scissoring of the crossing beams. It was found that this flexibility was an important factor in the overall behavior of the framework and to represent it, new models were set up. In these models, the crossing members were offset and the torsional stiffness represented with a 2-node beam element. Results obtained with these models were closer to the experimental results.

In Ref. [14] the analysis and the optimal design of a geodesically stiffened wing rib panel was performed. Through the use of Lagrange multipliers, the buckling load of rectangular orthotropic plates with a number of oblique stiffeners was calculated

without smearing the stiffeners. Design constraints considered in the analysis were global buckling of the panel assembly, local crippling of the stiffeners, and material strength. Design variables included thickness of the skin laminate, stiffener thickness, and stiffener height. The design study results showed that the grid-stiffened geometry resulted in lighter designs compared to the conventional longitudinal stiffened panel under the in-plane loading cases considered.

In a recent study, the effect of stiffness discontinuities and structural parameters on the response of continuous-filament grid-stiffened flat panels was presented [15]. The buckling load degradation due to manufacturing-introduced stiffener discontinuities associated with a filament cut-and-add approach at the stiffener intersection was investigated. For practical discontinuity sizes, the reduction in buckling load was found negligible. The benefit of utilizing non-solid stiffener cross sections, such as a foam-filled blade or hat with a 0° dominant cap, was evaluated. Such stiffener cross sections were found structurally very efficient for wing and fuselage applications.

In summary, the need for efficient and cost-effective structures has prompted the development and study of new stiffening patterns which present stiffeners oriented at an arbitrary angle with respect to the axis of the shell. In the case of isotropic cylindrical shells, two design studies that have considered axial compression and pressure have resulted in conflicting conclusions concerning the efficiency of geodesically stiffened shells. In the case of composite materials, no exhaustive design study has been conducted either. The only results available have been obtained from parametric studies on isogrid stiffened cylinders. In all cases, very dense grids of stiffeners were used. Although experimental results indicate that geodesically stiffened shells exhibit very good damage tolerance characteristics and that they can be cost-efficiently manufactured, no information is yet available concerning the performance of the geodesic stiffening concept compared to more conventional stiffener arrangements in the case of composite

structures.

2.3 Scope of Design Study

To evaluate the efficiency of the geodesic stiffening concept in the case of composite aircraft fuselages, a design study is proposed. Its overall objective is to seek practical, minimum-weight designs for geodesically stiffened composite cylindrical shells, and provide a database for a direct comparison of the optimal weights obtained with more traditional stiffening patterns. Although the cost for the construction of the different shell configurations may be different, no attempt will be made to include cost considerations into the comparison study. The functional requirements of aircraft fuselages force the inclusion of large openings such as access ports and windows. For this reason, larger skin portions between stiffeners, compared to those considered in the examples published in the literature, will be considered. Consequently, it is believed that the discrete nature of the stiffeners will have a stronger influence on the local and overall behaviors of the shell. This is among the reasons why its analysis will be obtained via the finite element method. All the design runs are performed with the optimization system TBOP (TestBed and OPtimization) which is a finite element based optimization system that has been developed in the course of this research initiative and that will be described in Chapter 3. Optimum designs are sought for unstiffened shells as well as the geodesically and conventionally stiffened shells subject to buckling and material failure constraints. In the case of the stiffened shells, different numbers of cells in the axial and circumferential directions are considered. Prospective geodesic and conventional configurations are shown in Figs. 2.2 and 2.3, respectively. In both cases, shaded portions indicate what is considered to be a single cell. Although this definition is somewhat arbitrary, it was chosen such that the number of stringers in the case of a conventionally stiffened shell, and stiffeners in the case of a geodesically stiffened shell are equal between geometries

with the same number of cells. The developed surface of each cell is also equal. In the case of the conventionally stiffened shell, the definition of a cell is as shown in Fig. 2.4. It includes a portion of the skin with two stringers (one in the middle and one half on each side) and is terminated by rings. Skin laminates with ±45°, 90°, and 0° plies will be considered, where the lamination angle in the skin is measured with respect to the axial direction. For the stiffeners, an orthotropic lamination sequence of $[0]_T$ is considered where the lamination angle in the stiffeners is measured with respect to their axis. Two levels of external loads, N_x, are applied in uniaxial compression: 1000 and 2700 pounds-force per inch (lb/in). In torsion, two levels are also considered: N_{xy} = 418.5 lb/in and 1000 lb/in.

In the case of the unstiffened shell, three design variables are used. They are the thickness of the 45°, 90°, and 0° plies, respectively. In the case of geodesically stiffened shells, five design variables are used. The first three are identical to those used in the case of the unstiffened shell, and the fourth and fifth design variables designate the thickness and height of the geodesic stiffeners. In the case of the conventionally stiffened shell, seven design variables are considered. The first three design variables are identical to those used in the case of the unstiffened shell. The fourth and fifth design variables designate respectively the thickness and height of the stringers, and the sixth and seventh, the thickness and height of the inner rings, respectively.

Properties of a typical graphite-epoxy material system (Hercules AS4/3502) are used in all analyses. Material properties for the stiffeners were assumed to be the same as those for the skin laminae. Since the maximum strain theory is used to predict material failure, the material strengths are expressed in terms of maximum allowable strain values. The elastic, strength, and physical properties used in the design study are shown in Table 2.1.

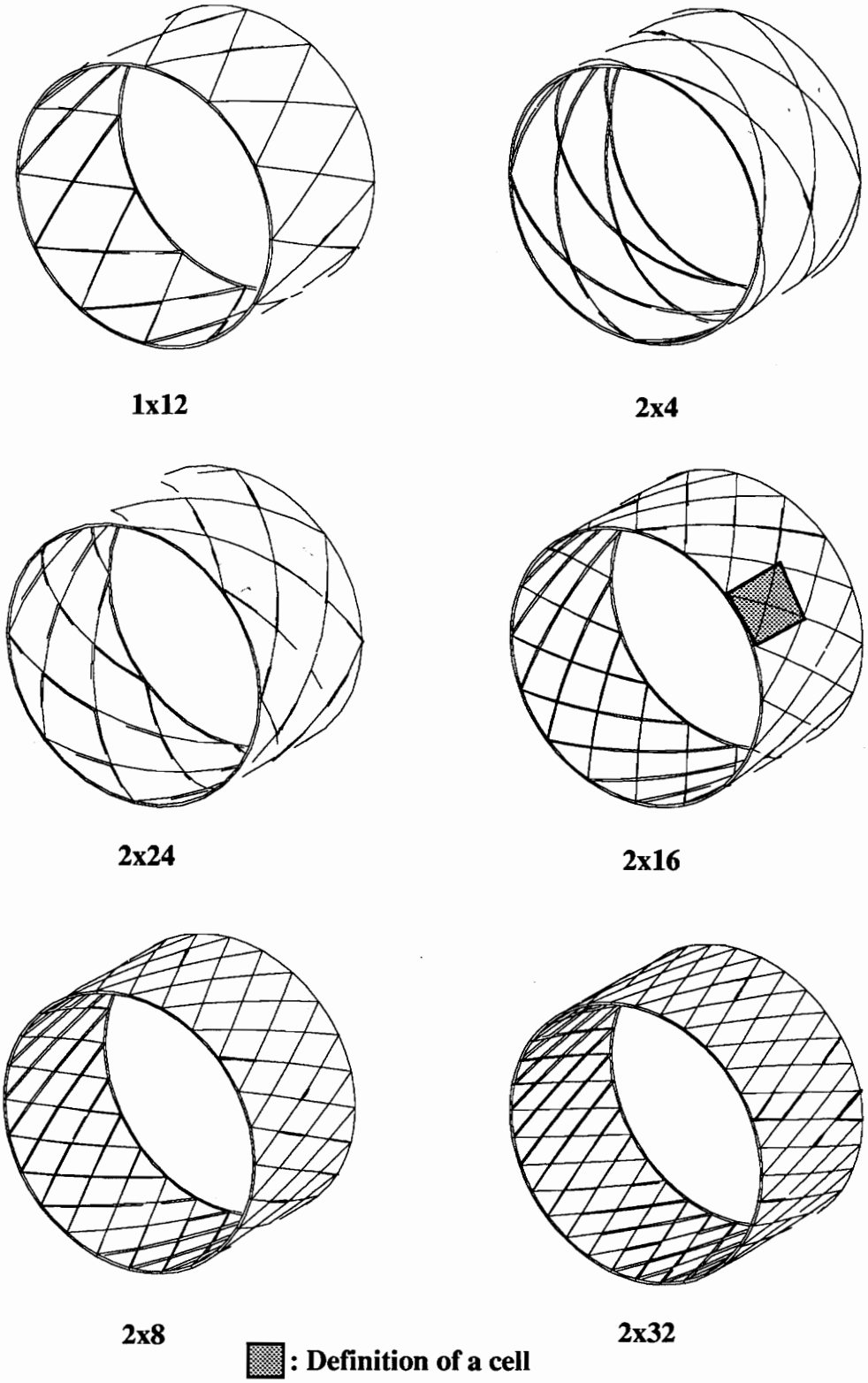

Fig. 2.2 – Design Study, Geodesically Stiffened Configurations.

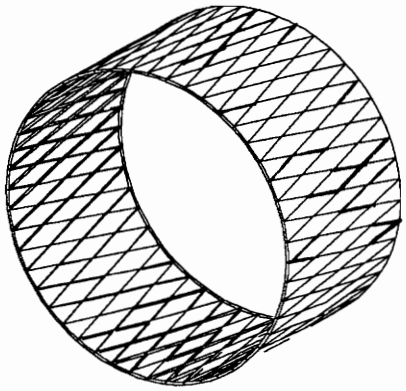

2x48

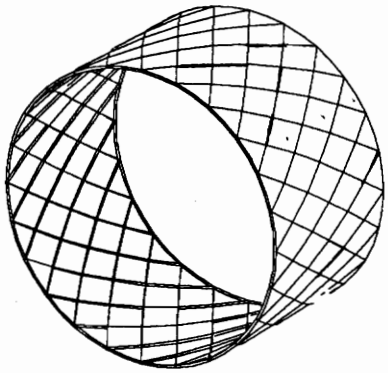

3x24

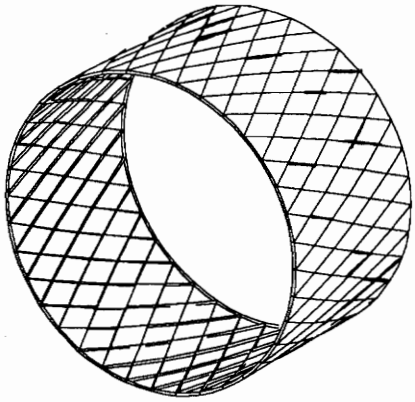

3x36

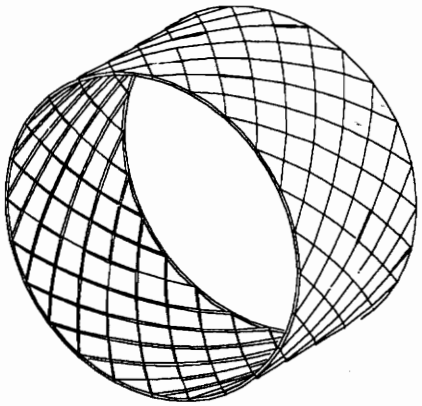

4x24

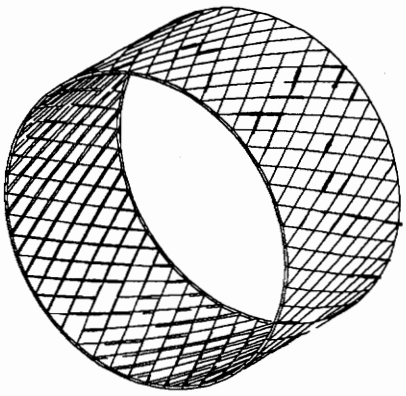

4x48

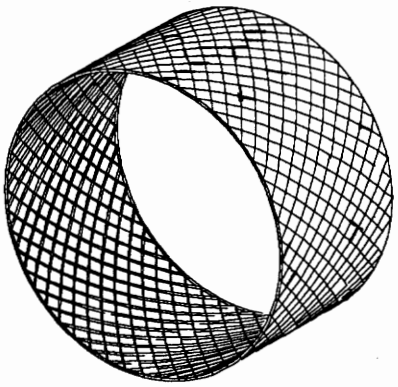

8x48

Fig. 2.2 – Design Study, Geodesically Stiffened Configurations (Continued).

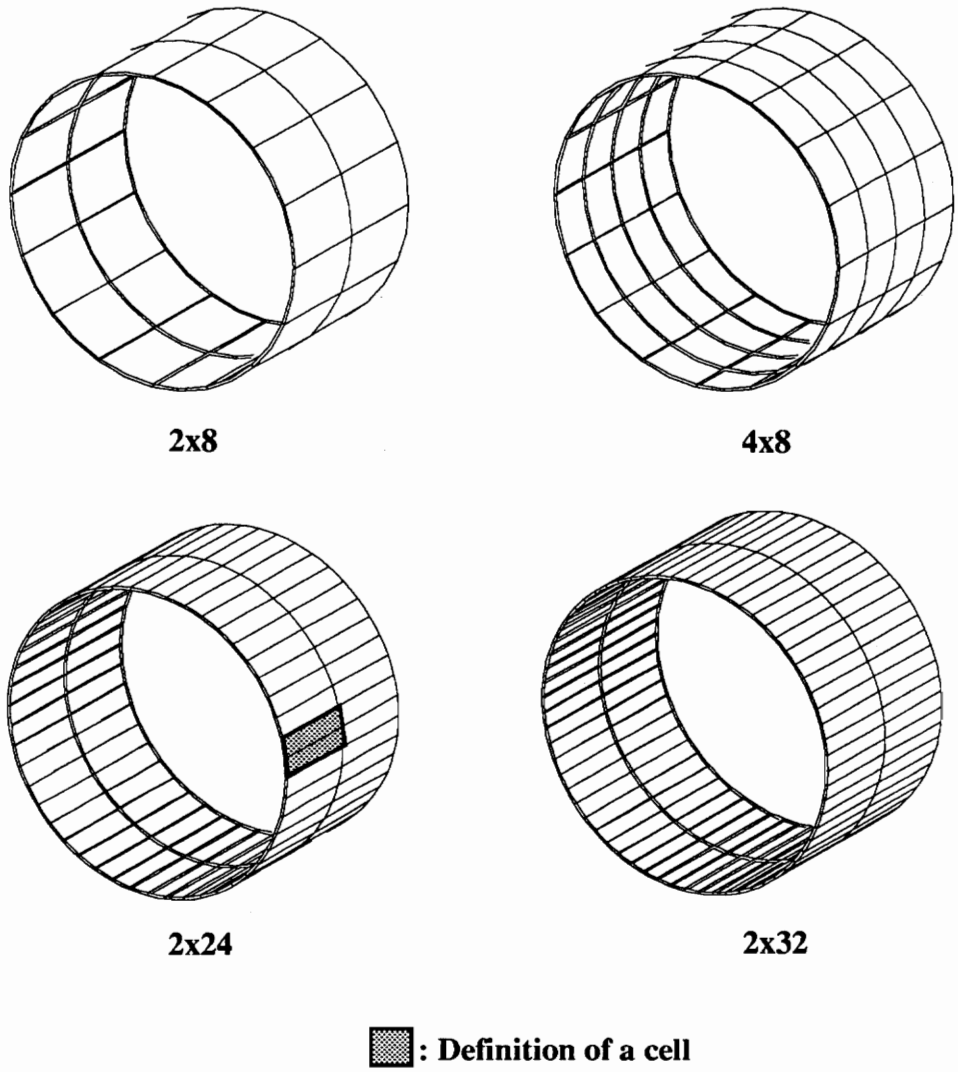

Fig. 2.3 – Design Study, Conventionally Stiffened Configurations.

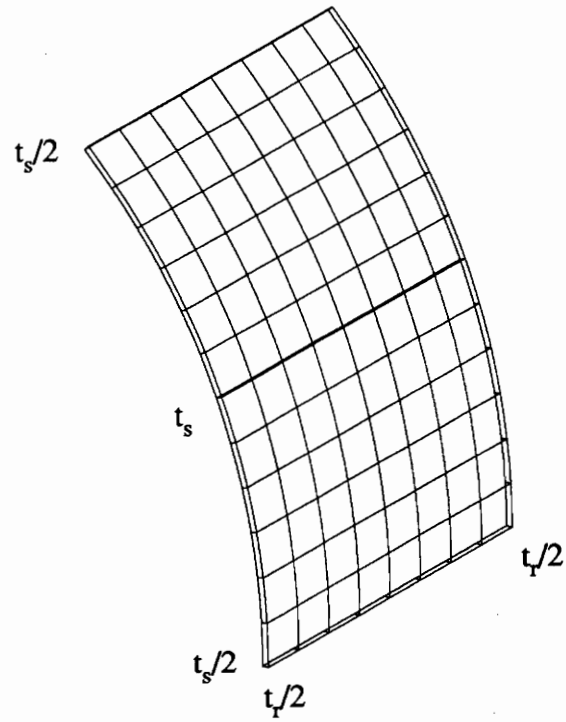

Fig. 2.4 – Definition of a Cell for the Conventionally Stiffened Shell.

Table 2.1 – Graphite-Epoxy Material Properties.

Elastic Properties :

E_1 Msi	E_2 Msi	G_{12} Msi	G_{23} Msi	ν_{12}
18.5	1.64	0.87	0.54	0.3

E_1 GPa	E_2 GPa	G_{12} GPa	G_{23} GPa	ν_{12}
128	11.3	6.0	3.7	0.3

Strength Properties :

$\epsilon^t_{1,allowable}$	$\epsilon^c_{1,allowable}$	$\epsilon^t_{2,allowable}$	$\epsilon^c_{2,allowable}$	$\gamma_{12,allowable}$
0.009	0.008	0.0055	0.029	0.025

Physical Properties :

$\rho = 0.057$ lbm/in^3 (1600 kg/m^3)

Chapter 3
The Optimization System

Comparing the efficiency of the geodesic stiffening concept to unstiffened and conventionally stiffened shells requires the study of different and complex configurations. To guarantee uniformity in the results, a versatile analysis and design tool that can deal with each of these different configurations has to be used. This requirement prompted the development of the new optimization system presented in this chapter.

Several alternatives can be considered for the development of an optimization system. The use of special purpose programs that combine both the computation of the structural response as well as the implementation of the optimization algorithm is one of the alternatives. However, such programs have limited capabilities and are consequently not suitable for the type of research considered herein. More often, a general purpose analysis package, such as a finite element code, is used for the computation of the structural response and an optimization package solves the design problem. This is the approach followed in the present study. The optimization tool is based on the finite element code CSM Testbed [16,17] and the optimization program ADS [18]. Before proceeding to the description of this new optimization system, some terminology that will be used in the present study is defined in Section 3.1. In Section 3.2, other optimization systems that have been recently developed are briefly described. Then, in Section 3.3.1, some generalities and the philosophy that has guided the development of the optimization system are presented. This is followed, in Sections 3.3.2 and 3.3.3, by a description of the new computational modules and procedures that have been developed to orchestrate the sequence of calculations required to achieve an optimum. The description of the optimization system ends with a discussion of the strategy that implements the imposition

of buckling constraints. Finally, in Section 3.4, the results obtained for three example problems are discussed.

3.1 Terminology

The definition of the principal terms used in this chapter is given in this section. The notion of optimal design requires the definition of a merit function, called the objective function, that can be improved. An improvement in the objective function can be achieved by varying certain characteristics of the model, called design variables. Also, the design must usually satisfy a set of equalities and/or inequalities which impose lower or upper bounds on quantities such as displacements, strains, eigenvalues, etc .... These relations are called constraints and they may be used, for example, to specify bounds on the value of the buckling load or the displacement of a point. The optimization problem is:

$$\begin{aligned} &\textbf{minimize } f(\mathbf{x}) \\ &\textbf{such that } g_j(\mathbf{x}) \leq 0, \qquad j = 1, \ldots, n_g \\ &\qquad\qquad h_k(\mathbf{x}) = 0, \qquad k = 1, \ldots, n_h, \end{aligned} \tag{3.1}$$

where f is the objective function, g_j are the inequality constraints, h_k the equality constraints, and $\mathbf{x}$ the vector of design variables.

In the present study, an optimization system is defined as a computer program that can realize the minimum-weight design of a structure based on a structural response obtained from a finite element code. Such a system can be divided into three parts. A general-purpose finite element code represents one of these parts. It is used to compute the structural response corresponding to a specific design. A second part consists of the sensitivity analysis module. It is responsible for the computation of the structural response derivatives with respect to the design variables. This information is required by the optimizer which constitutes the third part.

It is clear that although this definition of an optimization system fits the approach used in the present work, the second of the three basic components, namely the sensitivity module, does not necessarily need to be present. If it is absent, the derivative information can be computed using a finite difference formulation. This approach requires the successive analysis of several designs, each of which is obtained by perturbing the value of a single design variable.

The finite element code used in the present study is called the CSM Testbed program [16,17]. It consists of a set of semi-independent computational modules, known as processors, which communicate with each other only by exchanging data objects residing in a data library. To utilize the processors in a particular analysis task, procedures must be written in a high-level command language called CLAMP [16] (Command Language for Applied Mechanics Processors). The commands of a CLAMP procedure can be interpreted and converted into object records by a "filter" utility called CLIP [16] (Command Language Interpreter Program). The framework is depicted in Fig. 3.1.

3.2 Finite Element Based Optimization Systems

The versatility achieved by combining a finite element program and an optimization code has attracted the interest of many researchers and three examples where this strategy has been chosen can be found in recent literature. In Ref. [19], Walsh combined the EAL [20] commercial package with the general-purpose optimization program CONMIN [21]. CONMIN employs a usable-feasible directions search algorithm to minimize an objective function that is subjected to a set of inequality constraints. Piecewise-linear approximations of the objective function and the constraints along with move limits were used in order to reduce the number of exact analyses required to achieve the optimum. Except for the move limits, the only constraints supported by this optimization system were stress constraints. The derivative computations were performed using the semi-

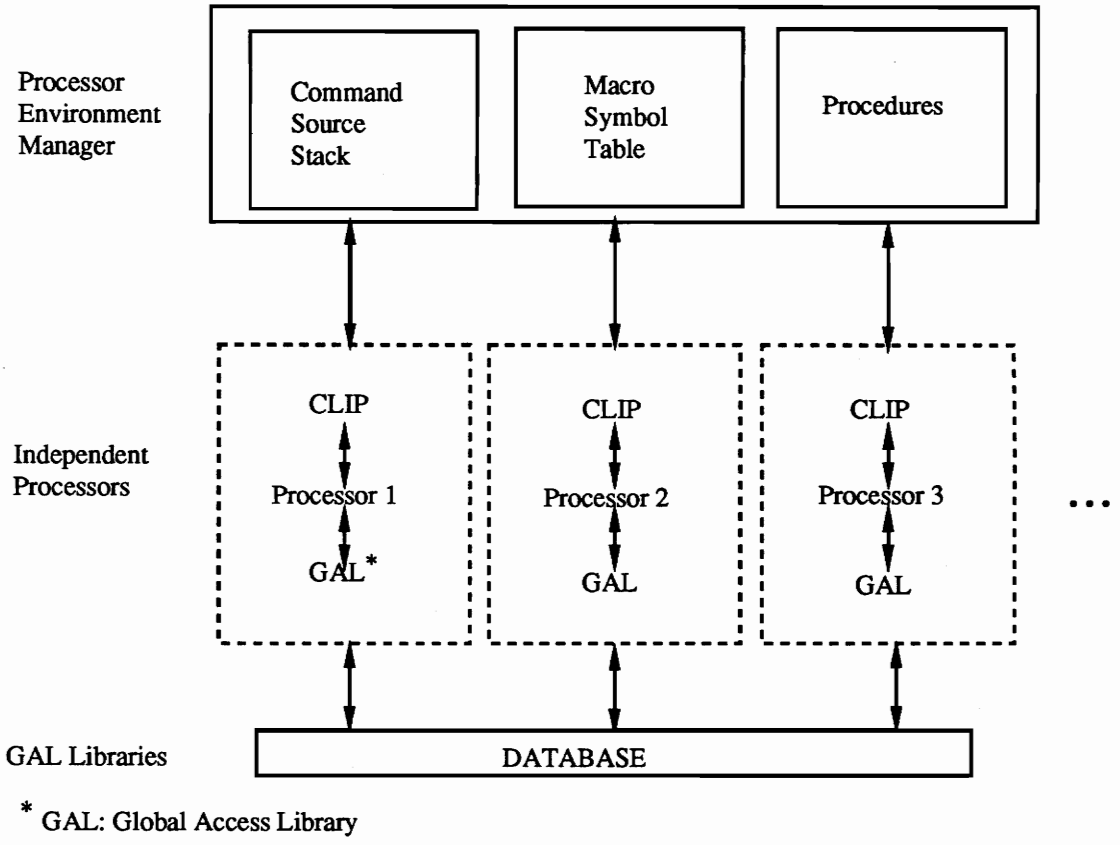

* GAL: Global Access Library

Fig. 3.1 – Implementation of the CSM Testbed Software System.

analytical approach described in Ref. [22]. The optimization system was applied to the minimum-mass design of a large transport-type wing designed to satisfy stress constraints while subjected to two static loading conditions. Results obtained using the system were compared with results produced by a fully stressed design procedure.

Probably one of the most popular and widely used finite element analysis code is the MSC/NASTRAN computer program. In 1983, a design sensitivity analysis module was developed for this program and this new feature resulted in the development of several optimization systems based on MSC/NASTRAN. The design sensitivity module was recently enhanced to include design variables and responses for composite materials. This new facility was used in Ref. [23] to develop a NASTRAN-based optimization system that can be used to design composite structures. The optimizer is called CONLIN [24] and its interface with MSC/NASTRAN was also described in the paper. CONLIN is a general-purpose optimizer that uses a convex linearization scheme to solve the optimization problem.

For the design sensitivity analysis of composites in MSC/NASTRAN, the design constraints could be lamina stresses or failure indices, displacement, frequency, buckling loads, or forces. Sensitivity of the design to changes in lamina thicknesses, orientation angles, or material properties could be obtained. However, a single type of variables, lamina thicknesses, could be defined as design variables. Semi-analytical expressions were used for the calculation of the constraint derivatives with respect to the design variables.

The optimization system described in Ref. [23] was tested on two example problems. The first problem dealt with the minimum-mass design of a rectangular laminated composite plate with a circular hole subjected to a material failure constraint. The second demonstration problem considered the minimum-mass design of a delta wing subjected to a displacement constraint.

Recently, the finite element program ABAQUS [25] and the optimization code ADS [18] were combined to form the optimization system described in Ref. [26]. In this case, no sensitivity module was developed. However, the finite difference calculations corresponding to the approximation of the constraint derivatives with respect to the design variables were performed on separate processors. The optimization system was used to obtain a minimum-mass design for an aircraft canopy loaded by an internal pressure. The optimization was performed using 50 thickness design variables and only stress constraints based on the von Mises criterion were imposed at each element.

3.3 A New Optimization System

3.3.1 Generalities

The new optimization system, called TBOP, is based on the CSM Testbed [16,17] and the general purpose optimization code ADS [18]. A user's manual is available for the program (see Ref. [27]), and consequently, none of the details related to the use of the optimization system will be presented here. The CSM Testbed is a framework for computational structural mechanics research which integrates research in structural mechanics, numerical analysis, and computer science. Several considerations have motivated the choice of the CSM Testbed. Among these considerations, the unrestricted access to all parts of the source code, the modularity, as well as the availability of a variety of state-of-the-art solution algorithms are major motivations. Another interesting aspect of the CSM Testbed is that it offers algorithms that exploit the hardware capabilities available with the new generation of computers. The availability of state-of-the-art solution algorithms and their efficient implementation are very important features in the context of optimization where the analysis must be repeatedly performed. The version of the CSM Testbed used in the present study performs all the calculations using 16 digits.

The choice of the ADS optimization module has been motivated by the wide set

of strategies that it offers to solve the optimization problem. This feature allows the tailoring of the optimization strategy to the problem at hand. Moreover, the architecture of ADS is such that it can be turned into a CSM Testbed processor by simply defining separate subroutines without requiring modifications to its original code. This means that it can easily be replaced once a new version of the program becomes available. This characteristic also preserves the modularity of the optimization system that can easily be separated into its three basic modules; namely, the finite element code, the sensitivity analysis module, and the optimizer.

The organization of the optimization system follows the philosophy used in the development of the CSM Testbed program (see Fig. 3.1). The CSM Testbed differs from conventional finite element codes in that there is no single, monolithic program (processor) controlling all aspects of the analysis. Instead, there is a growing set of independently executable FORTRAN processors, each of which is responsible for only a small portion of the work, and on top of which are a growing selection of high-level CLAMP procedures. To enforce modularity, processors do not communicate explicitly with each other, but instead communicate only by exchanging data objects in the global database. The global database is made up of sets of data libraries which contain collections of named datasets.

To keep up with this philosophy, a set of CLAMP procedures have been developed to control the optimization run. Each of these procedures implements a small portion of the work that must be performed to compute an optimum. Also, ADS has been embedded into a processor. This means that it can now be called just as any other CSM Testbed processor. As a result, both the optimization and the analysis programs are sitting at the same level, and CLAMP procedures are in charge of calling each processor in the appropriate order. The flow of calculations required for the computation of an optimum is shown in Fig. 3.2. In theory, however, ADS is the "master" that sets the design

variables to their new values and the analysis modules of the CSM Testbed constitute the "slave" responsible for the computation of the information required by the optimizer to proceed in the design space. This information may consist of the function values or of their derivatives with respect to the design variables as requested by the optimizer through a variable called `info`.

In its current implementation, the optimization system supports three different types of design variables. Two are related to the laminate construction. They are the thickness of a ply and its orientation. The third type of design variable can designate the size of finite elements and, consequently, allows a limited amount of shape optimization to be performed. In this study, it is used to modify the height of stiffening members. Linking of the thickness or orientation design variables is possible.

The optimization system defines the weight of the structural component as the objective function that must be minimized subject to a set of constraints. Although this still allows for the solution of a wide class of problems, this type of objective function will be difficult to use in conjunction with ply angle design variables because the gradient of the objective function with respect to such design variables is zero. Consequently, the only design variables considered in the present study are ply thicknesses and size of finite elements.

Three types of constraints, buckling g_b, displacement g_d and material failure constraints g_f, can be imposed on the design. Buckling constraints are predicted using a linearized buckling analysis which results in the solution of an eigenvalue problem. Critical load vectors $\mathbf{P}_j$, which correspond to buckling in different modes, are obtained by:

$$\mathbf{P}_j = \lambda_j \mathbf{P}_{ref}, \tag{3.2}$$

where λ_j is the jth eigenvalue and $\mathbf{P}_{ref}$ is a reference load vector. The kth buckling

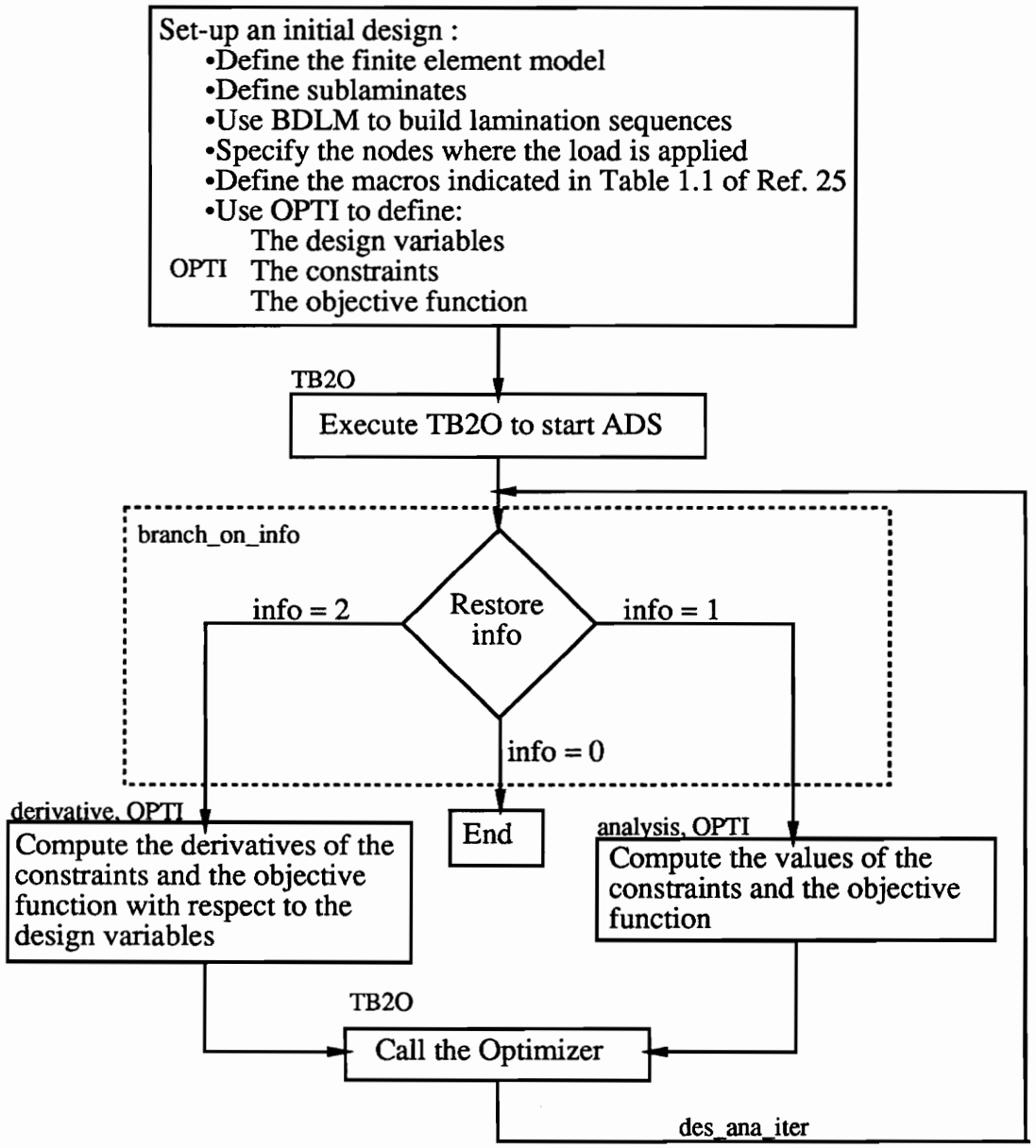

Fig. 3.2 – Flow of Calculations.

constraint g_{bk} is:

$$g_{bk} = \overline{v}_k - \lambda_j \leq 0, \qquad k = 1, \ldots, n_b, \tag{3.3}$$

where $\overline{v}_k$ is the limiting value of λ_j, and n_b is the number of buckling constraints. Since λ_j and $\overline{v}_k$ are close to 1.0, the buckling constraints do not need to be normalized. The procedure used in the present study to impose buckling constraints will be discussed in Section 3.3.4. The displacement constraints g_d require that the jth component of the nodal displacement vector be less than a given maximum allowable value $\overline{u}_k$. The kth displacement constraint is:

$$g_{dk} = \frac{|u_{dj}|}{\overline{u}_k} - 1.0 \leq 0.0. \qquad k = 1, \ldots, n_d. \tag{3.4}$$

Finally, the material failure constraints, g_f, are evaluated using the maximum strain failure theory. The strains in each ply are first calculated from the mid-plane strains and curvatures computed at a specific integration point. They are then transformed to the principal material directions and compared to their respective allowable values. The ratio closest to 1.0 is retained and used to evaluate the constraint,

$$g_{fk} = \frac{|\epsilon_j|}{\overline{\epsilon}_k} - 1.0 \leq 0.0, \qquad k = 1, \ldots, n_p, \tag{3.5}$$

where ϵ_j is a component of the engineering strains and $\overline{\epsilon}_k$ is its maximum allowable value.

Since a gradient-based optimization algorithm is used, the derivatives of the constraints with respect to the ith design variable x_i are required. These are found by differentiating Eqs. (3.3)-(3.5) and their calculation will be discussed in Section 3.3.3.

3.3.2 The Processors

The CSM Testbed consists of a library of independently executable FORTRAN computational modules or processors. To build the optimization system, three new

processors have been added to this library. The first of these processors, BDLM (BuilD LaMinate), builds the different lamination sequences to be used in the various sections of a model. This processor reads user-defined sublaminate stacking sequences and stacking orders and creates new datasets that contain the definition of complete stacking sequences for groups of elements. This feature allows a design variable to designate the thickness or orientation of a ply contained in several lamination sequences. This is important from a manufacturing point of view since tailoring of a structure is normally achieved by adding, at selected locations, plies with appropriate thicknesses and orientations on top of an underlying base laminate.

The implementation of this feature has been realized by first breaking up the definition of the lamination sequences into two successive steps. In the first step, sublaminate stacking sequences are defined in exactly the same way lamination sequences are defined in the CSM Testbed. Then, the order in which each sublaminate must be stacked to produce the complete lamination sequence is given. For example, the definition of the four stacking sequences L1 through L4 of the plate shown in Fig. 3.3 is obtained by defining three sublaminate sequences, S1-S3 and four stacking orders, one for each section. The base sublaminate S1 covers all four sections of the plate while vertical and horizontal sections with different properties are obtained by adding S2 and S3, respectively. These vertical and horizontal sections may represent the flange area of stiffeners and fail safe straps, respectively, that are added to the skin laminate to improve the structural performance.

Secondly, the ply orientation and ply thickness design variables refer to plies contained in sublaminate stacking sequences. This implies that when the value of one of these design variables is changed, only one sublaminate sequence must be updated but all the lamination sequences that contain this sublaminate must be rebuilt by BDLM. Consider an example where the optimal thickness of one of the 90° plies adjacent to

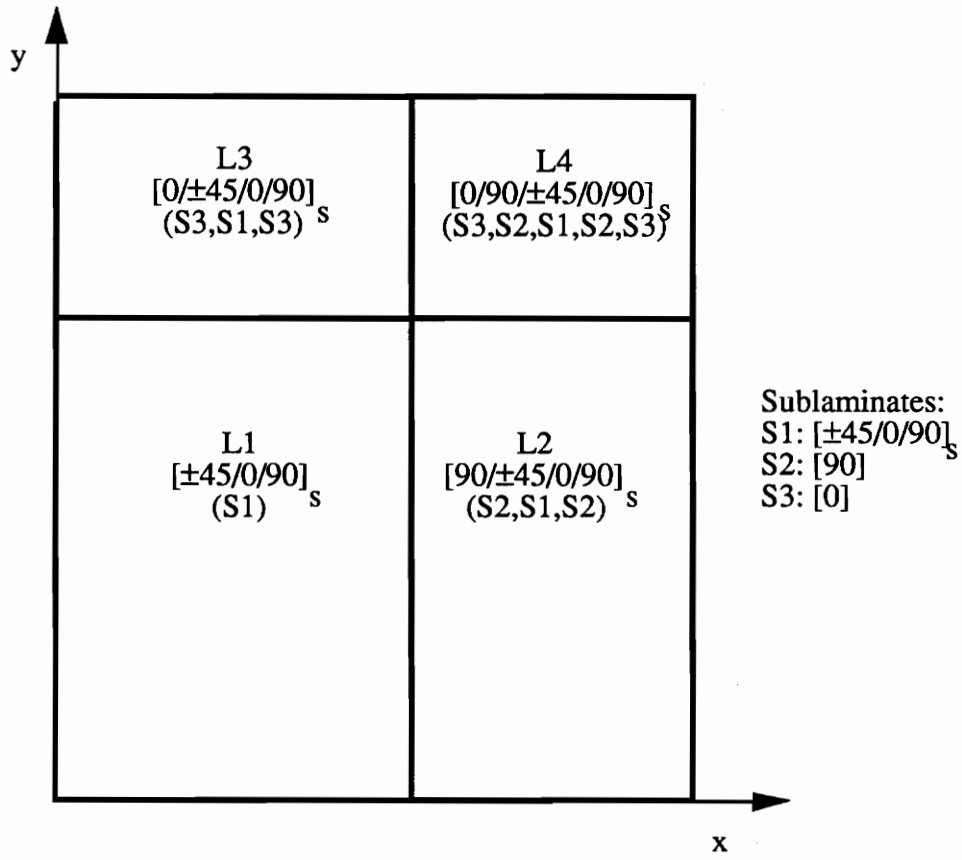

Fig. 3.3 – Lamination Sequences for a Flat Plate.

the mid-plane of the plate shown in Fig. 3.3 is sought. In this case, the sublaminate sequence S1 must be updated but the four lamination sequences must be rebuilt since S1 enters the definition of each of them.

The second processor added to the library of CSM Testbed processors is called OPTI. This processor is primarily used to set up the optimization problem and extract, from the CSM Testbed database, the information necessary for the evaluation of the constraints and their gradients. The functionalities of the processor can consequently be divided into three groups. The first group contains the different facilities required for the definition of the design variables, the constraints and the objective function. These facilities are used once, at the beginning of each design run, to set up the optimization problem. The second group contains programs that access the database and evaluate the constraints and their gradients. Finally, a third group of functionalities realize miscellaneous operations required at different stages of the optimization run. For example, one subroutine calculates the load applied to the model and the corresponding scale factor that must be applied to the displacements when the loading is introduced using displacement boundary conditions.

The third processor is called TB2O. This processor contains the optimization program ADS, and it also serves as an interface between the CSM Testbed and ADS. Most of the interfacing work consists of reading information from the CSM Testbed datasets and passing this information to ADS using different FORTRAN variables and arrays. The information that needs to be sent to ADS includes the values of the design variables, the constraints, the objective function, as well as miscellaneous optimization-related data. Upon return from the optimizer, the design has been modified, and TB2O updates the different datasets that need to be changed. Those datasets consist of the sublaminate stacking sequences in the case of ply thickness or ply orientation design variables. In the case of height design variables, the dataset that contains the node coordinates must

be updated.

3.3.3 The Procedures

As previously mentioned in Section 3.3.1, a set of CLAMP procedures implements the sequence of operations required for the computation of an optimal design. To better understand the role of each procedure, flowcharts that describe the performed operations are included in Appendix A. The different procedures are briefly described in this section.

The procedure controlling the optimization run is called `des_ana_iter`. It implements the loop shown in Fig. 3.2. At each cycle, either an exact analysis or the computation of the derivatives of the functions that define the optimization problem are performed. The analysis and derivative calculations are controlled by the procedure `branch_on_info`, and consequenly, `des_ana_iter` first calls this procedure, and then the optimizer.

The role of `branch_on_info` is to organize the evaluation of the structural response corresponding to the current design or a perturbation of the current design. In either case, `branch_on_info` must call either the procedure `analysis` or `derivative` and the processor OPTI. If the optimizer has requested the calculation of the values of the functions, the two libraries containing the database are first examined to eliminate obsolete information generated at the previous design point. Then, a procedure named `analysis` is called. The role of this procedure is described below. Finally, the processor OPTI is executed to evaluate the constraints and the objective function. On the other hand, if the values of the derivatives have been requested, a procedure named `derivative`, which is also described below, will first be called. This call is immediately followed by an execution of the processor OPTI. In this case, OPTI is responsible for the constraint and objective function derivatives with respect to the design variables.

The role of the procedure `analysis` is to compute the information required by

OPTI to evaluate the constraints. Depending on the nature of the constraints imposed on the design, this information may consist of the displacement vector, the eigenvalues corresponding to the buckling problem, and/or the strains. In order to apply combined loading conditions while controlling the individual magnitudes, `analysis` implements a scaling feature that permits the loading to be introduced using applied displacements.

With the finite element method, the loading can be applied by specifying either nodal displacements or nodal forces at the boundaries. If nodal forces are applied, no scaling will be necessary since the magnitude of the applied load corresponds to the magnitude of the design load. However, the resulting displacements at the loaded edges are not necessarily uniform and, therefore, deviate from the boundary conditions that are observed during the actual loading of the structure. One way of solving this problem is to place stiff elements adjacent to the loaded boundary. Because of the increased computational cost associated with a larger model and the ill-conditioned matrices that result from a model with large differences in the stiffness of its elements, load introduction through applied displacements is usually preferred. In this case, the boundary conditions can be applied directly to the model of the structure and the corresponding nodal loads are computed from the finite element solution.

Although using nonzero boundary conditions eases the analysis of the structure, the static displacements corresponding to a specific design must be scaled by `analysis` since the load resulting from applying such boundary conditions may not correspond to the design load. To handle combined loading conditions, `analysis` can compute up to three scaling factors, each factor corresponding to a different component of the combined loading condition. For example, consider the case of a structure that must be designed to resist a combined compression and shear loading. In such a situation, the user must specify two series of nonzero displacement boundary conditions, one of which corresponds to a case of pure compressive loading and the other to a case of pure shear.

During the analysis of the structure, the procedure `analysis` will consider each case independently by computing a static displacement solution and a scaling factor for each of them. It will then apply each scaling factor to its corresponding static displacement solution and superpose them to obtain the static displacement solution corresponding to the combined loading condition. This resulting set of displacements will be used to compute the strains and the eigenvalues of the buckling problem.

The procedure `derivative` performs the computations of the perturbed structural response quantities such as displacements, strains, etc ..., which are required by the processor OPTI to evaluate the constraint derivatives with respect to the design variables. With ADS, the user has the option of either letting ADS determine the derivatives by finite differences or supplying the derivative information to ADS. Because of the organization of the optimization system, the latter method must now be chosen. Both an overall finite difference scheme (OFD) and a semi-analytical (SA) method have been implemented in the procedure `derivative` for the approximation of the derivatives of the constraints with respect to the design variables. Note that in the present study, the objective function corresponds to the weight of the structure. Therefore, the computation of its derivatives is based solely on geometric characteristics.

The semi-analytical method for the calculation of the constraint derivatives combines an analytical expression for the displacement derivatives and a finite difference approximation for the derivatives of the system matrices. This strategy is outlined below for the cases of applied nodal forces and nonzero displacement boundary conditions.

In the case of applied nodal forces, the derivative of the displacement vector with respect to a design variable $d\mathbf{u}_d/dx_i$ is obtained by solving the set of equations resulting from taking the first derivative of the equilibrium equations with respect to x_i:

$$\mathbf{K}\frac{d\mathbf{u}_d}{dx_i} = \frac{d\mathbf{f}}{dx_i} - \frac{d\mathbf{K}}{dx_i}\mathbf{u}_d, \tag{3.6}$$

where $\mathbf{K}$ is the stiffness matrix, $\mathbf{u}_d$ the displacement vector, and $\mathbf{f}$ the load vector. The terms $d\mathbf{K}/dx_i$ and $d\mathbf{f}/dx_i$ are approximated using finite difference formulas.

If nonzero displacement boundary conditions are applied [28], the equilibrium equations can be viewed as:

$$\begin{bmatrix} \mathbf{K}_{1,1} & \mathbf{K}_{1,2} \\ \mathbf{K}_{1,2}^T & \mathbf{K}_{2,2} \end{bmatrix} \begin{Bmatrix} \mathbf{u}_u \\ \mathbf{u}_c \end{Bmatrix} = \begin{Bmatrix} \mathbf{0} \\ \mathbf{R} \end{Bmatrix}, \tag{3.7}$$

where block $\mathbf{K}_{1,1}$ represents the non-singular matrix that is solved by a linear equation solver while blocks $\mathbf{K}_{1,2}$ and $\mathbf{K}_{2,2}$ contain coefficients that are eliminated due to constraint conditions. The vectors of unknown displacements and boundary conditions are represented by $\mathbf{u}_u$ and $\mathbf{u}_c$, respectively. Note that $\mathbf{u}_c$ may have zero and nonzero components depending respectively on whether the corresponding nodal displacement is fully restrained, or nonzero displacement boundary conditions are specified. Similarly, the right-hand-side vector is divided into two parts: a null vector $\mathbf{0}$, and the static reaction vector, $\mathbf{R}$.

The load applied to the model, $F_a(\mathbf{x})$, corresponding to the boundary conditions $\mathbf{u}_c$ is:

$$F_a(\mathbf{x}) = \left| \sum_{j \in \mathbf{A}} R_j \right|, \tag{3.8}$$

where $\mathbf{A}$ is a user-defined vector that gives the position in the static reaction vector of the components that must be added to obtain the total applied load.

If the design load is F_d, then the displacement vector corresponding to the design load, $\mathbf{u}_d$, is given by:

$$\mathbf{u}_d = \begin{Bmatrix} \mathbf{u}_{du} \\ \mathbf{u}_{dc} \end{Bmatrix} = s(\mathbf{x}) \begin{Bmatrix} \mathbf{u}_u \\ \mathbf{u}_c \end{Bmatrix}, \tag{3.9}$$

where $\mathbf{s}(\mathbf{x})$ is a scale factor given by:

$$s(\mathbf{x}) = F_d / F_a(\mathbf{x}). \tag{3.10}$$

In this case, the derivative of $\mathbf{u}_{dc}$ with respect to a design variable x_i is given by:

$$\frac{d\mathbf{u}_{dc}}{dx_i} = \frac{ds}{dx_i}\mathbf{u}_c \tag{3.11}$$

and, similarly, $d\mathbf{u}_{du}/dx_i$ is obtained from:

$$\frac{d\mathbf{u}_{du}}{dx_i} = s\frac{d\mathbf{u}_u}{dx_i} + \frac{ds}{dx_i}\mathbf{u}_u. \tag{3.12}$$

To obtain ds/dx_i, successively differentiate Eqs. (3.10) and (3.8):

$$\frac{ds}{dx_i} = \frac{-F_d}{F_a^2}\left|\sum_{j\in\mathbf{A}}\frac{dR_j}{dx_i}\right|, \tag{3.13}$$

where, $d\mathbf{R}/dx_i$ is obtained by differentiating the equilibrium equations corresponding to $\mathbf{u}_c$, Eq. (3.7). That is,

$$\frac{d\mathbf{R}}{dx_i} = \frac{d\mathbf{K}_{1,2}^T}{dx_i}\mathbf{u}_u + \mathbf{K}_{1,2}^T\frac{d\mathbf{u}_u}{dx_i} + \frac{d\mathbf{K}_{2,2}}{dx_i}\mathbf{u}_c. \tag{3.14}$$

Finally, the only missing term in the expression for $d\mathbf{u}_{du}/dx_i$, is $d\mathbf{u}_u/dx_i$ and it can be obtained by taking the first derivative of the equilibrium equations corresponding to $\mathbf{u}_u$, Eq. (3.7). That is,

$$\mathbf{K}_{1,1}\frac{d\mathbf{u}_u}{dx_i} = -\frac{d\mathbf{K}_{1,2}}{dx_i}\mathbf{u}_c - \frac{d\mathbf{K}_{1,1}}{dx_i}\mathbf{u}_u. \tag{3.15}$$

Note that one of the reasons for the SA method to result in computational savings, compared to the OFD approach, is that it does not require the factorization of system matrices for computation of the derivatives. The solutions that need to be computed use system matrices that have already been factored during the previous exact analysis. Consequently, only forward elimination and backward substitution operations are required and are one order of magnitude less expensive than the matrix factorization.

Once these computations have been performed and the derivative of the displacement vector with respect to a design variable has been obtained, the calculation of the derivatives of the constraints (Eqs. (3.3)–(3.5)) can be performed. In the case of a buckling constraint, we obtain [29]:

$$\frac{dg_b}{dx_i} = -\frac{d\lambda_j}{dx_i} = -\frac{\mathbf{u}_j^T(\frac{d\mathbf{K}}{dx_i} + \lambda_j\frac{d\mathbf{K}_G}{dx_i})\mathbf{u}_j}{\mathbf{u}_j^T\mathbf{K}_G\mathbf{u}_j}, \tag{3.16}$$

where $\mathbf{K}_G$ is the geometric stiffness matrix, and $\mathbf{u}_j$ is the jth eigenvector. As for other system matrices, the derivative of $\mathbf{K}_G$ is approximated using a forward finite-difference formula. The perturbed geometric stiffness matrix entering the finite-difference formula is obtained using the stresses corresponding to a first-order Taylor series approximation $\mathbf{u}_d^i$ of the perturbed displacement vector:

$$\mathbf{u}_d^i = \mathbf{u}_d + \frac{d\mathbf{u}_d}{dx_i}\Delta x_i, \tag{3.17}$$

where Δx_i represents a perturbation in the value of x_i.

In the case of a displacement constraint, the derivative is directly obtained from the solution of Eq. (3.6) or (3.12). Finally, in the case of material failure constraints, Eq. (3.17) is first used to approximate the perturbed displacement vector. Then, the strains corresponding to $\mathbf{u}_d^i$ are computed. Finally, a finite difference formula is used to approximate the derivative of the constraint with respect to x_i.

3.3.4 Implementation of Buckling Constraints

Structures made up of thin-walled components must be designed for buckling resistance. To put the problem of imposing buckling constraints in perspective, it is worthwhile to present a simple example and briefly review the different alternatives that can be considered for the imposition of such constraints.

The example used to illustrate the imposition of buckling constraints is shown in Fig. 3.4. It is a simply-supported open-web truss structure subjected to a uniform compressive loading applied using nonzero displacement boundary conditions at its top edge (y = 28 in). Two design variables are considered; one represents the thickness t of the members, and the other their height h (z–direction in Fig. 3.4), with initial values of 0.55 in and 0.60 in, respectively. The objective function represents the total weight of the truss. The lowest eight eigenvalues obtained for this design are presented in Table 3.1. As indicated in this table, based on the general shape of the eigenmodes, the eigenvalues

can be classified into two different sets. The lowest three eigenvalues are associated with in-plane buckling modes that are slightly different from one another. Similarly, the eigenvalues 4 through 8 are associated with slightly different out-of-plane buckling modes. The first, second, fourth, and fifth buckling modes are shown in Fig. 3.5. Because of the general shape of the buckling modes, it can intuitively be deduced that changing t has a stronger influence on the lowest three eigenvalues than changing h, and vice versa. For example, the variation of the critical loads associated with the first in-plane and the first out-of-plane modes with respect to the height of the members is shown in Fig. 3.6.

Based on the dependencies of the eigenvalues on the design variables, and assuming that the optimization process is started from the initial design t = 0.55 in and h = 0.6 in, it can intuitively be deduced that, to reach the optimum, the optimizer will tend to increase t and decrease h in such a way that the lowest eigenvalue remains at 1.0 and that the weight will be reduced. Such a move, however, will result in a smaller difference between the values of the fourth and third eigenvalues. As the design progresses, the magnitude of the fourth eigenvalue will continuously decrease, until it switches place with the lower ones. Eventually the two eigenvalues corresponding to the first out-of-plane and in-plane modes will approach the same value.

To guarantee that all the buckling modes are taken into account during the design process, closely-spaced eigenvalues that can potentially switch places may require the imposition of as many buckling constraints as there are computed eigenvalues. However, this practice is inconvenient since to avoid coalescent eigenvalues which are undesirable because they cannot be combined in a linear fashion [29], increasing values must be chosen for $\overline{v}_k, k = 1, ..., n_b$ in Eq. (3.3). As a result of imposing such a number of buckling constraints, the optimization problem may become over-constrained and non-optimal designs can be obtained. On the other hand, imposing a single buckling constraint based on the lowest eigenvalue may result in convergence problems as the eigenvalues

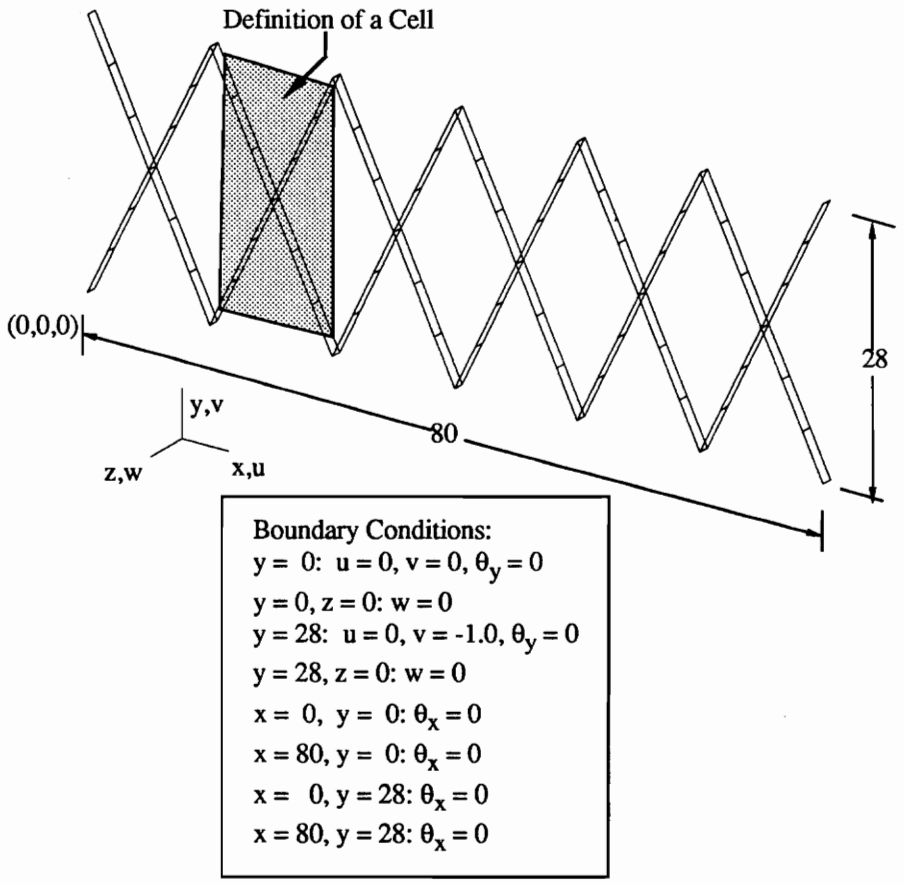

Fig. 3.4 – Six-cell Cross-Stiffened Open-web Truss.

Table 3.1 – Lowest Eight Eigenvalues for the Six-Cell Open-Web Truss.

Sequence	Eigenvalue	Set
1	1.0000	In-plane
2	1.0326	In-plane
3	1.1286	In-plane
4	1.1890	Out-of-plane
5	1.1891	Out-of-plane
6	1.1892	Out-of-plane
7	1.1894	Out-of-plane
8	1.1896	Out-of-plane

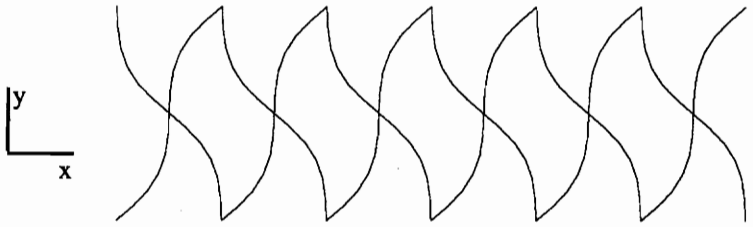

a – First Buckling Mode.

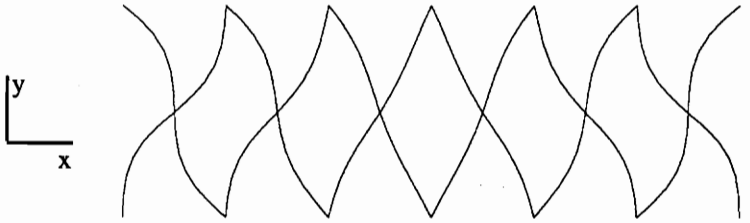

b – Second Buckling Mode.

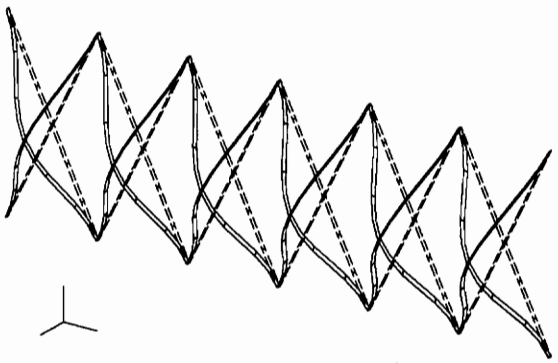

c – Fourth Buckling Mode (First Out-of-plane).

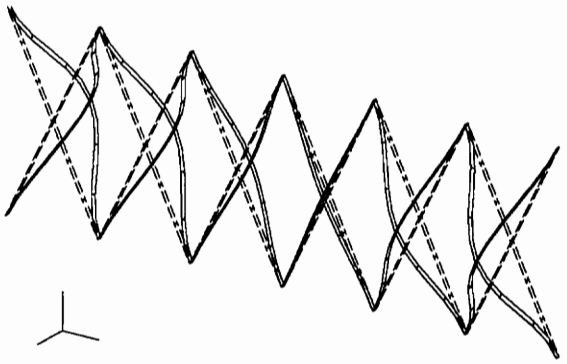

d – Fifth Buckling Mode (Second Out-of-plane).

Fig. 3.5 – Four Buckling Modes for the Open-web Truss Structure.

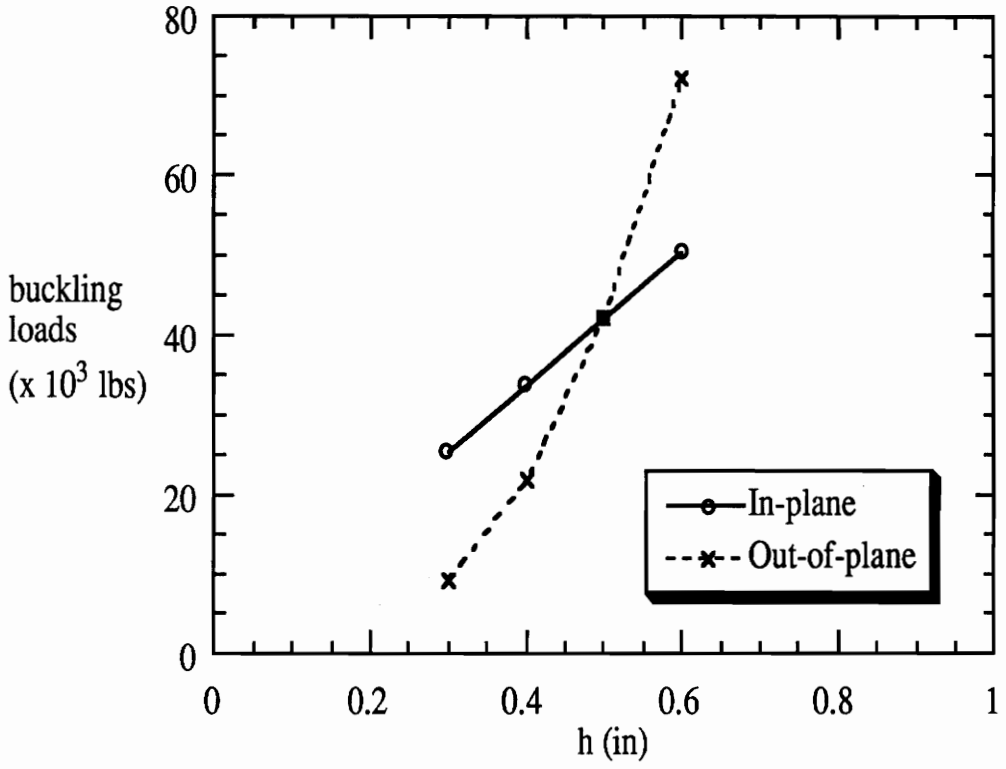

Fig. 3.6 – Variation of the First and Fourth Critical Loads with Respect to h.

associated with two different modes become closely spaced and start switching places. In the case of the open-web truss structure discussed above, for example, convergence problems result in the generation of designs for which the lowest in-plane and out-of-plane buckling modes become alternatively critical.

An alternate strategy is proposed in the present study. It is based on the observation that the eigenvalues can be grouped based on the values of their derivatives with respect to the design variables. Each group contains eigenvalues with derivatives of similar magnitudes. A buckling constraint is then imposed only on the lowest eigenvalue found in each group. For example, in the case of the open-web truss, the first three eigenvalues vary as a group, as the design is changed, without switching places within the group. Conseqently, a single buckling constraint can be used to control these eigenvalues. The implementation of this procedure can be visualized by forming a $(p \times n)$ matrix of eigenvalue derivatives, where n is the number of design variables and p is the number of eigenvalues contained in a specified range. The range of eigenvalues that must be examined depends on the buckling response of the structure and has been set to $1.2\lambda_1$. In order to select the eigenvalues that would be included in the constraint set, the derivative of each eigenvalue with respect to a design variable is compared with the derivative of the lowest eigenvalue with respect to the same design variable. If the difference is larger than a specified threshold, an additional constraint is set up for the higher eigenvalue with a new value $\overline{v}_k$ (see Eq. (3.3)). In the present study, a practical (but arbitrary) threshold of 20% has been used. For example, the derivatives of the lowest eight eigenvalues of the open-web truss problem with respect to the design variables are shown in Table 3.2. Since the derivatives of the second eigenvalue (second row) are not significantly different from the ones corresponding to the first eigenvalue, λ_2 would not be included in the constraint set. However, the derivatives of the fourth eigenvalue, the first out-of-plane buckling mode, are significantly different from the derivatives found

in the first row. Thus, a buckling constraint would be set up to constrain the fourth eigenvalue. Once the eigenvalues that must be constrained have been selected, the use of slightly increasing values for $\overline{v}_2$, $\overline{v}_3$, ... in equation (3.3) precludes the apparition of coalescent eigenvalues.

The number of groups of eigenvalues considered at a specific design point depends on several characteristics of the problem at hand. First, the thresholds for the identification of groups of eigenmodes (currently set to 20%) will affect the number of buckling constraints that will be set up. Secondly, the choice of the design variables will also influence the buckling response. For example, suppose that the thickness and height of each pair of members forming the cells of the open-web truss structure discussed above were allowed to vary independently. Then, as the optimizer starts changing the dimensions of each member independently, the number of groups of eigenvalues that need to be considered will progressively increase.

The procedure has been implemented in the optimization system and tested on several open-web truss and cylindrical composite shell configurations. In all the cases considered, only one buckling constraint, corresponding to the lowest eigenvalue, was imposed on the initial design. Additional buckling constraints were automatically added as the lowest eigenvalues of successive groups were approaching each other.

3.4 Examples

In this section, three examples are presented to demonstrate the capabilities of the new optimization system. They also validate the implementation of the processors and procedures that have been developed to build the optimization system. The examples considered are geodesically stiffened panels. This stiffening concept has been defined in Chapter 1 and will be studied in more detail starting in Chapter 4. This type of stiffening has recently received more attention [2,12,13,30], principally due to its potential in

Table 3.2 – Derivatives of the lowest Eight Eigenvalues with Respect to the Design Variables.

Sequence i	$\frac{d\lambda_i}{dt}$	$\frac{d\lambda_i}{dh}$
1	−4.365	−1.357
2	−4.502	−1.401
3	−4.906	−1.531
4	−1.760	−4.809
5	−1.760	−4.809
6	−1.761	−4.810
7	−1.761	−4.810
8	−1.761	−4.811

terms of geometric tailoring, weight savings, increased damage tolerance and ease of manufacturing.

In the first two examples, optimum designs with respect to weight are obtained while satisfying constraints due to buckling as well as lower and upper bounds on layer thicknesses and stiffener cross section dimensions. In the third example, material failure constraints are also considered. The Sequential Convex Programming (SCP) algorithm combined with the Modified Method of Feasible Directions and the Bounded Polynomial Interpolation has been chosen to solve the optimization problem. In the SCP, conservative approximations are used during the optimization of the convex sub-problem. These approximations may cause the eigenvalues associated with the different buckling modes of the structure to switch following a move in the design space. For all the examples presented in the present study, move limits have been used. The move limits were set between 10% and 20% for the initial design and multiplied by 0.8 every time the most critical constraint obtained at a specific design point was more positive than at the previous design point and larger than 0.001.

The finite element results have been obtained with the CSM Testbed using the continuum-based nine-node quadrilateral shell element implemented in processor ES1 (element EX97). The computations were performed on a Convex C220 computer located at NASA Langley Research Center.

3.4.1 Example 1

The first example focuses on the optimal design of composite wing rib open-web trusses. Rib dimensions of 28 inches high by 80 inches wide are used. The configuration shown in Fig. 3.4 is a 6-cell open-web truss and the boundary conditions used for the analysis are indicated in the figure. Uniform unit displacements are applied at the top edge of the truss (y = 28 in) to simulate a uniformly distributed compressive load. Each

member is discretized using 6 9-node shell elements, and only one element is placed along the height of the members since the structural response presents no strong gradients in this direction.

A minimum-weight design corresponding to a compressive load N_y of 1,000 pounds per inch (lb/in) is sought subject to buckling resistance constraints. The design variables represent the thickness t and height h (z–direction in Fig. 3.4) of the stiffeners. Only one laminate is considered, and all its plies are oriented at 0° with respect to the axis of each member. The number of cells in the x–direction (see Fig. 3.4) is varied in an incremental fashion to determine the optimal configuration. The minimum weights obtained are plotted in Fig. 3.7. This figure indicates that a minimum weight design corresponds to six cells along the length of the panel.

This example clearly demonstrated the utility of the procedure described in Section 3.3.4 that automatically groups the eigenvalues and sets up an appropriate number of buckling constraints. For all the configurations considered, two buckling constraints, corresponding to an in-plane and an out-of-plane buckling mode, are active at the optimum. The buckling modes corresponding to the lowest in-plane and out-of-plane buckling modes are shown in Figs. 3.5a and 3.5c. Their corresponding critical loads are 79745 and 82041 lb. Note that both buckling constraints are critical since values of $\overline{v}_1$ and $\overline{v}_2$ of 1.0 and 1.025, respectively have been used in Eq. (3.3). Verification of the Kuhn-Tucker optimality conditions [29] has shown that the final designs obtained correspond to optimal designs.

3.4.2 Example 2

This example presents the optimum design of a composite wing rib panel under a combined compression shear load. The rib dimensions correspond to those used in the previous example and are shown in Fig. 3.8 along with the boundary conditions. The

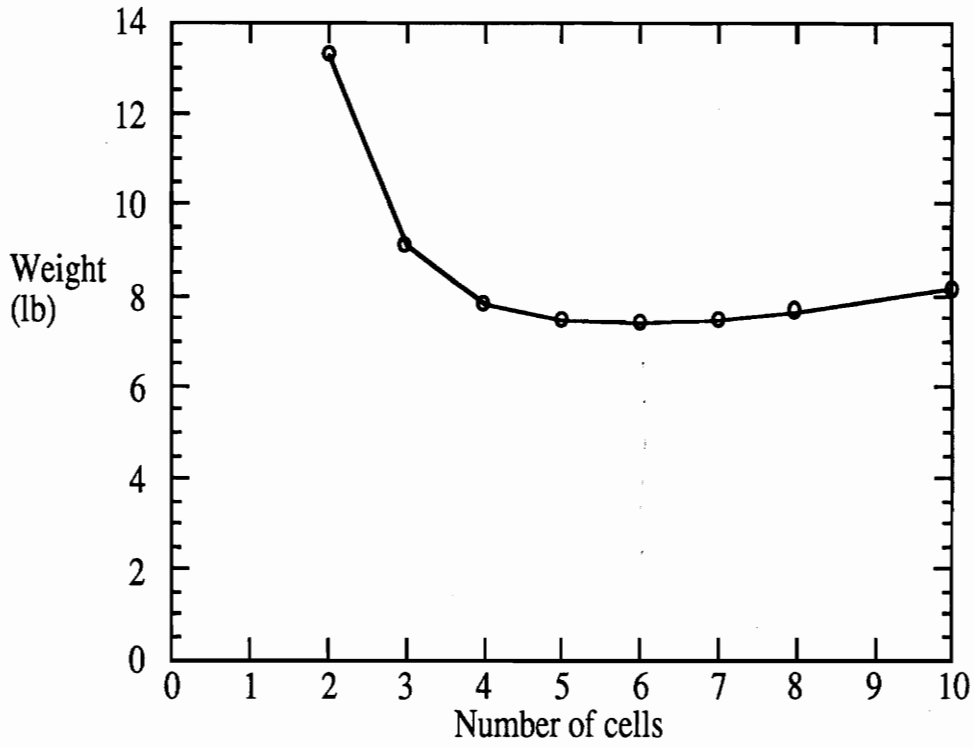

Fig. 3.7 – Structural Efficiency of Open-web Trusses Subjected to Uniform Compressive Loading.

stiffeners are symmetrically placed with respect to the skin and an 8-cell configuration is chosen. The skin lamination sequence is symmetric and present plies oriented at -45°, 45°, 90°, and 0°, the -45° plies being the outer plies and the 0° plies being adjacent to the middle plane of the skin (see Fig. 3.8 for the definition of the lamination angle in the skin). The final thickness of the plies correspond to the value of the first design variable. All the plies in the stiffeners are oriented along the length of the members. The panel is subjected to equal magnitudes of shear N_{xy} and uniaxial compression N_y of 1,000 $lb/in.$

The finite element model of the stiffened panel includes a total of 256 9-node elements and 1073 six-degree-of-freedom nodes. The skin is modelled with 128 (32 by 4) elements and each stiffener is discretized with 4 elements. Two sets of nonzero displacement boundary conditions are used to simulate, respectively, the compressive and the shearing component of the loading. The complete structural response is obtained by superposing the scaled structural responses obtained by applying successively each set of nonzero displacement boundary conditions.

The optimization problem consists of minimizing the total weight f of the panel subject to buckling constraints g_b as well as lower and upper bounds on the design variable values. Three design variables are used. The first design variable, x_1, corresponds to the thickness of the contiguous plies oriented at any specific angle in the skin of the panel. For example, x_1 in of 90° plies are placed on each side of the panel middle plane. Since a single design variable is used, all the plies oriented at a specific angle have the same thickness, and the thickness of the skin is eight times the value of the first design variable. The second and third design variables, x_2 and x_3, correspond, respectively, to the thickness and height (z–direction in Fig. 3.8) of the stiffeners.

The history of the optimization run and the minimum weight reached after 10 design iterations are shown in Fig. 3.9. It can be seen that after the first 5 iterations the weight reduction rate was small, and that convergence occurred after a plateau had been reached.

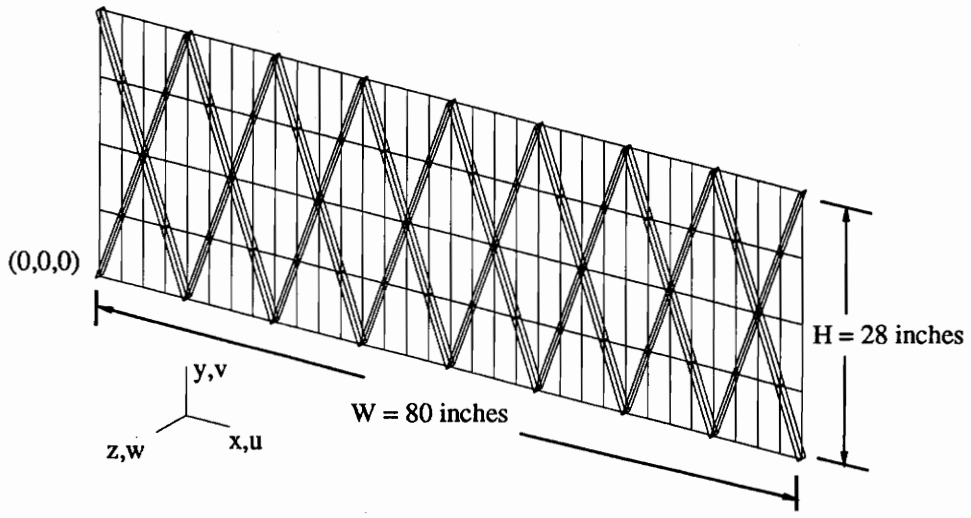

Note: Angle of lamination in the skin is measured with respect to the x-axis.

Boundary Conditions:

y=0: u=0,v=0,θ_y=0
y=0, z=0: w=0

y=28: θ_y=0
Compression: u=0,v=-1.0
Shear: u=-1.0,v=0
y=28, z=0:w=0

x=0: θ_x=0
Compression: u=0,v=-y/H
Shear: u=-y/H,v=0
x=0, z=0:w=0

x=80: θ_x=0
Compression: u=0,v=-y/H
Shear: u=-y/H,v=0
x=80,z=0: w=0

Fig. 3.8 – Eight-Cell Geodesically Stiffened Panel, Finite Element Model and Boundary Conditions.

For this example, the convergence criterion specifies that convergence occurs when the relative change in the value of the objective function is smaller than 0.2%. More detailed results are presented in Table 3.3. In the first three columns, the values of each design variable are presented. The value of the first buckling constraint and the objective function (weight) are given in the fourth and fifth columns. The last column gives the derivatives of the first buckling constraint with respect to each design variable. Note that, because the constraints are posed as $g_j(\mathbf{x}) \leq 0$ (see Eq. (3.1)), a negative gradient component indicates that an increase in the value of the design variable would result in a less critical constraint. The weight reduction achieved during the last design iterations mainly comes from the reduction in the value of the stiffener thickness (design variable x_2). Note that, since the stiffeners are made of unidirectional material, their thickness should probably be limited by design factors that have not been included in this example, such as damage tolerance considerations. The CPU time required for a single analysis of the structure can be broken up into two components. The first component corresponds to the linear analysis of the structure and the calculation and assembling of the geometric stiffness matrix. The second component represents the calculation of the eigenvalues of the buckling problem. The CPU time corresponding to the first component was 143 s, and the CPU time for an iteration in the eigensolver was 15 s. The number of iterations in the eigensolver varies during the optimization run, but generally decreases as the optimization progresses. In this case, an average of 9 iterations were required at each design point.

At the optimum, several buckling constraints, which correspond to different skin buckling modes, are active. To make the stiffener buckling modes become critical, the convergence criterion must be thightened so that few more design iterations are performed thus yielding stiffener dimensions that will make buckling of these members become critical. By thightening the convergence criterion, a final design for which both

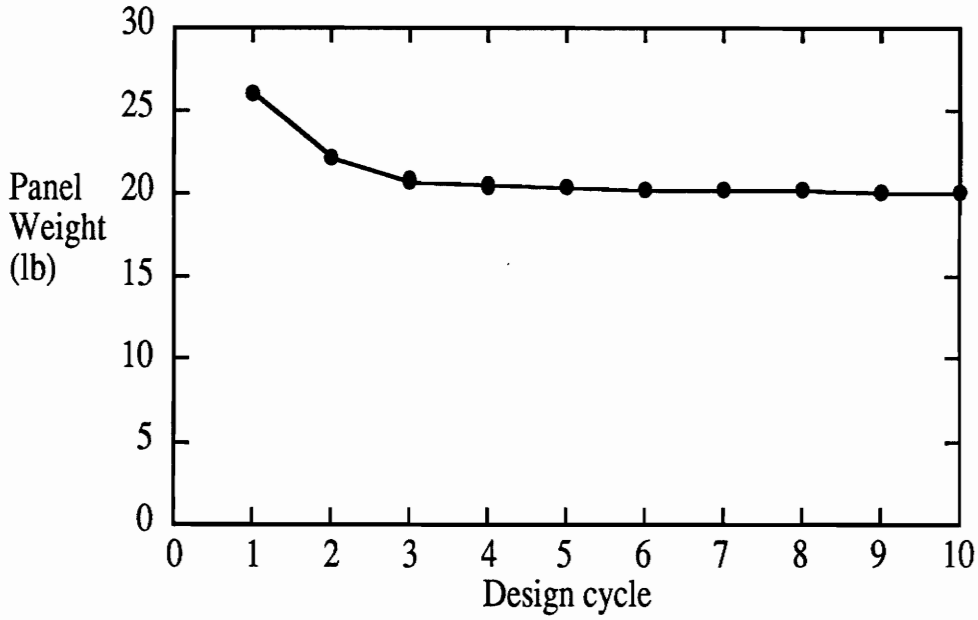

Fig. 3.9 – Eight-Cell Panel, History of the Optimization Run

Table 3.3 – History of the Optimization Run for the Eight-Cell Geodesically Stiffened Panel.

x_1 *inch*	x_2 *inch*	x_3 *inch*	g_{b1}	f *lb*	$\frac{\partial g_{b1}}{\partial x_i}$
0.02	0.15	0.6912	-0.7082	26.05	<-108.2,-7.820,-3.440>
0.01753	0.1201	0.6606	-0.1618	22.20	<-87.65,-6.403,-2.408>
0.01671	0.1018	0.6827	-0.0209	20.83	<-86.64,-6.309,-1.911>
0.01656	0.08944	0.7484	-5.398E-3	20.54	<-147.6,-3.800,-0.5948>
0.01678	0.07693	0.7785	-5.308E-3	20.39	<-146.1,-4.156,-0.5526>
0.01679	0.07415	0.7883	1.212E-4	20.32	<-145.4,-4.237,-0.5363>
0.01680	0.07284	0.7945	3.207E-4	20.30	<-145.4,-4.280,-0.5258>
0.01683	0.06557	0.8581	-1.363E-4	20.24	<-148.0,-4.534,-0.4164>
0.01705	0.05704	0.8915	-4.637E-3	20.17	<-147.1,-4.985,-0.3793>
0.01707	0.05425	0.9103	-6.194E-4	20.12	<-146.4,-5.156,-0.3602>

stiffener and skin buckling modes are critical has been obtained. This new design is 0.08% heavier than the one given in Table 3.3. The slight increase in weight is due to the approximations used in the solution of the optimization problem which resulted in the switching of the skin and stiffener buckling modes. For this new design, skin buckling corresponds to the second buckling constraint and a limiting value $\overline{v}_2$ slightly larger than the value of $\overline{v}_1$ ($\overline{v}_2 = 1.0025\overline{v}_1$) is used in equation (3.3).

The combined loading condition has been introduced using the scaling and superposition strategies implemented in the procedure `analysis` described in Section 3.3.3. In this case, the use of displacement boundary conditions for the application of the loading is forced by the fact that the fraction of the load carried by the stiffeners is unknown and varies as the design is changed. Therefore, the values of the nodal forces that should be applied to the stiffener and skin nodes are also unknown and cannot be used to introduce the loading.

3.4.3 Example 3

The calculation of practical designs for composite structures typically requires the consideration of a relatively large number of design variables. To demonstrate that such structures can be designed with the optimization system, the design of a composite wing rib panel that presents skin sections with different lamination sequences is performed. The rib dimensions correspond to those used in the two previous examples and are shown in Fig. 3.10a along with the boundary conditions. The stiffeners are symmetrically placed with respect to the skin and a 3-cell configuration is considered. The stacking sequences in the skin are as indicated in Fig. 3.10b. The underlying base laminate is reinforced in the middle cell by additional plies symmetrically placed with respect to the middle plane of the panel. The stiffeners are made of unidirectional material. The panel is subjected to an axial stress resultant N_y of 5000 lb/in.

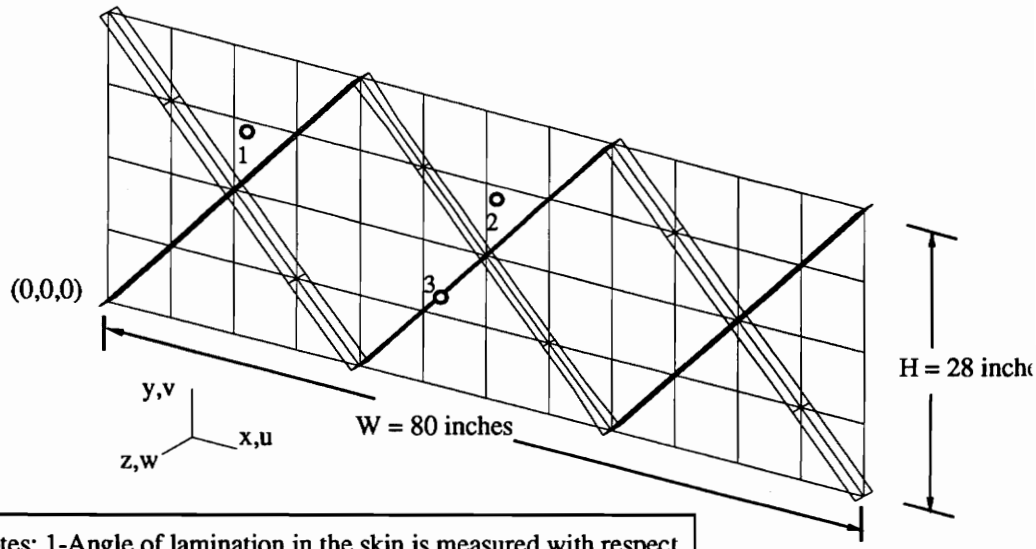

Notes: 1-Angle of lamination in the skin is measured with respect to the x-axis.

2-Empty circles indicate the location of the evaluation of the material failure constraints.

Boundary Conditions:

y=0: u=0,v=0,θ_y=0	**x=0**: θ_x=0
y=0, z=0: w=0	u = 0
	x=0, z=0:w=0
y=28: θ_y=0	**x=80**: θ_x=0
u=0,v=-1.0	u = 0
y=28, z=0: w=0	x=80,z=0: w=0

a – Model and Boundary Conditions.

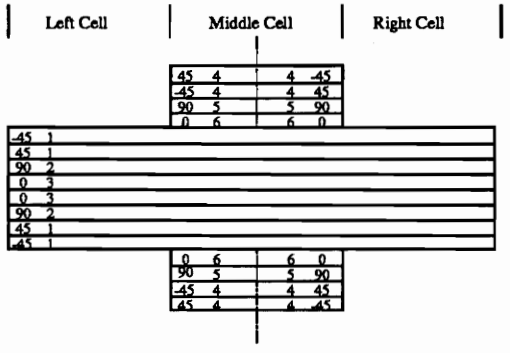

b – Skin Stacking Sequences.

Fig. 3.10 – Three-Cell Geodesically Stiffened Panel.

The finite element model of the stiffened panel includes a total of 96 9-node elements and 413 six-degree-of-freedom nodes. The skin is modelled using 48 (12 by 4) elements and each stiffener is discretized with 4 elements. Nonzero displacement boundary conditions are applied at the top (y = 28 in) to simulate the compressive loading.

The optimization problem consists of minimizing the total weight f of the panel subject to buckling constraints g_b, material failure constraints g_{f1}, g_{f2}, and g_{f3} imposed in the skin and the stiffeners (see Fig. 3.10a). The final design must also satisfy lower and upper bounds on the design variable values. The first six design variables, $x_1 - x_6$, are ply thickness design variables used to tailor the skin of the panel. Ply designations are given in Fig. 3.10b next to the ply angles. For example, x_1 designates the thickness of the $\pm 45°$ plies in the underlying base laminate. The seventh and eighth design variables designate the thickness and height of the stiffeners.

The history of the optimization run is shown in Fig. 3.11. It can be seen that 62 exact analyses or design iterations were required to reach a minimum weight of 49.7 lb. The final values of the design variables are given in Table 3.4. For comparison purposes, a baseline design, obtained by considering only three design variables corresponding to the skin thickness and the stiffener cross-section dimensions, had a final weight of 55.3 lb. This is a weight penalty of 11% compared to the 8 design variable problem. At the optimum, two buckling and three side constraints are critical. The first buckling constraint corresponds to a skin buckling mode and the second one corrresponds to the buckling of the stiffeners. The material failure constraints are inactive. For the final design, the Lagrange multipliers are $< 98.79, 70.08, 31.32, 19.06, 0.29 >$ and the results of the verification of the Kuhn-Tucker optimality conditions [29] are presented in Table 3.4.

In summary, these three examples have shown that the optimization system can be used to optimally design structures that present a complex buckling response. They have also demonstrated the utility of the scaling and superposition strategies implemented in

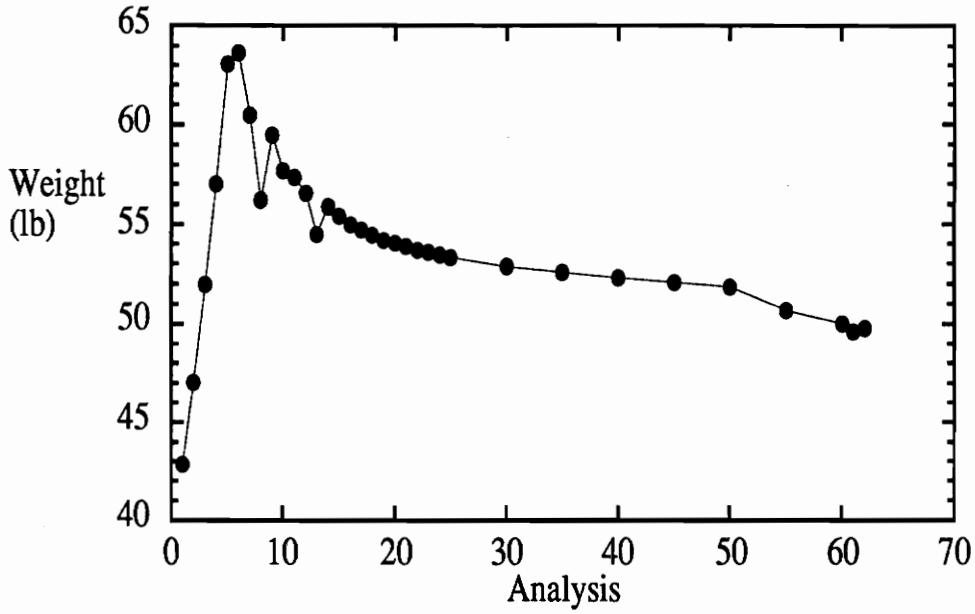

Fig. 3.11 – Three-Cell Panel, History of the Optimization Run.

Table 3.4 – Final Design for the Three-Cell Panel.

	Values	$\left\lvert \frac{\partial f/\partial x_i}{\sum_{j=1}^{r} \lambda_j \frac{\partial g_j}{\partial x_i}} \right\rvert$
x_1 (in)	0.005†	1.00
x_2 (in)	0.129	1.01
x_3 (in)	0.022	0.99
x_4 (in)	0.005†	1.00
x_5 (in)	0.017	1.00
x_6 (in)	0.005†	1.00
x_7 (in)	0.094	0.98
x_8 (in)	2.35	1.03
f (lb)	49.8	

† Lower bound.

the procedure `analysis` for the application of combined loading conditions. Finally, the last example has shown that the optimization system can also be used to obtain practical solutions for problems that involve a relatively large number of design variables.

Chapter 4
Analysis of Composite Cylindrical Shells

As indicated in Chapter 3, the constraints imposed on the design of the cylindrical shells considered in the present study are evaluated using the results of a finite element analysis. Two limiting failure modes are considered. The first failure mode is the buckling of the shell in either an overall or a localized mode, and the second is material failure, where first-ply failure in the skin or stiffeners is considered. In this chapter, the details of the structural analysis of the different cylindrical shell configurations considered in the design study are presented. In Section 4.1, the specific element used is briefly described. Then, in Section 4.2, the finite element models and the specific boundary conditions used for the analysis of each configuration in the case of compressive and torsional loadings are presented. Finally, in Section 4.3, characteristics of the behavior of geodesically stiffened shells are discussed.

4.1 Finite Element Formulation

The only element type used in the present study is the quadrilateral 9-node shell element called EX97 that has been installed in processor ES1 of the CSM Testbed. Its formulation is that of a continuum-based theory which leads to degenerated 3D shell elements [31]. EX97 represents the assumed-natural strain (ANS) implementation of this formulation [32]. The out-of-plane deflections and bending rotations are approximated independently and this results in a C^o continuity of the primary variables. This also implies that the effects of transverse shear deformation are taken into account through the use of a first-order shear deformation theory. The primary motivation behind the development of these shell elements has been the construction of simple and efficient finite

elements for plates and shells that are locking-free and fit naturally into displacement-based programs. They also yield accurate answers for coarse meshes.

4.2 Finite Element Models

The finite element models used in the design study are presented in this section. Although the optimization system described in Chapter 3 can be used in conjunction with any finite element model, the optimization of a structure discretized with a refined mesh may become computationally very expensive. To reduce the computational cost, partial models and symmetry boundary conditions are used. In all cases, the mesh is rectangular in topology, and restricted to 9-node quadrilateral shell elements. Each finite element model is defined as a m_{ne} x n_{ne} x l_{ne} mesh where m_{ne} is the number of elements in the axial direction, n_{ne} is the number of elements in the circumferential direction, and l_{ne} is the number of elements along the height of the stiffeners. In the case of unstiffened shells, only m_{ne} and n_{ne} need to be specified. The boundary conditions are imposed in a cylindrical coordinate system. The radial, circumferential, and axial displacements are respectively denoted by u_r, u_θ, and u_x. Similarly, rotations around the radial, circumferential, and axial axes are denoted by θ_r, θ_θ, and θ_x.

Following the presentation of each model, the results of a mesh refinement study are given to assess the capability of the mesh density chosen for the design study to accurately predict the two lowest eigenvalues of the buckling problem. For the mesh convergence study, a nominal design has been chosen. The skin is 0.08 in thick with a quasi-isotropic lamination sequence of $[-45_2/+45_2/90_2/0_2]_S$, where the lamination angle in the skin is measured with respect to the axis of the cylinder. In the case of geodesically stiffened shells, the geodesic stiffeners and the rings are 1.5 in high and are 0.1 and 0.2 in thick, respectively. The lamination sequences for the geodesic stiffeners and the rings are $[0_{20}]_T$ and $[0_{40}]_T$, respectively, where the lamination angle in the stiffeners is

measured with respect to their axis. For conventionally stiffened shells, the rings are identical to those used for the geodesically stiffened shells and the stringers are 1.5 in high and 0.1 in thick. For each case, the eigenvalues have been normalized with respect to the lowest eigenvalue obtained with the most refined mesh.

4.2.1 Axial Compression

The finite element models used in the case of the unstiffened shell as well as the geodesically and conventionally stiffened configurations subjected to axial compression are presented in this section. For the unstiffened shell, four different meshes have been used for the mesh refinement study. The model with 144 (12x12) quadrilateral shell elements and 625 nodes is shown in Fig. 4.1. It represents a partial (L/2x90°) shell-element-based model of the cylindrical shell. Symmetry conditions BC2 and BC3 are respectively imposed at midlength and at $\theta = 0°$ and 90°. The remaining edge is clamped and the axial force is imposed by specifying the nonzero displacement boundary conditions u_o at every node located on this edge. The first two eigenvalues obtained with each mesh density are presented in Table 4.1. The lowest eigenvalue obtained with the 12x12 mesh is within 2% of the one obtained with the most refined mesh and, therefore, the 12x12 mesh is used for the design study.

For the geodesically stiffened shell, different numbers of cells are considered in the axial and circumferential directions (see Section 2.3 for a discussion of the scope of the design study). For these structures, the model used depends on the number of cells in the axial direction. In the cases of one, two, and three cells in the axial direction, the partial model represents the entire length with one cell in the circumferential direction. See Fig. 4.2a. Each cell is discretized with a mesh of 8x8 quadrilateral shell elements. Eight shell elements are used for each stiffener. Symmetry boundary conditions BC3 are imposed along the edges located at $\theta = 0°$ and (360°/N), where N is the number of cells

L = 100 in
R = 85 in

BC1: $u_r = 0, u_\theta = 0, u_x = u_o, \theta_\theta = 0$

BC2: $u_x = 0, \theta_\theta = 0$

BC3: $u_\theta = 0, \theta_x = 0$

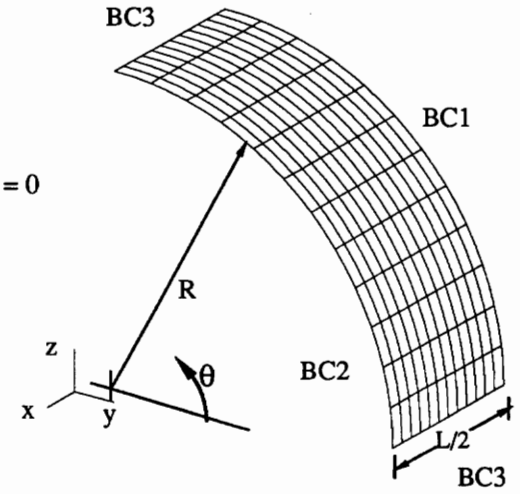

Fig. 4.1 – Model of the Unstiffened Shell Subjected to Compression.

in the circumferential direction. On the two remaining edges, the displacements in the circumferential direction and the rotations with respect to the same axis are restrained. The axial force is introduced by specifying the nonzero displacement boundary conditions u_o at all the nodes located on these edges. For four and eight cells in the axial direction, the partial model represents half the length with one cell in the circumferential direction. See Fig. 4.2b. The mesh refinement is identical to the one used in the case of two cells in the axial direction. The same boundary conditions are also used except that the boundary conditions BC4 are replaced by the symmetry boundary conditions BC2. The mesh refinement study has been performed using the 2x16 configuration (see Fig. 2.2). The results are as indicated in Table 4.2. In this case, the mesh chosen for the design study (16x8x1) predicts the lowest eigenvalue of the buckling problem within 9.5% of the one obtained with the most refined mesh.

For the conventionally stiffened shell, three different configurations, 2x8, 2x24, and 2x32 are studied under axial compression. Since they all have only 2 cells in the axial direction, the same partial model is used in all cases. The partial model discretizes the entire length with one cell in the circumferential direction, see Fig. 4.3. Since the first buckling mode presents a short wavelength pattern in the axial direction and only 1 half-wave between each stringer, 24 elements are placed in the axial direction and only 8 in the circumferential direction. Therefore, the skin is discretized with 192 quadrilateral shell elements. Each stringer is discretized with 24 elements and eight elements are placed along each ring (24x8x1 mesh). There are 288 elements and 1211 nodes in the finite element model. The boundary conditions applied to the model are identical to those used for the two cell geodesically stiffened geometry (see Fig. 4.2a). The mesh refinement study has been performed using the 2x8 configuration (see Fig. 2.3). The results are as indicated in Table 4.3. In this case, the lowest eigenvalue predicted with the mesh chosen for the design study (24x8x1) is within 1.0% of the one obtained with

the most refined mesh.

4.2.2 Torsion

The finite element models used in the case of the unstiffened as well as the geodesically and conventionally stiffened configurations subjected to torsion are presented in this section. The model used for the unstiffened shell is shown in Fig. 4.4. It represents the entire shell (Lx360°) and it has 6 elements along the length and 36 around the circumference (6x36 mesh). It includes a total of 216 elements and 936 nodes. The shell is clamped at each end and the loading is applied by imposing nonzero displacement boundary conditions. The use of the entire model has been forced by the lack of symmetries of the first buckling mode with respect to the midlength and the generator. The results of the mesh refinement study are indicated in Table 4.4. As indicated by the results obtained with the 6x24 and 12x24 meshes, refining the mesh in the axial direction does not result in a significant improvement in the accuracy of the computed eigenvalues. This is due to the low number of axial half-waves presented by the first buckling shape which require only a small number of elements to be accurately modelled.

For the geodesically stiffened shell, different number of cells are considered in the axial and circumferential directions. For these structures, all the partial models discretize the entire length, and the number of cells modelled in the circumferential direction depends on the specific configuration. For the 2x4, 2x8, 2x16, and 2x24 configurations, short half-waves well contained within each cell are obtained. Therefore, only 3 cells in the circumferential direction need to be discretized. Although for the 3x24 and 4x24 configurations the same buckling pattern is obtained, 4 cells in the circumferential direction have been discretized to decrease the effect of the boundary conditions imposed at θ = 0° and 15° on the buckling response. For the 2x32 configuration, the first buckling mode presents long half-waves that extend over the entire length of the shell (see Fig. 5.4d).

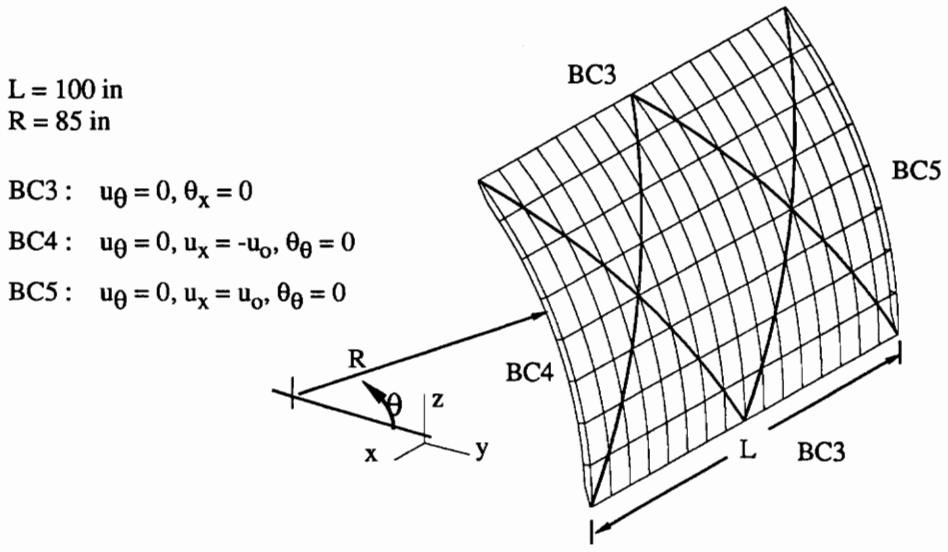

a – 2 Cells in the Axial Direction.

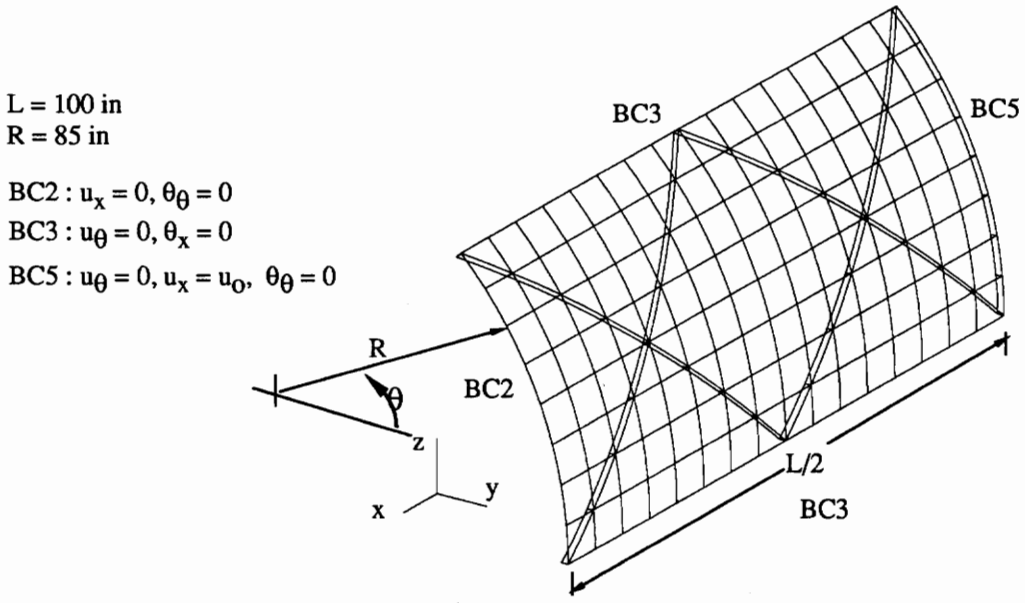

b – 4 and 8 Cells in the Axial Direction.

Fig. 4.2 – Models of the Geodesically Stiffened Shell Subjected to Compression.

L = 100 in
R = 85 in

BC3 : $u_\theta = 0, \theta_x = 0$

BC4 : $u_\theta = 0, u_x = -u_o, \theta_\theta = 0$

BC5 : $u_\theta = 0, u_x = u_o, \theta_\theta = 0$

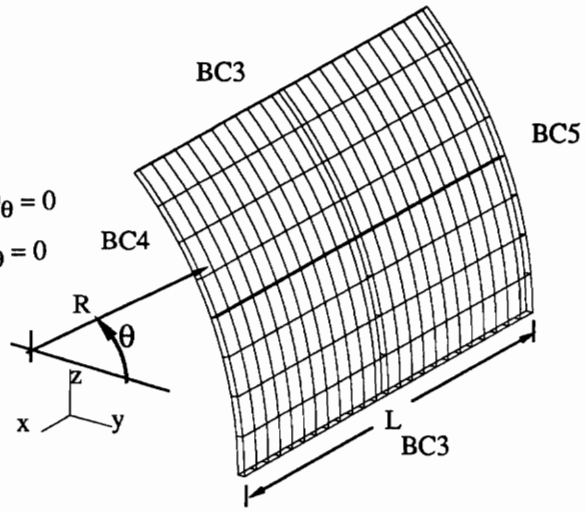

Fig. 4.3 – Model of the Conventionally Stiffened Shell Subjected to Compression.

Table 4.1 – Results of the Mesh Refinement Study for the Unstiffened Shell under Axial Compression

Mesh	λ_1	λ_2
9x9	1.081	1.083
12x12	1.020	1.030
18x18	1.004	1.009
24x24	1.000	1.001

Table 4.2 – Results of the Mesh Refinement Study for the Geodesically Stiffened Shell under Axial Compression.

Mesh	λ_1	λ_2
12x6x1	1.198	1.232
16x8x1	1.095	1.106
24x12x1	1.013	1.037
32x16x1	1.000	1.003

Table 4.3 – Results of the Mesh Refinement Study for the Conventionally Stiffened Shell under Axial Compression.

Mesh	λ_1
16x8x1	1.025
16x16x1	1.012
24x8x1	1.010
30x8x1	1.008
30x16x1	1.000

L = 100 in
R = 85 in

BC6: $u_r = 0, u_\theta = u_o, u_x = 0, \theta_\theta = 0$

BC7: $u_r = 0, u_\theta = -u_o, u_x = 0, \theta_\theta = 0$

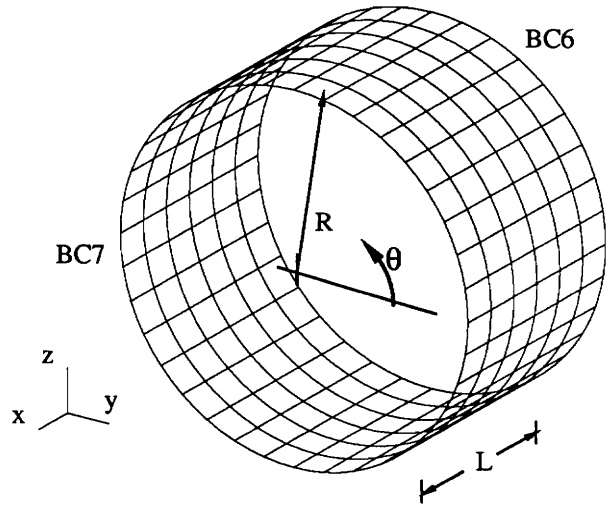

Fig. 4.4 – Model of the Unstiffened Shell Subjected to Torsion.

Thus, the effect of the symmetry boundary conditions tend to influence a larger portion of the domain. To reduce their effect, 9 cells have been modelled in the circumferential direction. However, the consideration of 9 cells in the circumferential direction does not change the boundary conditions that must be applied along the generators. Consequently, only the model that discretizes 3 cells in the circumferential direction is described. It is shown in Fig. 4.5. The skin is discretized with 216 quadrilateral shell elements. Twelve elements are placed along the length and eighteen in the circumferential direction. Six shell elements are used for each stiffener (12x18x1 mesh). There are 324 elements and 1333 nodes in the finite element model. Boundary conditions BC10 are imposed along the edges located at $\theta = 0°$ and (360°/(N/3)) (360°/(N/9) for the 2x32 configuration). Imposing $u_r = 0$ along these two edges allows to exclude a local buckling mode that develops along these edges when u_r is free. On the two remaining edges, the displacements in the axial direction and the rotations with respect to the circumferential direction are restrained. The shear force is applied by specifying nonzero displacement boundary conditions at all the nodes located on these edges. The mesh refinement study has been performed using a 2x24 configuration (see Fig. 2.2). The results are as indicated in Table 4.5a. In this case, the mesh chosen for all of the configurations, excluding the 2x32, (12x6x1) predicts the lowest eigenvalue of the buckling problem within 5% of the one obtained with the most refined mesh. For the 2x32 configuration, the computational requirements associated with the consideration of nine cells in the circumferential direction has forced the use of a coarser mesh. However, as previously mentioned, the first buckling mode presents a single half-wave within each cell. Consequently a mesh of 4x4/cell can be used as indicated by the results of the mesh refinement study presented in Table 4.5b.

For the conventionally stiffened shell, three different configurations, 2x8, 4x8, and 2x32 have been studied in torsion. For the 2x8 configuration, the low number of waves

L = 100 in
R = 85 in

BC8 : $u_\theta = u_o$, $u_x = 0$, $\theta_\theta = 0$

BC9 : $u_\theta = -u_o$, $u_x = 0$, $\theta_\theta = 0$

BC10: $u_r = 0$, $u_x = 0$, $\theta_x = 0$

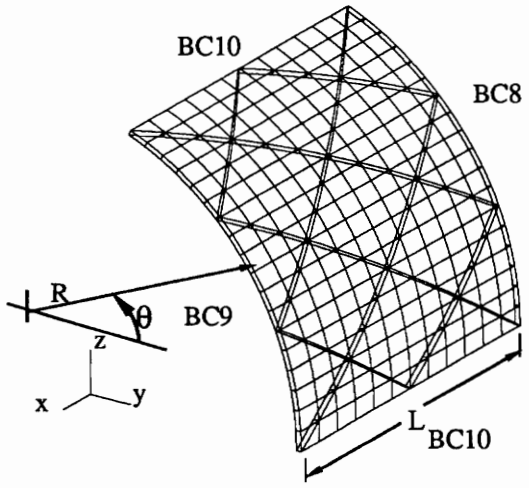

Fig. 4.5 – Model of the Geodesically Stiffened Shell Subjected to Torsion.

Table 4.4 – Results of the Mesh Refinement Study for the Unstiffened Shell under Torsion.

Mesh	λ_1	λ_2
6x24	1.05	1.13
6x36	1.02	1.11
12x24	1.05	1.13
6x48	1.00	1.09

Table 4.5 – Results of the Mesh Refinement Study for the Geodesically Stiffened Shell under Torsion.

a – All the Configurations, except the 2x32.

Mesh	λ_1	λ_2
12x18x1	1.05	1.06
16x24x1	1.00	1.00
20x30x1	1.00	1.00

b – 2x32 Configuration.

Mesh	λ_1
12x36x1	1.006
12x54x1	1.000

Table 4.6 – Results of the Mesh Refinement Study for the Conventionally Stiffened Shell under Torsion.

Mesh	λ_1	λ_2
6x24x1	1.038	1.118
6x36x1	1.035	1.118
12x24x1	1.003	1.063
18x24x1	1.000	1.063

presented by the first buckling mode has allowed the discretization of the complete shell. The resulting model is shown in Fig. 4.6a along with the boundary conditions. The skin is discretized with 288 quadrilateral shell elements. Six elements are placed along the length and 48 around the circumference. Each stringer is discretized with 6 elements (6x48x1 mesh). There are 480 elements and 2144 nodes in the finite element model. The displacement in the axial direction, u_x, and the rotation with respect to the circumferential direction, θ_θ, are restrained at both ends. The loading is applied with nonzero displacement boundary conditions at each end. To study the 4x8 configuration, the same mesh density has been used. Since only half of the circumference of the shell is discretized, symmetry boundary conditions BC10 are applied along the generators located at $\theta = 0°$ and $180°$. For the 2x32 configuration, the entire length of the shell and three cells in the circumferential direction are discretized using a 6x24x1 mesh. Consequently, six elements are placed along the length of the shell and 24 in the circumferential direction. Six shell elements are used for each stringer. The boundary conditions used for the 4x8 configuration are also applied for this configuration (see Fig. 4.6b). The mesh refinement study has been conducted using the 2x32 configuration (see Fig. 2.3). The results are as indicated in Table 4.6. Comparing the results obtained with the 6x24x1 and 6x36x1 meshes allow to conclude that no practical difference is obtained when the number of elements in the circumferential direction is increased. The mesh chosen for the design study (6x24x1) allows to predict the lowest eigenvalue of the buckling problem within 4% of the one obtained with the most refined mesh.

4.2.2 Combined Axial Compression and Torsion

The finite element models used in the case of combined axial compression and torsion are presented in this section. As for the other load cases, an unstiffened shell as well as conventionally and geodesically stiffened configurations are studied. For the unstiffened

L = 100 in
R = 85 in

BC8 : $u_\theta = u_o$, $u_x = 0$, $\theta_\theta = 0$

BC9 : $u_\theta = -u_o$, $u_x = 0$, $\theta_\theta = 0$

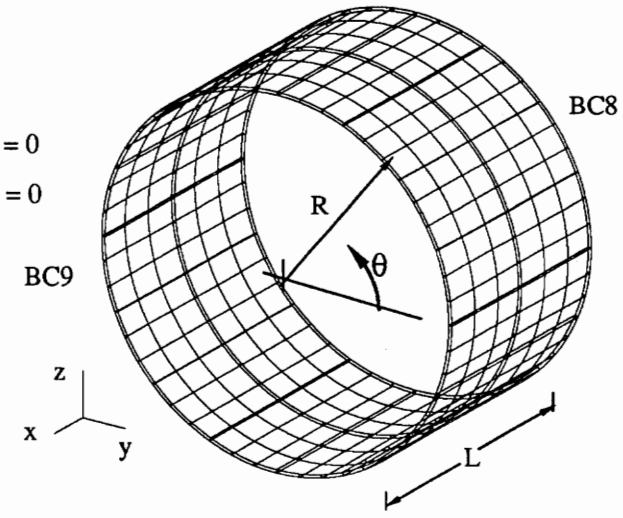

a – 2x8 Configuration.

L = 100 in
R = 85 in

BC8 : $u_\theta = u_o$, $u_x = 0$, $\theta_\theta = 0$

BC9 : $u_\theta = -u_o$, $u_x = 0$, $\theta_\theta = 0$

BC10: $u_r = 0$, $u_x = 0$, $\theta_x = 0$

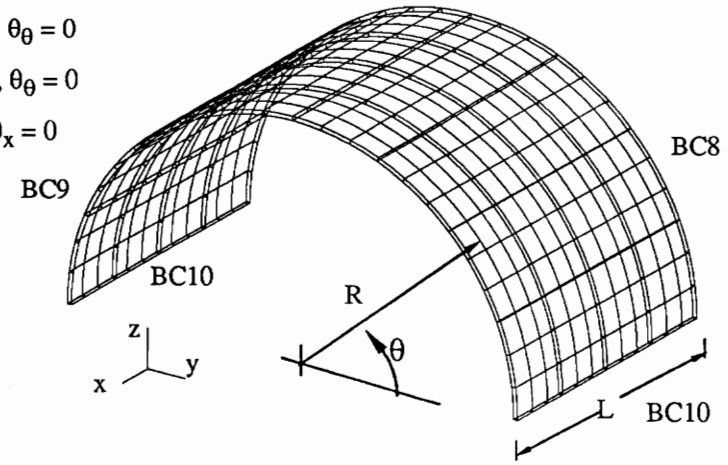

b – 4x8 Configuration.

Fig. 4.6 – Models of the Conventionally Stiffened Shell Subjected to Torsion.

shell, the model is presented in Fig. 4.7. It represents the entire shell (Lx360°) and it has 10 shell elements along the length and 40 around the circumference (10x40 mesh). It includes a total of 400 elements and 1680 nodes. The level of mesh refinement has been chosen based on the fact that, under combined compression and torsion of equal magnitudes, the first buckling mode resembles the one obtained under torsion only. It is recalled that under pure torsion, a 6x36 mesh allows to predict the lowest eigenvalue within 2% of the one obtained with a 6x48 mesh. Consequently, the 10x40 mesh should at least allow the same level of accuracy to be obtained. For the case of $N_x = 2700$ lb/in and $N_{xy} = 418.5$ lb/in, the model may be slightly less accurate. However, due computational considerations the same mesh refinement has been used.

The boundary conditions are such that the rotation around the circumferential direction, θ_θ, is restrained at both ends and the loading is introduced by imposing nonzero displacement boundary conditions. Because the same components of the static displacement vector are constrained for the compressive and torsional loadings, the two sets of boundary conditions can actually be considered as two different vectors of applied motions. Therefore, only successive forward eliminations and backward substitutions are required for the calculation of their respective static displacement solutions. Once these solutions have been calculated, they are scaled and superposed to obtain the resulting displacement field (see Section 3.3.3 for a discussion of the superposition and scaling procedures).

For the geodesically stiffened shells, only two configurations, 2x8 and 2x24, are studied under combined loads. For these studies, the model and mesh density are identical to the torsion case. The resulting model is shown in Fig. 4.8 along with the boundary conditions. As in the case of the unstiffened shell, the displacement solution corresponding to the combined loads is obtained by superposing the solutions obtained from each set of displacement boundary conditions.

L = 100 in
R = 85 in

BC11: Compression: $u_r = 0, u_\theta = 0, u_x = u_o, \theta_\theta = 0$

Torsion: $u_r = 0, u_\theta = u_o, u_x = 0, \theta_\theta = 0$

BC12: Compression: $u_r = 0, u_\theta = 0, u_x = -u_o, \theta_\theta = 0$

Torsion: $u_r = 0, u_\theta = -u_o, u_x = 0, \theta_\theta = 0$

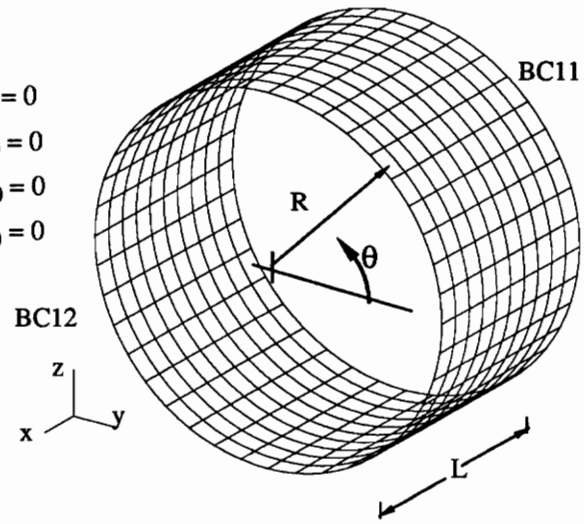

Fig. 4.7 – Model of the Unstiffened Shell Subjected to Axial Compression and Torsion.

L = 100 in
R = 85 in

BC11: Compression: $u_\theta = 0, u_x = u_o, \theta_\theta = 0$

Torsion: $u_\theta = u_o, u_x = 0, \theta_\theta = 0$

BC12: Compression: $u_\theta = 0, u_x = -u_o, \theta_\theta = 0$

Torsion: $u_\theta = -u_o, u_x = 0, \theta_\theta = 0$

BC13: Compression: $u_\theta = 0, u_x = (-2z/L + 1)u_o, \theta_x = 0$

Torsion: $u_\theta = (-2z/L + 1)u_o, u_x = 0, \theta_x = 0$

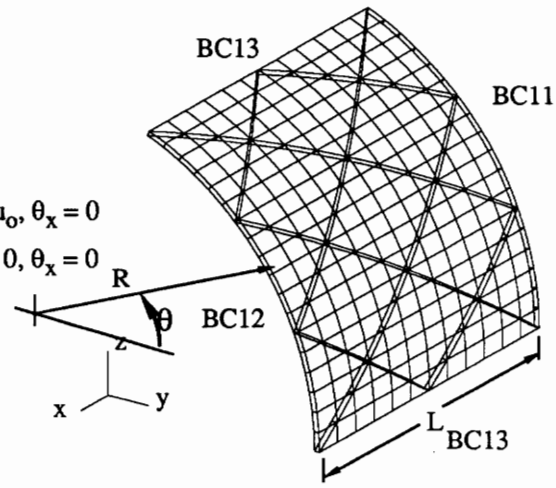

Fig. 4.8 – Model of the Geodesically Stiffened Shell Subjected to Axial Compression and Torsion.

For the conventionally stiffened shell, only two configurations, 2x8 and 2x24, are studied under combined loads. For the the load case N_x =1000 and N_{xy} =1000 lb/in, the model used in the case of torsion has been adopted, see Fig. 4.9a. The entire shell is discretized and six elements are placed along the length and 48 around the circumference. Six elements are placed along each stringer. For the load case N_x =2700 and N_{xy} =418.5 lb/in, a finer mesh is used in the axial direction to more accurately capture the first buckling mode since a short wavelength pattern is expected. For this second load case, the entire length of the cylinder and three cells in the circumferential direction are discretized, see Fig. 4.9b. Twenty-four elements are placed along the length of the cylinder and eighteen in the circumferential direction. As in the other cases of combined loads, the complete displacement solution is obtained by superposing the solutions obtained from each set of displacement boundary conditions.

4.3 Behavior of Geodesically Stiffened Shells

As evidenced by the literature review presented in Chapter 2, very little information is available on the analysis and the design of composite geodesically stiffened cylindrical shells. Moreover, most of the papers that have been published use a smeared stiffener approach which represents the skin-stiffener assembly by an equivalent homogeneous orthotropic plate. Since in the present study a small number of stiffeners is considered, it is expected that the discrete stiffener assembly will influence the local and overall behaviors of the shell. Consequently, such an approach is not used. The purpose of this section is to develop a better understanding of the behavior of geodesically stiffened shells and demonstrate that they can be tailored to suit the particular requirements of a specific loading regime.

Results of preliminary studies indicate that under compressive loading, the structural behavior of the geodesically stiffened shell falls in either one of the following two

L = 100 in
R = 85 in

BC11: Compression: $u_\theta = 0, u_x = u_o, \theta_\theta = 0$

Torsion: $u_\theta = u_o, u_x = 0, \theta_\theta = 0$

BC12: Compression: $u_\theta = 0, u_x = -u_o, \theta_\theta = 0$

Torsion: $u_\theta = -u_o, u_x = 0, \theta_\theta = 0$

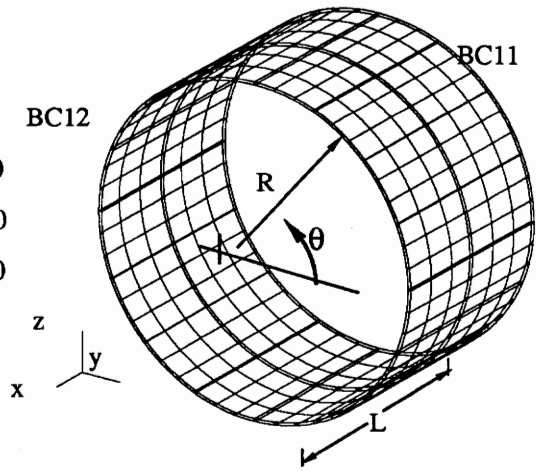

a – 2x8, $N_x = N_{xy} = 1000$ lb/in.

L = 100 in
R = 85 in

BC11: Compression: $u_\theta = 0, u_x = u_o, \theta_\theta = 0$

Torsion: $u_\theta = u_o, u_x = 0, \theta_\theta = 0$

BC12: Compression: $u_\theta = 0, u_x = -u_o, \theta_\theta = 0$

Torsion: $u_\theta = -u_o, u_x = 0, \theta_\theta = 0$

BC13: Compression: $u_\theta = 0, u_x = (-2z/L + 1)u_o, \theta_x = 0$

Torsion: $u_\theta = (-2z/L + 1)u_o, u_x = 0, \theta_x = 0$

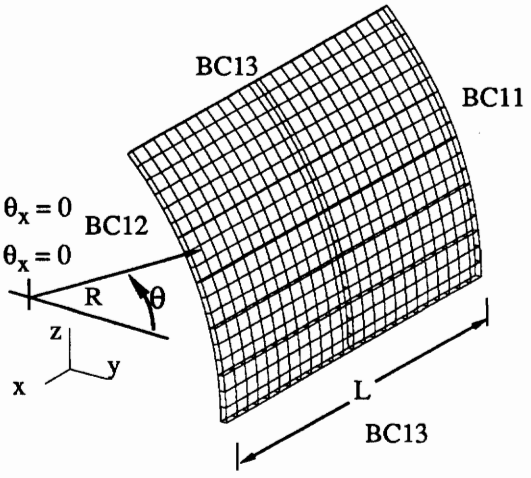

b – 2x8 and 2x24, $N_x = 2700$ lb/in $N_{xy} = 418.5$ lb/in.

Fig. 4.9 – Models of the Conventionally Stiffened Shells Subjected to Axial Compression and Torsion.

categories. In the first category, the value of the angle γ between the stiffeners and the axis of the cylinder (see Fig. 2.1) is large and the stiffeners behave essentially like rings. In this case, the Poisson's expansion of the shell creates tensile stresses in the stiffeners. In the second category, the angle γ is small, and the structural behavior of the stiffened shell resembles more closely the behavior of a shell stiffened by stringers. In this latter category, part of the axial load is carried by the stiffeners. Therefore, compressive stresses developed in these members. Each category of structural behavior is now illustrated by considering a specific example.

The example considers the 4x8 geodesically stiffened configuration (see Fig. 4.10) subjected to axial compression only. The same nominal design used in the previous section for the mesh convergence studies is considered. The skin is 0.08 *in* thick with a quasi-isotropic lamination sequence of $[-45_2/+45_2/90_2/0_2]_S$. The geodesic stiffeners and the rings are made of 0° layers and are 1.5 *in* high and 0.1 *in* and 0.2 *in* thick, respectively. The boundary conditions correspond to those describe in Section 4.2.1 (see Fig. 4.2b). To obtain different angles γ, the overall length of the shell is progressively increased. The u_r component of the static displacement solutions is shown in Fig. 4.11 for three different lengths. In each case, the magnitude of the displacements has been normalized by the value of u_r(R,45°,L/2) of a shell with the same dimensions but stiffened with end rings only.

In Fig. 4.11a, a length of 100 *in* is considered and the resulting behavior of the shell falls in the first category described above. The stiffeners are in tension, and u_r tends to be larger in the unstiffened regions of the skin than in the vicinity of the stiffeners. As the overall length of the shell is progressively increased, a range of angles is found for which the tension due to the Poisson's expansion of the shell is balanced by the compression created by the applied compressive load. As a result, the stiffeners are subjected to a very low level of stress and the radial deflection of the skin is almost uniform over the

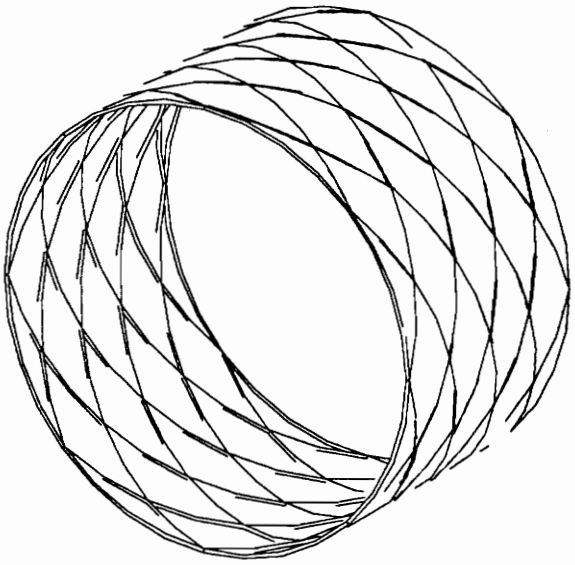

Fig. 4.10 – 4x8 Geodesic Configuration.

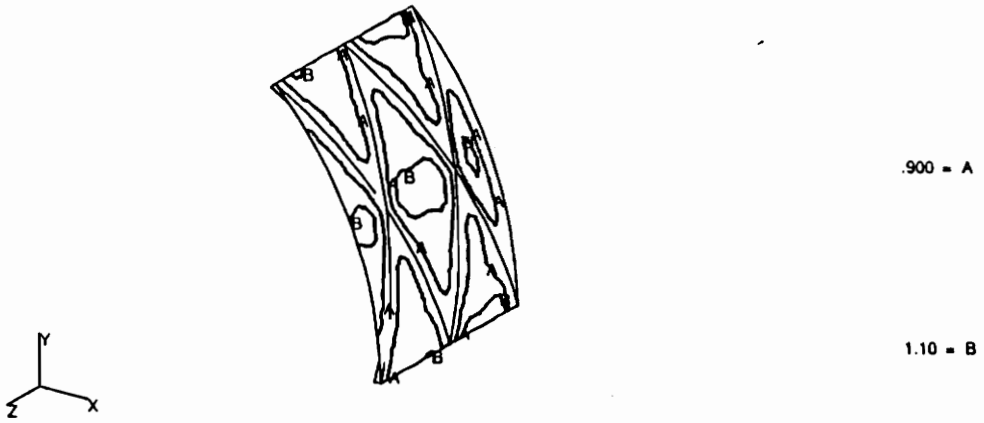

a – L = 100 *in*, $\gamma = 53.2°$.

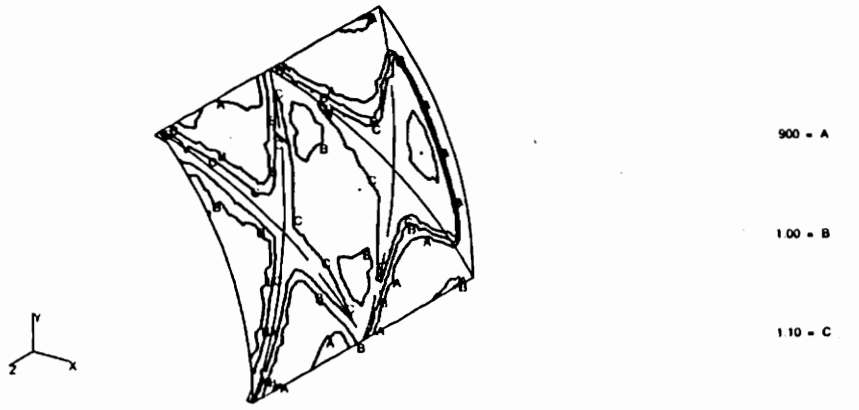

b – L = 175 *in*, $\gamma = 37.3°$.

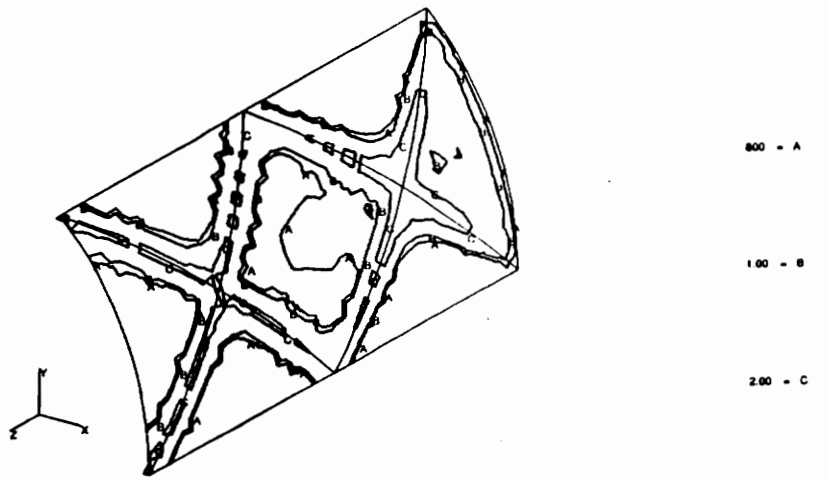

c – L = 300 *in*, $\gamma = 24.0°$.

Fig. 4.11 – u_r Component of the Static Displacement Solution Corresponding to 3 Different Lengths.

entire shell. This type of behavior is illustrated in Fig. 4.11b. In this case, the stiffeners are only slightly compressed. As γ becomes smaller, the compressive stresses in the stiffeners increase and the static displacement pattern is changed substantially compared to the ones obtained for a larger value of γ or for an unstiffened shell. For example, the radial displacements in the vicinity of the stiffener intersections are now more than twice as large as those that would be obtained for an unstiffened shell. On the other hand, in the unstiffened regions, radial displacements smaller than those that would occur in the case of an unstiffened shell are obtained. Past experiences have shown that depending on the stiffness of the stiffeners, negative radial displacements could even occur in the unstiffened regions. These aspects of the behavior of geodesically stiffened shells will also be discussed in Section 5.3, titled Skin Laminate Trends. It will be seen that the ratio of the stiffener to skin stiffnesses also has a strong influence on the magnitude of the radial component of the static displacement solution.

This study clearly demonstrates that depending on the angle γ, the geodesic stiffening pattern can be tailored to resemble either the behavior of a ring or a stringer stiffened shell. In the latter case, however, the curvature of the geodesic stiffeners result in the creation of bending stresses that produce important radial displacement components. This is a disadvantage when aerodynamics considerations require the outer surface of the shell to be as uniform as possible as in the case of aircraft fuselages. Also, such high displacement gradients are likely to produce critical stress states at the skin-stiffener interface where stiffened composite structures are known to be weak. Although under compression the tendency of the stiffeners is to push the skin outward, under tension this tendency would be reversed and the stiffeners would tend to peel-off from the skin.

Finally, when a geodesically stiffened shell is subjected to torsion, half of the stiffeners are in tension and the other half are in compression. Therefore, both categories of behavior are found over different regions of the stiffened shell. As a result, the stiffeners

that are in compression tend to push the skin outward, and those that are in tension tend to pull the skin inward. For example, the u_r component of the static displacement solution obtained for a 2x16 geodesic configuration is shown in Fig. 4.12. The magnitude of the radial displacements correspond to unit tangential displacements applied at each end.

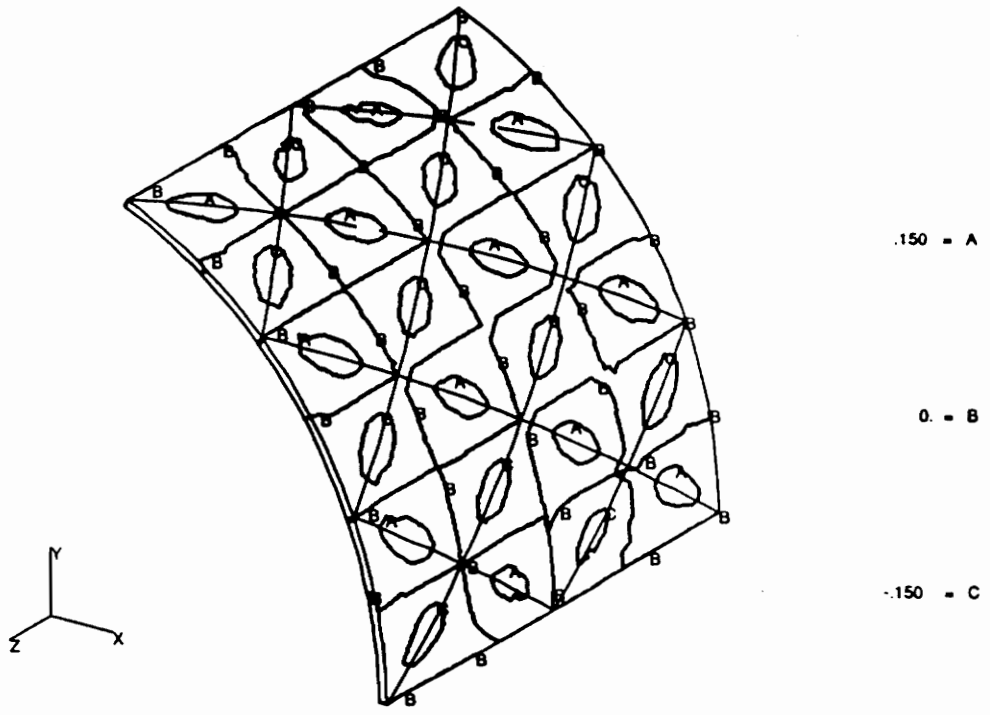

Fig. 4.12 – u_r Component of the Static Displacement Solution under Torsion.

Chapter 5
Design Study Results

In Chapter 3, a new optimization system, called TBOP, has been described and tested on three simple examples. TBOP is based on the finite element package CSM Testbed and the numerical optimization program ADS. In the present chapter, following the outline presented in Section 2.3, it is used to conduct a preliminary design study for minimum-weight aircraft fuselages. In Section 5.1, optimum designs of geodesically stiffened shells subjected to axial compression, torsion, and combined compression and torsion are obtained. In the following section, the results are analyzed and discussed. Trends in design variables and other parameters are examined to determine what contributes to a structurally efficient stiffened shell design. In Section 5.3, trends in the design of the skin laminate of geodesically stiffened shells are discussed. Because of the computational requirements associated with the optimization of the configurations considered in the present study, partial models have been used. The results obtained with these partial models are validated in Section 5.4 where the optimal configurations are analyzed using a larger portion of the structure. Finally, Section 5.5 gives estimates of the computational times required for the calculation of optimal designs for the classes of structures considered in the present study.

5.1 Optimum Designs for Stiffened Shells

In this section, minimum-weight stiffened shell designs subject to constraints on both buckling resistance and material strength are sought. Material strength constraints considered in the analysis are maximum strain failure criterion of the skin and stiffeners. The imposition of material failure constraints is facilitated by the repetitive nature of

the static displacement field from cell to cell. In the case of compressive loading, a material failure constraint is imposed in the skin and a second one in a stiffener. In the case of torsional loading, three material failure constraints are considered. As in the case of compressive loading, a constraint is imposed in the skin. The second and third constraints are imposed in stiffeners subjected to tensile and compressive stresses, respectively. Although a finite element analysis would allow the calculation of material failure constraints close to stress concentrators, the meshes chosen for the design study are not sufficiently refined to allow their accurate evaluation. Consequently, the locations for the evaluation of these constraints (see Fig. 5.1) are such that they are far from the stiffener intersections and edges of the shell where stress concentrations may occur.

To briefly review the scope of the design study, covered in Section 2.3, three cylinder configurations are considered: unstiffened shell, geodesically stiffened cylinder, and conventionally stiffened cylinder. The specific configurations and loading cases are indicated in Table 5.1. For the geodesically stiffened configurations, the number of cells is varied in both the circumferential and axial directions and the minimum-weight design corresponding to each configuration loaded in axial compression and pure torsion is obtained. In combined compression and torsion, only the 2x8 and 2x24 configurations have been studied. For the conventionally stiffened cylinders, a 2x8 configuration has been studied in compression, torsion, and combined compression and torsion. To evaluate the effect of increasing the number of stringers, 2x24 and 2x32 configurations have been studied in compression. The 2x32 configuration has also been studied in pure torsion, and the effect of increasing the number of rings in torsion has been studied with a 4x8 configuration. In compression, the results obtained have shown that the rings play only a minor role. Therefore, the effect of increasing the number of rings has not been studied for this loading case.

Skin laminates with ±45, 90, and 0° plies are considered. Unidirectional material

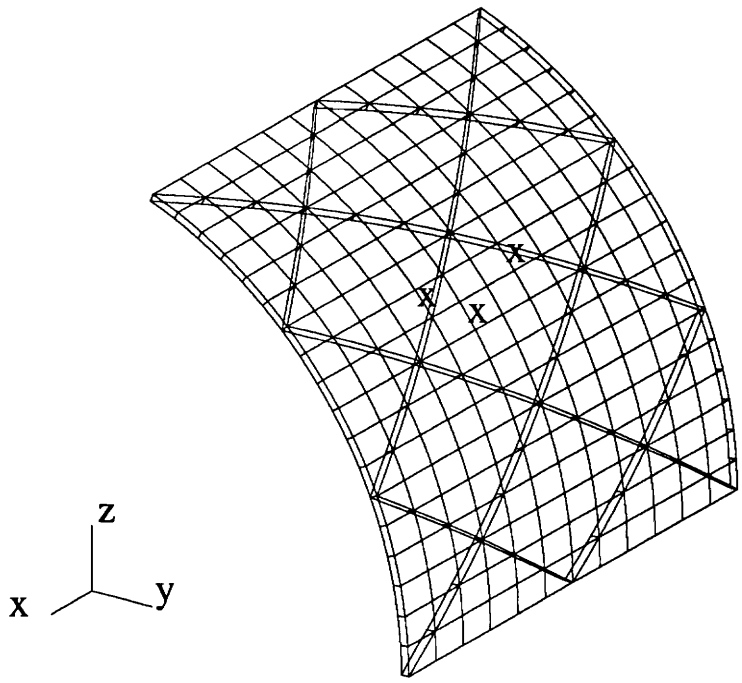

Fig. 5.1 – Locations for the Evaluation of the Material Failure Constraints.

is used in the stiffeners. A minimum-gauge lower bound of 0.005 in is imposed on the thickness of individual plies in the skin. To avoid elements with undesirable aspect ratios, a lower bound of 0.4 in has been imposed on the height of the stiffeners. A minimum-gauge of 0.040 in has been arbitrarily imposed on their thickness. For the unstiffened shell, three design variables are considered. They are the thicknesses of the ±45°, 90°, and 0° plies. For the geodesically stiffened shell, five design variables are used. The first three design variables are identical to those used in the case of the unstiffened shell, and the fourth and fifth design variables designate the thickness and height of the geodesic stiffeners, respectively. For the conventionally stiffened shell, seven design variables are used. As in the case of the geodesically stiffened shell, the first three design variables designate the thickness of the ± 45°, 90°, and 0° plies in the skin. The fourth and fifth design variables designate the thickness and height of the stringers, respectively. The last two design variables designate the thickness and height of the rings that are located away from the ends of the shell. For all the configurations, the final skin layup is: $[-45_{\bar{x}_3}/45_{\bar{x}_3}/90_{\bar{x}_2}/0_{\bar{x}_1}]_S$, where an overbar is placed to indicate that the value of the design variable has been normalized by the thickness of an individual ply. Note that for both the geodesically and conventionally stiffened shells, the end-rings are not considered in the design study. Therefore, their dimensions are constant (0.2 in thick and 1.5 in high) and their weight is not included in the results. The loads applied to the models include the axial compression (N_x), and shear (N_{xy}) which results in torsion. The magnitudes of the loads are 1000 and 2700 lb/in in compression and 418.5 and 1000 lb/in in torsion.

The optimization program ADS allows several choices for each of the three parts (strategy, optimizer, and one-dimensional search) of the solution procedure for the constrained optimization problem. Numerous other parameters also govern the optimization process itself, through specifying internal tolerances, bounds, convergence criteria, etc,

Table 5.1 – Cases Considered in the Design Study.

Configuration	Type	Compression	Torsion	Combined
Unstiffened		x	x	x
1x12	Geodesic	x		
2x4	Geodesic	x	x	
2x8	Geodesic	x	x	x
2x8	Conventional	x	x	x
2x16	Geodesic	x	x	
2x24	Geodesic	x	x	x
2x24	Conventional	x		x
2x32	Geodesic	x	x	
2x32	Conventional	x	x	
2x48	Geodesic	x		
3x24	Geodesic		x	
3x36	Geodesic	x		
4x8	Conventional		x	
4x24	Geodesic		x	
4x48	Geodesic	x		
8x48	Geodesic	x		

for the algorithm. Based on results obtained in Ref. [30], the Sequential Convex Programming strategy, Modified Method of Feasible Directions optimizer, and Bounded Polynomial Interpolation one-dimensional search technique were chosen. For the convergence criterion, a relative change of less than 0.1% in the value of the objective function between two consecutive design iterations is used.

The results obtained in Chapter 4 allowed to determine the level of mesh refinement required for the prediction of the static and buckling responses for each configuration considered herein for compression, torsion and combined compression and torsion. The levels of mesh refinement and the models selected for the design study are summarized in Table 5.2. The loading is introduced using nonzero displacement boundary conditions. Therefore, the scaling procedure implemented in the procedure `analysis` (see Section 3.3.3) is used to scale the displacements to the level of the design load. Only one buckling constraint corresponding to the lowest eigenvalue is imposed on the initial design. In many cases, additional buckling constraints are automatically added by the finite element based optimization system to guarantee convergence of the optimization process (see Section 3.3.4 for a discussion of the strategy used to impose the buckling constraints).

The results of the design runs will now be presented for the different loading cases, in the form of structural efficiency curves for the various geometries. In the present study, "structural efficiency" is defined as minimum cylinder weight for a given load carrying capacity. The comparisons between geodesic and conventional configurations will not include the differences between the cost involved in the construction of each configuration. Detailed results which include the values of each design variable, the constraints, and the objective function are presented in Appendix B.

Table 5.2 – Mesh Refinement Requirements and Models Used in the Design Study.

a – Unstiffened Shell.

Loading	Model	Mesh
		m_{ne} x n_{ne}
Axial Compression	$L/2$ x 90°	12 x 12
Torsion	L x 360°	6 x 36
Combined Compression and Torsion	L x 360°	10 x 40

b – Geodesically Stiffened Shell.

Loading	Configuration	Model	Mesh
			m_{ne} x n_{ne} x l_{ne}
Axial Compression	1 cell in the axial direction	L x 360°/N‡	8 x 8 x 1
	2 cells in the axial direction	L x 360°/N‡	16 x 8 x 1
	3 cells in the axial direction	L x 360°/N‡	24 x 8 x 1
	4 cells in the axial direction	$L/2$ x 360°/N	16 x 8 x 1
	8 cells in the axial direction	$L/2$ x 360°/N	32 x 8 x 1
Torsion	2 cells in the axial direction 4, 8, 16, 24 cells in the circ. direction	L x 3(360°/N)	12 x 18 x 1
	2 cells in the axial direction 32 cells in the circ. direction	L x 9(360°/N)	8 x 36 x 1
	3 and 4 cells in the axial direction 24 cells in the circ. direction	L x 4(360°/N)	12 x 24 x 1
Combined Compression and Torsion	2 cells in the axial direction 8 and 24 cells in the circ. direction	L x 3(360°/N)	12 x 18 x 1

‡N: Number of cells in the circumferential direction

c – Conventionally Stiffened Shell.

Loading	Configuration	Model	Mesh
			m_{ne} x n_{ne} x l_{ne}
Axial Compression	2 cells in the axial direction	L x 360°/N	24 x 8 x 1
Torsion	2 cells in the axial direction 8 cells in the circ. direction	Complete	6 x 48 x 1
	2 cells in the axial direction 32 cells in the circ. direction	L x 3(360°/N)	6 x 24 x 1
	4 cells in the axial direction 8 cells in the circ. direction	L x 4(360°/N)	12 x 48 x 1
Combined Compression and Torsion	2 cells in the axial direction 8 cells in the circ. direction 1000-1000 lb/in	Complete	6 x 48 x 1
	2 cells in the axial direction 8 and 24 cells in the circ. direction 2700-418.5 lb/in	L x 3(360°/N)	24x 18 x 1

5.1.1 Axial Compression Only

Cylinder structural efficiency versus the number of cells, for two levels of axial compression, N_x = 1000 and 2700 lb/in, is shown in Fig. 5.2. The results presented for the conventionally and geodesically stiffened shells in Fig. 5.2a correspond to an increasing number of cells in the circumferential direction for 2 cells in the axial direction. In this figure, filled circles and squares represent the individual designs obtained for the geodesically stiffened configurations, the empty circle and square indicate the results obtained for the unstiffened cylinder, and finally, x's and stars are used to indicate the designs obtained for the conventionally stiffened shells. In Fig. 5.2b, results obtained by considering an increasing number of cells in the axial direction for geodesically stiffened shells with 48 cells in the circumferential direction and subjected to 2700 lb/in of axial compression are presented. For the conventionally stiffened shell, since increasing the number of rings does not significantly affect the designs, this case will not be considered.

As indicated by the results shown in Fig. 5.2a, compared to the unstiffened shells, geodesically stiffened configurations with a small number of cells in the circumferential direction do not provide any weight savings. For the 2x4, 2x8 and 2x16 configurations, the angle γ between the stiffeners and the axis of the shell (see Fig. 2.1) is too large to allow a significant portion of the load to be carried by the stiffeners. However, as the number of cells, and consequently the number of stiffeners, increases there is a clear downward trend for the stiffened shell weight, particularly for the heavier load. Among the studied configurations, the minimum cylinder weight is achieved at both load levels by using 48 cells in the circumferential direction. This geometry weighs 76% and 68% of an unstiffened shell for the 1000 lb/in and 2700 lb/in loads, respectively. The conventionally stiffened configurations are lighter than the corresponding geodesically stiffened cylinders, particularly for the heavier load. For 1000 lb/in, the 8 and 32

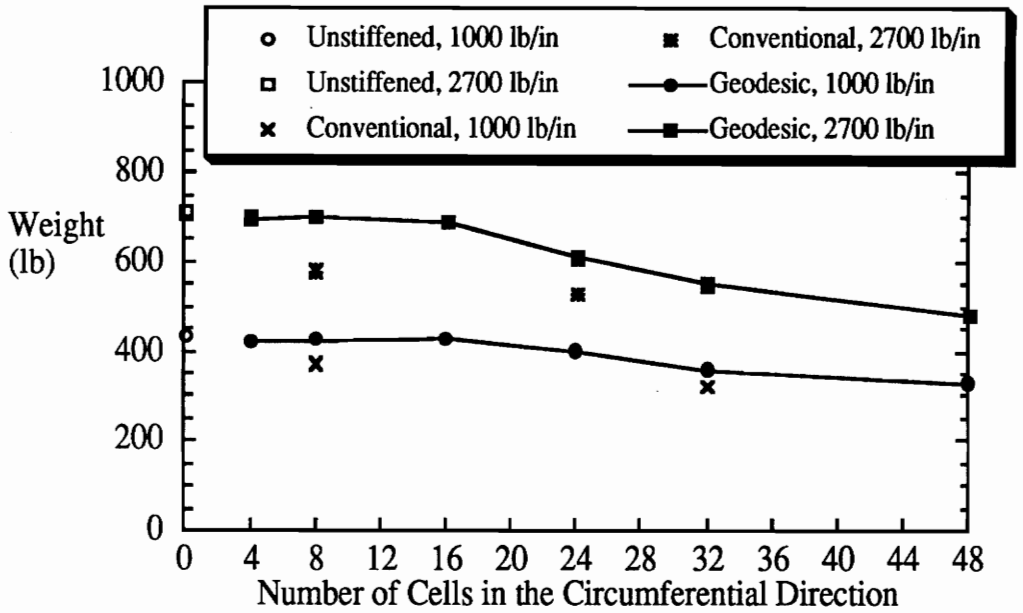

a – Increasing Number of Cells in the Circumferential Direction.

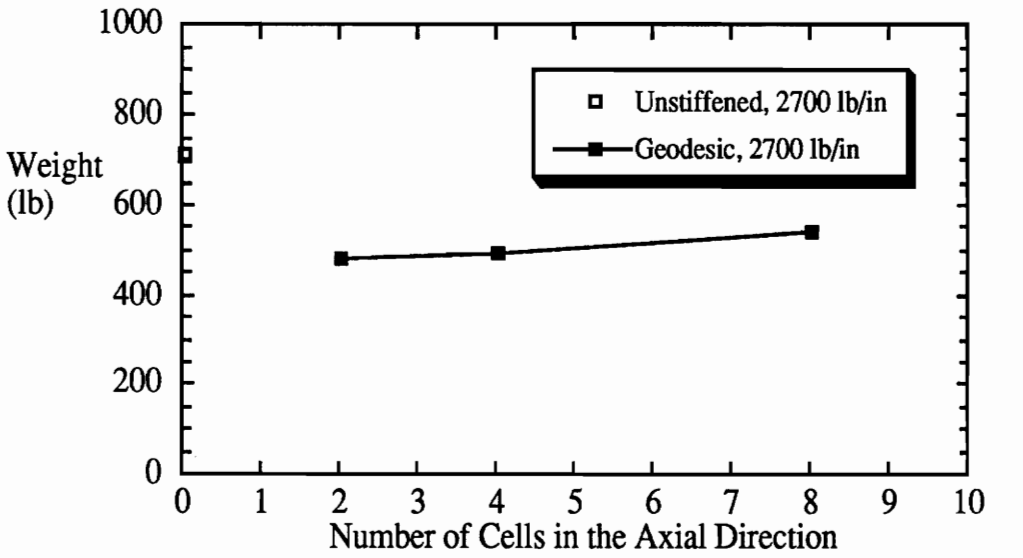

b – Increasing Number of Cells in the Axial Direction.

Fig. 5.2 – Structural Efficiency of Stiffened Cylinders Subjected to Axial Compression.

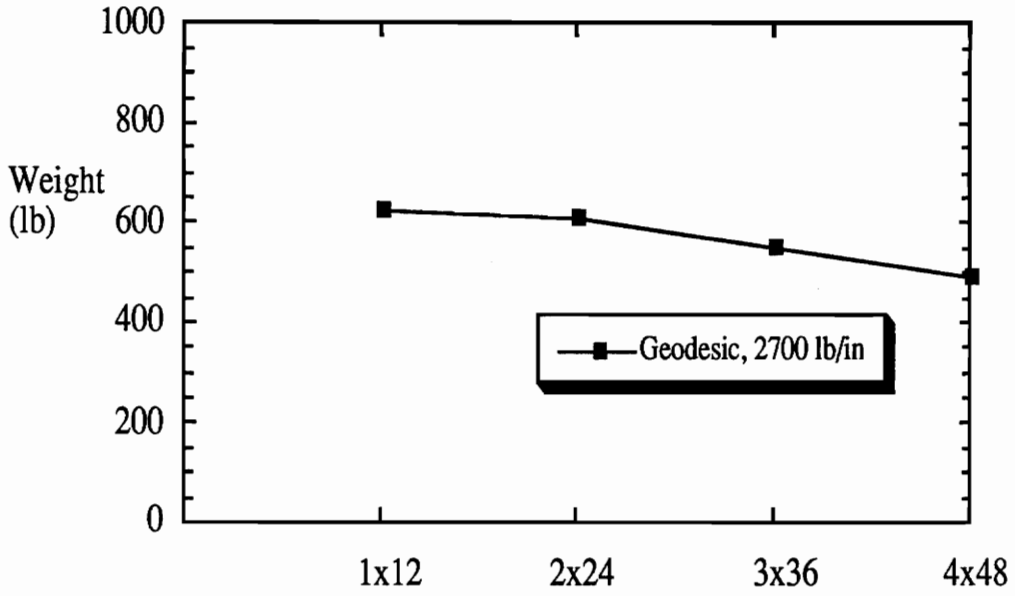

c – Constant Angle Between the Stiffeners and the Shell Axis.

Fig. 5.2 – Structural Efficiency of Stiffened Cylinders Subjected to Axial Compression (Continued).

cell conventionally stiffened configurations weigh 88% and 92% of their corresponding geodesically stiffened configurations, respectively. For 2700 lb/in, the 8 and 24 cell conventionally stiffened shells weigh 83% and 87% of the corresponding geodesically stiffened configuration, respectively.

Considering an increasing number of cells in the axial direction results in heavier designs as indicated by the results shown in Fig. 5.2b which have been obtained for 48 cells in the circumferential direction. This is due to the increase in the value of the angle γ resulting from an increase in the number of cells in the axial direction. The design obtained with 8 cells in the axial direction is 12% heavier than the one obtained with the equivalent two axial cell geometry.

The results presented in Fig. 5.2a and b correspond to an increasing number of cells in the circumferential and axial direction, respectively. As the number of cells in the either of these directions is changed, the angle between the stiffeners and the shell axis is also changed causing a redistribution of the load between the skin and the stiffeners. To isolate the effects of changing the stiffener density without causing a major change into the load distribution between the skin and the stiffeners, trends were also obtained for configurations with a constant angle γ between the stiffeners and the shell axis. The minimum weights obtained for four different configurations that present the same angle $\gamma = 24°$ are shown in Fig. 5.2c for a load level of 2700 lb/in. The results shown in Fig. 5.2c indicate that as the area of unstiffened sections becomes smaller, as a result of increasing the number of cells, the stiffened shell weight decreases. The 4x48 configuration weighs 79% of the 1x12 configuration. In all cases, buckling constraints are the only active constraints at the optimum (see Appendix B).

5.1.2 Torsion Only

A study analogous to that for compressed cylinders is performed for cylinders under

torsion. Because of the coupling that occurs at the laminate level between the bending and twisting responses (D_{16} and D_{26} terms in the constitutive relation [33]), the buckling loads depend on the direction of the applied load. The results presented in this section correspond to a negative torque. However, when both positive and negative eigenvalues were obtained, constraints were imposed on the negative eigenvalues as well as the positive ones to insure that buckling due to a positive torque occurs at a load level of equal or higher magnitude. The minimum weights obtained for each configuration are plotted in Fig. 5.3. The results presented in Fig. 5.3a correspond to an increasing number of cells in the circumferential direction for 2 cells in the axial direction. In this figure, filled diamonds and circles represent the individual designs obtained for the geodesically stiffened configurations, the empty diamond and circle indicate the results obtained for the unstiffened cylinder, and finally "+" and "x" symbols are used to indicate the designs obtained for the conventionally stiffened shell. Two values of N_{xy}, 418.5 lb/in and 1000 lb/in, have been considered. In Fig. 5.3b, a fixed number of cells in the circumferential direction, 24 for the geodesic and 8 for the conventional, and an increasing number of cells in the axial direction is considered. The results in Fig. 5.3b correspond to a single load level, 418.5 lb/in.

Comparison of Figs. 5.2a and 5.3a shows that for equal load magnitudes, the cylinders in torsion are heavier than the axially compressed cylinders. As in the case of axial compression, only buckling constraints are critical at the optimum (see Appendix B). In torsion, the use of even a small number of geodesic stiffeners results in sharp decreases in weight compared to the unstiffened shells. For example, for 418.5 and 1000 lb/in, the 2x8 configuration weighs 77% and 76%, respectively, of equivalent unstiffened cylinders. This is due to the changes that occur in the buckling shapes of the unstiffened and stiffened cylinders. For the unstiffened cylinder, the first buckling mode presents 16 full waves that extend over the entire length of the cylinder. Adding stiffeners precludes

the formation of these long waves and consequently, increases the buckling resistance of the cylinder. Among the geodesic configurations studied, the mimimum weight is still achieved by using the maximum number of cells. The 32 cell geometry weighs 51% and 50% of an unstiffened shell for 418.5 lb/in and 1000 lb/in, respectively. There is little difference between the minimum weights obtained with the conventionally stiffened cylinders and their corresponding geodesically stiffened configurations. For eight cells in the circumferential direction, the conventionally stiffened shell is slightly lighter, but at 32 cells, the opposite is true.

Contrary to the case of axial compression, the consideration of an increasing number of cells in the axial direction results in slightly lighter designs (see Fig. 5.3b). The 4 cell geodesic configuration weighs 94% of the equivalent 2 cell cylinder. The results obtained by considering an increasing number of cells in the axial direction for the 8 cell conventionally stiffened geometry are also shown in Fig. 5.3b. Although a direct comparison of the results obtained from the geodesic and conventional configurations is not possible, it can still be concluded that the addition of cells in the axial direction contributes to more important weight reductions in the case of the conventional configurations that for the geodesic ones. For example, the 4x8 conventionally stiffened cylinder weighs 88% of the 2x8 configuration.

The performance of the geodesically stiffened shell in torsion is rather deceptive. Another preliminary study [6] had suggested that under this loading condition, the geodesic construction would result in lighter designs. As mentioned above, all the designs obtained in this section are buckling critical. Therefore, the incapacity to substantially decrease the weight of the cylinders can be directly related to the lack of increase in buckling resistance. For example, the critical buckling mode obtained for the conventionally stiffened 2x8 configuration, the geodesically stiffened 2x16, 2x24, and 2x32 configurations subjected to N_{xy} of 418.5 lb/in are shown in Fig. 5.4. For the conven-

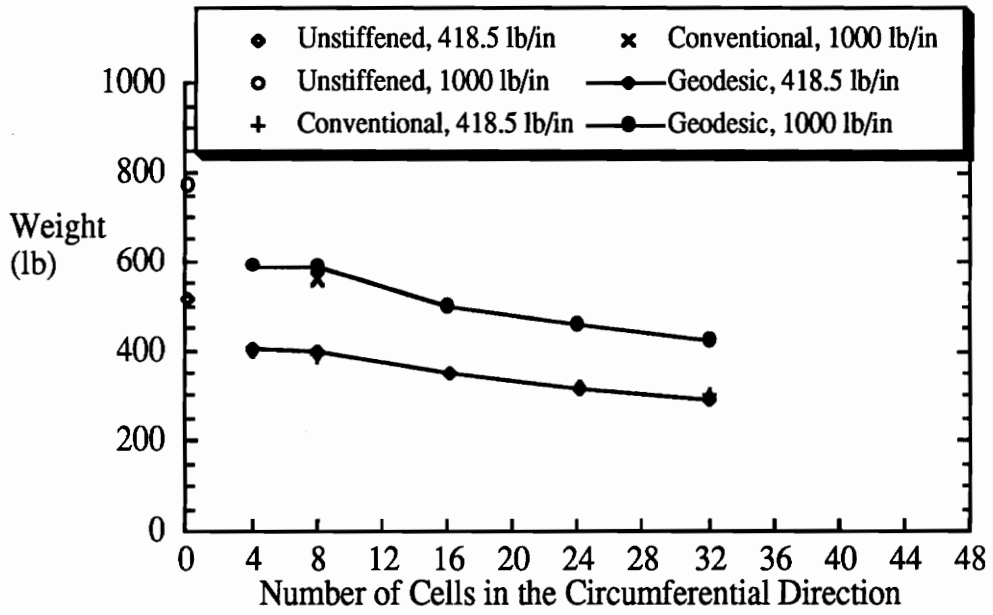

a – Increasing Number of Cells in the Circumferential Direction.

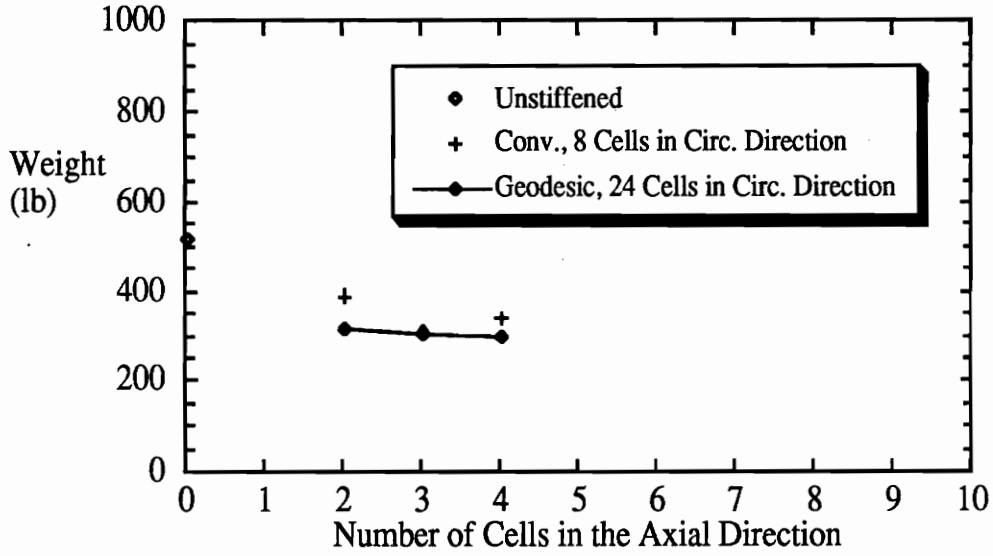

b – Increasing Number of Cells in the Axial Direction.

Fig. 5.3 – Structural Efficiency of Stiffened Cylinders Subjected to Torsion.

tionally stiffened shell, the first buckling mode corresponds to the first buckling mode that would be obtained for an unstiffened shell. However, the axial waves that would develop over the entire length of the cylinder in the case of an unstiffened configuration are broken by the ring. For the 2x16 and 2x24 geodesically stiffened configurations, the first buckling modes are completely different from the one obtained for an unstiffened shell. They present short half-waves well contained within each cell. For that matter, they resemble the first buckling mode of a cylindrical shell stiffened with stringers and subjected to uniform axial compression. For the shell subjected to axial compression only, it has been observed that the best way to improve the buckling resistance was by decreasing the fraction of the applied load carried by the skin. The addition of a small number of stiffeners that do not carry a significant fraction of the load does not result in significant increases in the buckling resistance. It is likely that the same reasoning applies for the type of buckling modes presented by the 2x16 and 2x24 configurations in torsion. As the number of cells in the circumferential direction is increased to 32, however, the first buckling mode switches to long half-waves extending over most of the length of the shell, and consequently, the design should benefit from such a change in the buckling patterns. For that number of cells, however, the angle γ between the stiffeners and the axis of the shell is too small to allow the stiffeners to effectively break the half-waves.

5.1.3 Combined Compression and Torsion

Finally, a combination of axial compression and torsion is considered. For this study, two geodesically stiffened configurations, 2x8 and 2x24, have been arbitrarily chosen and are subjected to two different load cases. First, equal magnitudes of axial compression N_x and torsion N_{xy} of 1000 lb/in are applied. For the second load case, N_x is increased to 2700 lb/in and N_{xy} is reduced to 418.5 lb/in. Minimum-weight designs for

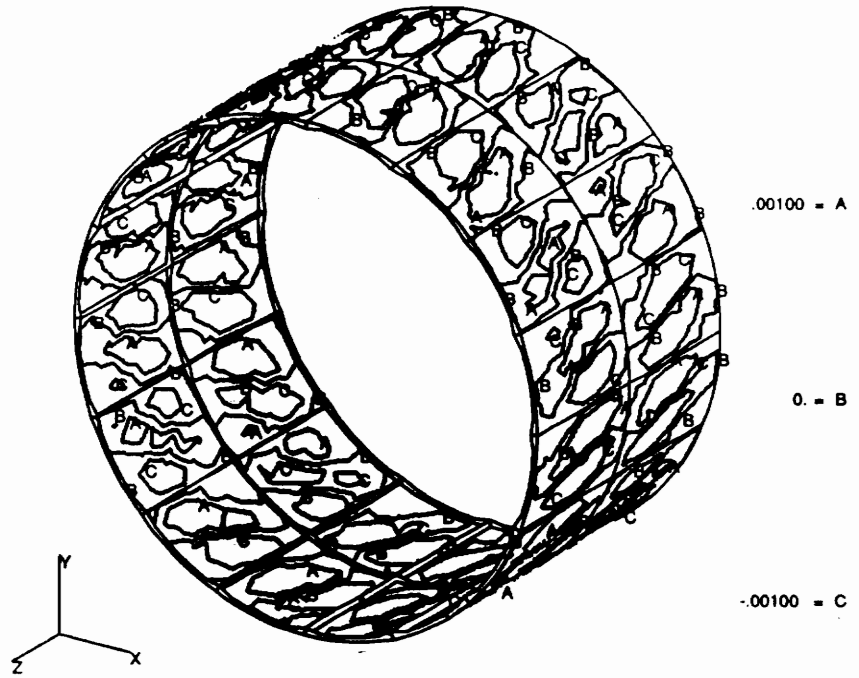

a – 2x8, Conventional Configuration

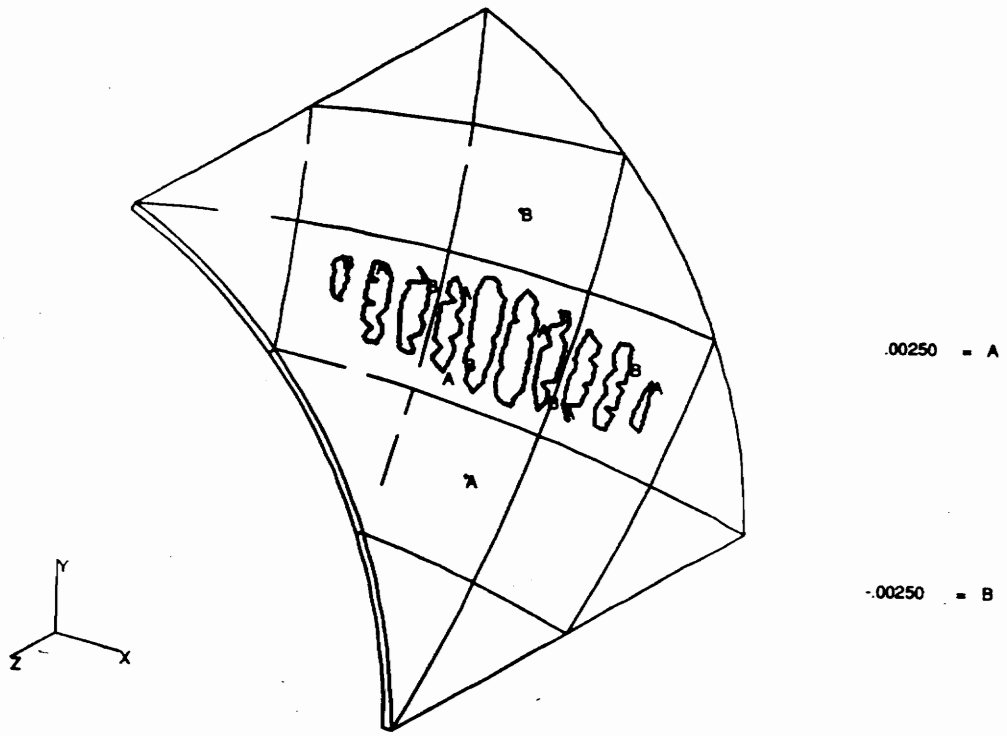

b – 2x16, Geodesic Configuration

Fig. 5.4 – First Buckling Modes, Conventionally and Geodesically Stiffened Configurations.

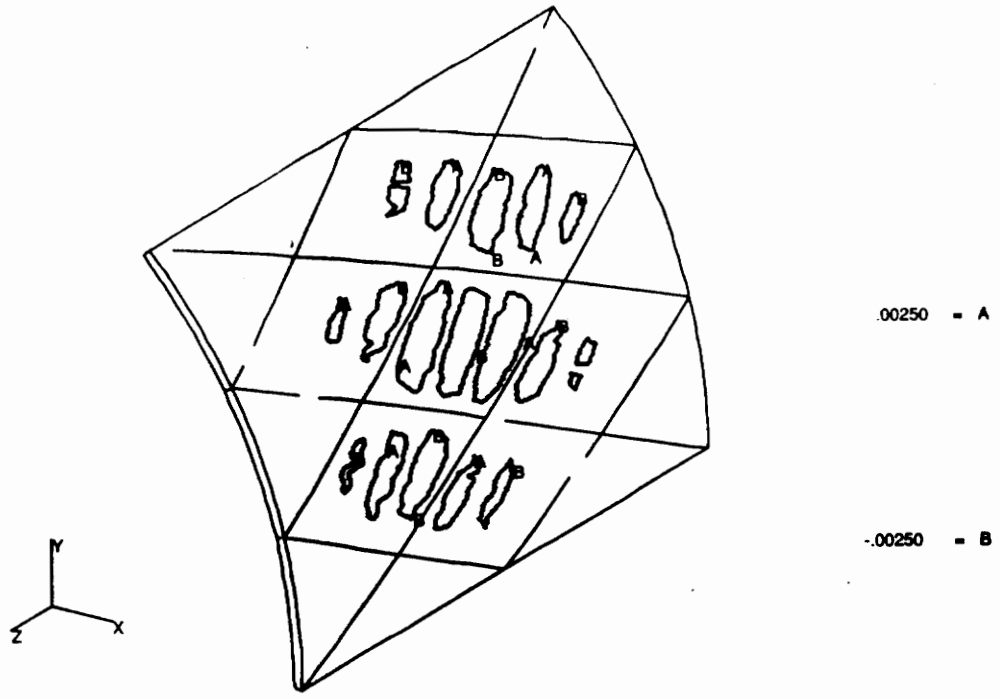

c – 2x24, Geodesic Configuration

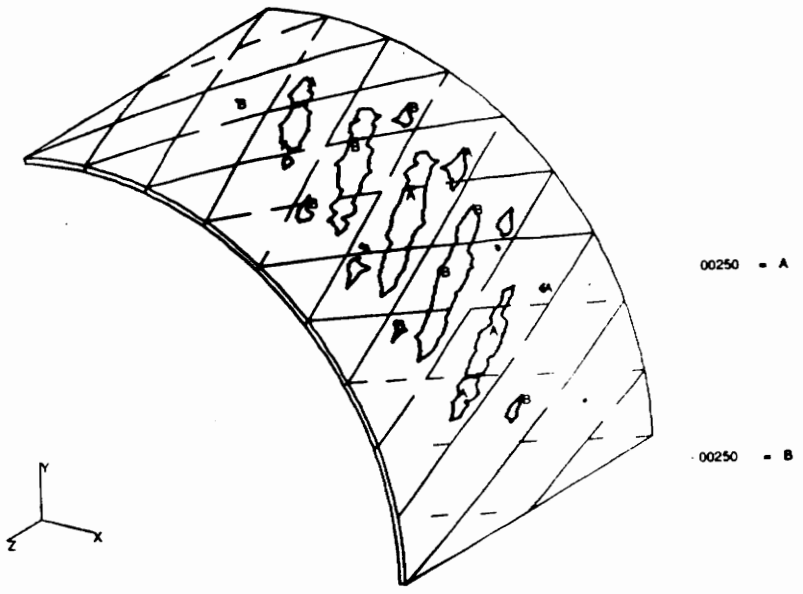

d – 2x32, Geodesic Configuration

Fig. 5.4 – (Continued).

the geodesically stiffened shells, conventionnally stiffened shells, and unstiffened shells are presented in Fig. 5.5. The results obtained for the same configurations subjected to pure axial compression and pure torsion are also shown in the same figure. As in the cases of pure torsion and axial compression only, the lightest geodesic designs are obtained for the configuration that presents the largest number of cells in the circumferential direction. For both load cases, the 2x24 geodesic configuration weighs 78% of the 2x8 geodesic configuration. Compared to the conventionally stiffened configuration, the 2x8 geodesic configuration is only slightly heavier for equal magnitudes of axial compression and torsion. The efficiency of the conventionally stiffened configurations under pure axial compression results in lighter designs compared to their corresponding geodesically stiffened geometries for the 2700-418.5 lb/in load combination. The weights obtained for 1000 lb/in of torsion are larger than those obtained for the same magnitude of pure compression. Also, the ratios of the weight obtained under combined compression and torsion of equal magnitudes to the one obtained under pure torsion are almost equal. For these two reasons, it is concluded that the design of a combined-load cylinder is most sensitive to the torsional load. As in the cases of axial compression and pure torsion, only buckling constraints are active at the optimum.

5.2 Discussion of Design Study Results

In Section 5.1, optimum cylinder designs were presented for an unstiffened shell as well as conventionally and geodesically stiffened cylinders. In that section, only final cylinder weights corresponding to a given load-carrying capacity were compared. Although comparing final weights provides an efficient way of choosing an appropriate cylinder design, a better evaluation of the performance of the geodesic configurations can be achieved by identifying trends in the values of the design variables as well as the distribution of load and weight between the skin and the stiffeners. These considerations

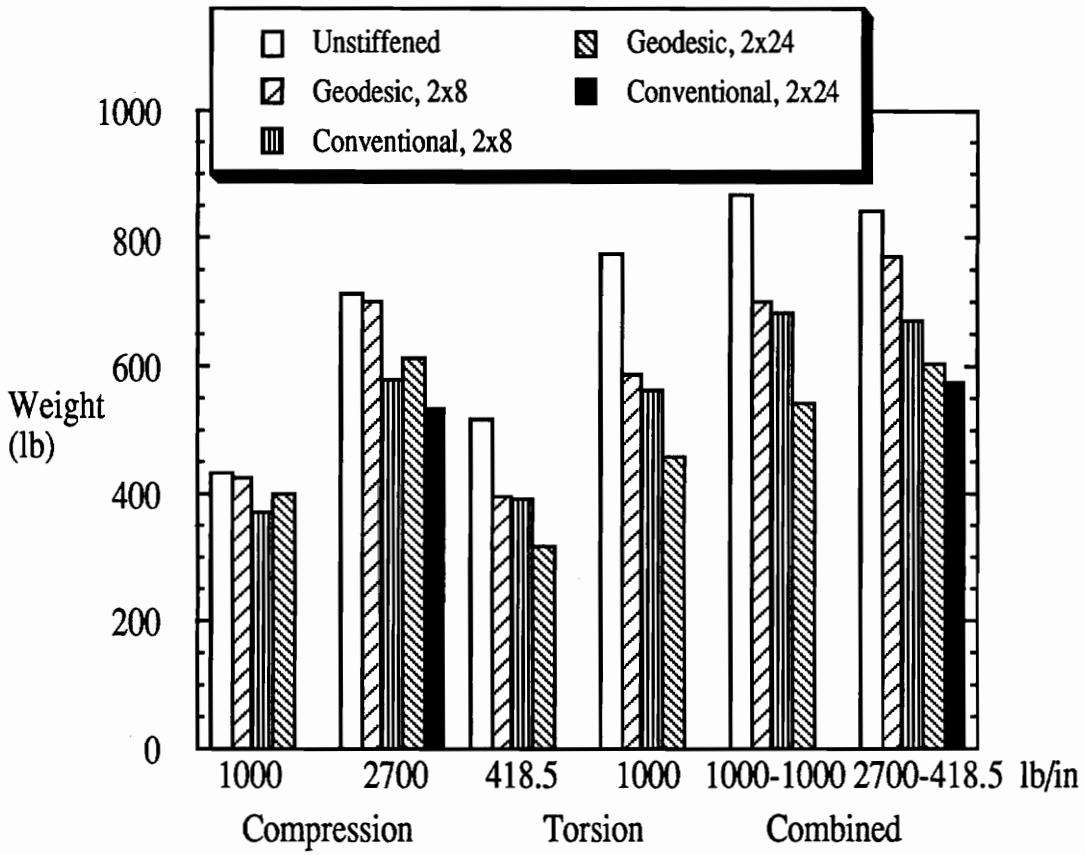

Fig. 5.5 – Results Corresponding to Combined Compression and Torsion.

are discussed in this section.

5.2.1 Convergence Behavior

The history of the optimization run of the 2x24 geodesically stiffened shell configuration (see Fig. 2.2) subjected to an axial stress resultant N_x of 2700 lb/in is used to illustrate the convergence behavior of the design runs. The variation of the structural weight is shown in Fig. 5.6. Between 20 and 30 design iterations were typically required to reduce the difference in weight between two consecutive iterations to less than 0.1%. This level of convergence, however, was not sufficiently stringent to guarantee that the values of the individual design variables are well converged. The trends that will be discussed in this section are consequently based on non-optimal values of the design variables and could be modified if optimal values were considered. In general, the skin thickness design variables have a higher degree of convergence than the stiffener dimensions. This is due to the fact that for the configurations with a small number of cells, the stiffener cross-section dimensions will have only a small influence on the weight. Moreover, in the case of axial compression, the addition of a small number of geodesic stiffeners does not result in a significant increase in the value of the buckling load. Therefore, under compression and for a design with a small number of stiffeners, the optimizer will tend to reduce the weight and satisfy the constraints by adjusting the thickness of the skin ply thicknesses, leaving the stiffener cross-section dimensions practically unchanged. The resulting skin thicknesses for these cases are almost identical to those obtained for the unstiffened shells. As the number of cells is increased for a compressive loading, the stiffeners tend to comprise a larger fraction of the final weight, resulting in better convergence for the stiffener dimensions. However for the torsional loading case, regardless of the number of cells, the stiffeners still make up less than 20% of the final weight and consequently, the stiffener dimensions are not as well

converged. In many cases, several initial designs have been considered and the lightest of the resulting designs has been retained.

The difficulty in obtaining convergence is illustrated in Fig. 5.7. This figure presents the results obtained for the optimal design of geodesically stiffened configurations subjected to 418.5 lb/in of torsion. In Fig. 5.7a, the change in weight corresponding to an increasing number of cells in the circumferential direction is shown. In parts b and c of the same figure, variations in skin thickness and stiffener cross-sectional area are plotted, respectively. For each of these parameters, the results obtained by starting from two different initial designs are shown for 4, 8, and 16 cells. The results are denoted Series A and Series B. Although starting from different initial designs results in little difference in the weights and overall skin thicknesses, significant differences in stiffener cross-sectional areas are obtained.

For the 2x8 and 2x16 configurations, only one buckling constraint is critical for the final design. Consequently, the optimality of these designs can be evaluated by using the optimality criterion for a single constraint [29]:

$$\frac{\partial f}{\partial x_i} - \lambda \frac{\partial g_{b1}}{\partial x_i} = 0, \quad i = 1, \ldots, n, \tag{5.1}$$

which can be rewritten

$$\lambda = \frac{\partial f}{\partial x_i} / \frac{\partial g_{b1}}{\partial x_i}, \quad i = 1, \ldots, n. \tag{5.2}$$

Equation (5.2) is a measure of the cost effectiveness of the ith design variable in affecting the constraint. At the optimum, all the design variables that are not at their lower or upper bounds should be equally cost effective in changing the constraint. The values of λ have been calculated for several final designs and are listed in Table 5.3. Note that the values of λ should be as closely spaced as possible and that the normalization procedure precludes comparisons between columns. It is seen that for the 2x32 geodesically stiffened shell and the 2x8 conventionally stiffened shell, the values of λ are relatively

closely spaced, indicating the proximity of an optimum. Also, in each column, the values of λ associated with the skin design variables are generally more closely spaced. For the 2x8 and 2x16 geodesic configurations, however, the values of λ are widely distributed, and consequently, none of the designs presented in either column Series A or Series B correspond to optimum designs. Thus, the differences between the designs shown in Fig. 5.7 for the 2x4, 2x8, and 2x16 configurations cannot be attributed to the occurence of local minima but rather to the small influence of the stiffener cross-section dimensions on the weight.

To estimate the number of design iterations that would be required to converge the values of the design variables, the optimal design of the 2x8 geodesic configuration subjected to 418.5 lb/in has been considered. First, to obtain a better estimate of the optimal stiffener dimensions, the design variables corresponding to the skin ply thicknesses were fixed, and only two design variables, corresponding to the stiffener thickness and height, have been considered. After 22 design iterations, the design variables corresponding to the skin ply thicknesses were re-introduced and 21 additional design iterations were performed. The new design, denoted Design C, is presented in columns 6 and 7 of Table 5.4 along with the designs corresponding to Series A and Series B for the 2x8 configuration. Although the values of the cost effectiveness parameters λ associated with Design C indicate that this design is not optimum, their range has become significantly smaller as a result of the additional design iterations. These also indicate that the additional design iterations had a small effect on the value of the objective function as the weight corresponding to Design C represents 99% of the one corresponding to the 2x8 configuration obtained for Series A. These further indicate that in the design of stiffened composite cylindrical shells, one has a great deal of flexibility in the choice of the values for design variables since several combinations of these can be found with only minor changes in the final weight.

Table 5.3 – Values of $\lambda = \frac{\partial f}{\partial x_i} / \frac{\partial g_{b1}}{\partial x_i}$.

Design Variable	2x32 Geod. Compression 2700 *lb/in*	2x8 Geod. Torsion 418.5 *lb/in*		2x16 Geod. Torsion 418.5 *lb/in*		2x8 Conv. Compression 1000 *lb/in*
		Series A	Series B	Series A	Series B	
x_1	l.b.†	100	72.0	67.9	90.0	l.b.
x_2	88.0	44.4	99.2	70.4	86.7	93.0
x_3	87.1	46.3	95.6	l.b.	100	100
x_4	91.3	63.7	72.4	100	94.0	95.3
x_5	100	100	41.1	72.3	76.0	95.8
x_6						l.b.
x_7						l.b.

† Indicates that this design variable is at its lower bound.

Table 5.4 – Comparison of Three Designs Obtained for the 2x8 Geodesic Configuration Subjected to 418.5 lb/in of Torsion

	Series A		Series B		Design C	
	Value *in*	λ	Value *in*	λ	Value *in*	λ
t_0 (in)	0.0197	100	0.0182	67.9	0.0175	100
t_{90} (in)	0.0293	99.2	0.0273	70.4	0.0291	100
$t_{\pm 45}$ (in)	0.00730	95.6	l.b.	N/A	0.00793	98.6
t_g (in)	0.0838	72.4	0.180	100	0.0622	90.9
h_g (in)	0.881	41.1	2.37	72.3	1.44	81.8
Weight (lb)	398.4		401.4		393.7	

† Indicates that this design variable is at its lower bound.

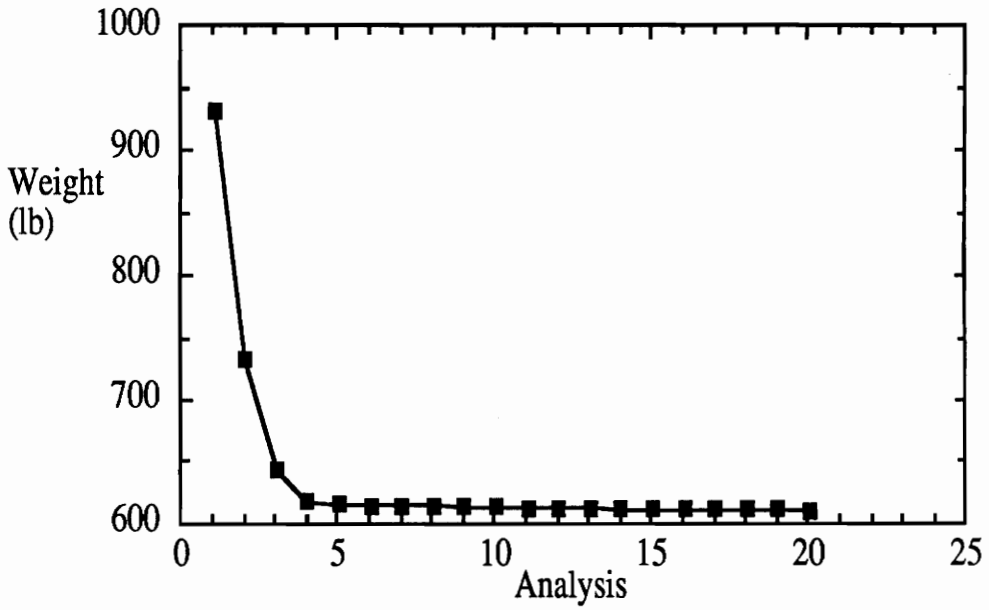

Fig. 5.6 – Convergence History, 2x24 Shell Configuration.

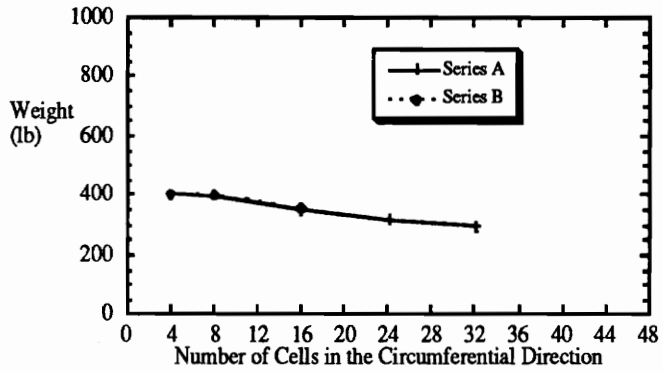

a – Weight Reduction.

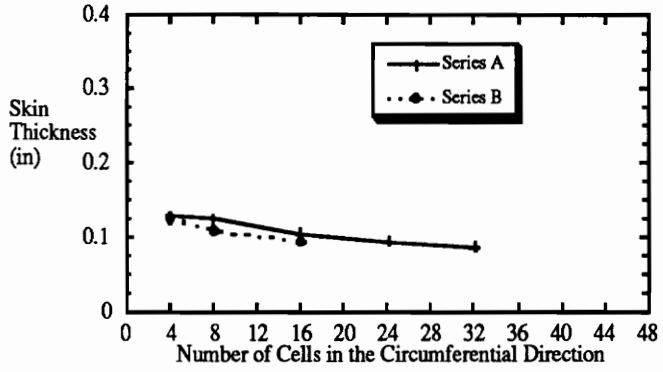

b – Variation of the Skin Thickness.

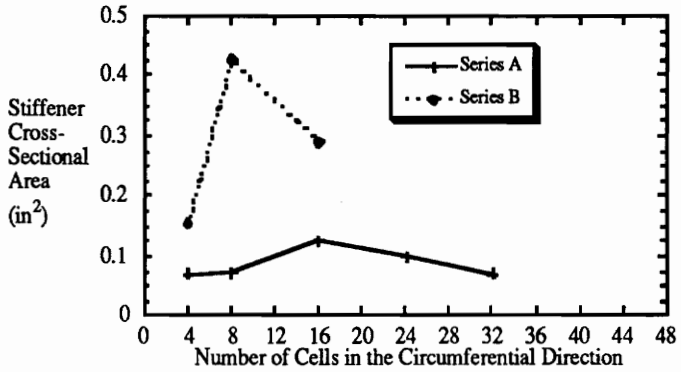

c – Variation of the Stiffener Cross-Sectional Area.

Fig. 5.7 – Optimum Designs Obtained by Starting from Different Initial Designs.

To investigate the cause for slow convergence in the values of the design variables, the conservative approximation used for the buckling constraint by the Sequential Convex Programming strategy has been replaced by a first-order Taylor series approximation. The results obtained from the two design runs which utilized the linear approximation demonstrate that, for the same move limits, more rapid convergence toward optimal values for the design variables is obtained. In Fig. 5.8, the variation in the ratio of the maximum value of the cost-effectiveness parameter to its minimum value is shown, calculated for 10 design cycles and with each type of approximation for the 2x8 geodesic configuration subjected to 418.5 lb/in of torsion. At the optimum, the values of λ should be equal and consequently the ratio of $\lambda_{max}/\lambda_{min}$ should be 1. As indicated by this plot, the linear approximation results in more rapid convergence in the values of the design variables than the conservative approximation although the difference in the structural weights obtained from each approximation after 10 design cycles is less than 0.2%.

For nearly all cases of unstiffened and geodesically stiffened shells which were considered, several buckling constraints were imposed on the design. Recal that the procedure used in the present study to impose buckling constraints is based on the examination of the derivatives of a selected range of eigenvalues with respect to the design variables (see Section 3.3.4). To briefly review the strategy, the derivatives of all the computed eigenvalues in a 20% range above the lowest one are examined. Then, a new buckling constraint is set up for every eigenvalue with a derivative with respect to any one of the design variables more than 20% different from the derivatives of those eigenvalues that are already constrained. The number of computed eigenvalues is an input parameter for the eigensolver which has been set to 8 in the present study. For all the configurations studied, the first buckling mode corresponds to a skin buckling mode. As indicated by the results presented in Appendix B, several buckling constraints are usually automatically set up by the procedure. In several cases, two or even three

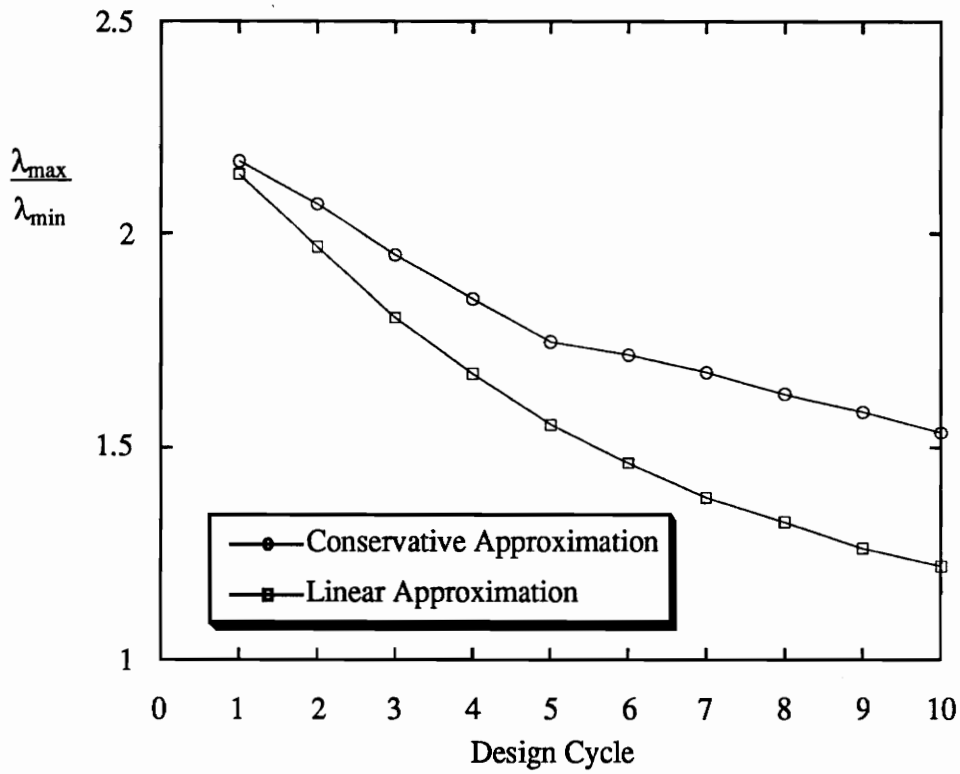

Fig. 5.8 – Convergence behavior Using two Different Approximations for the Buckling Constraint.

buckling constraints are critical at the optimum. In these cases, the value of $\overline{v}_k$ in Eq. (3.3) is incremented according to the rule

$$\overline{v}_1 = 1.0 \tag{5.3}$$

$$\overline{v}_k = \overline{v}_{k-1} + \frac{0.005}{(k-1)}, \qquad k = 2, \ldots, 8$$

although arbitrary, the rule given by Eq. (5.3) guarantees that a finite distance will remain between successive groups of eigenvalues. On the other hand, the difference between $\overline{v}_{k-1}$ and $\overline{v}_k$ is not large enough to significantly affect the final design. In torsion, as the optimization progresses, negative eigenvalues (which correspond to buckling due to a positive torque) are found and a buckling constraint usually corresponds to one of those. As a result, the final designs in torsion are buckling resistant for both negative and positive torques.

Finally, the results of the mesh convergence study presented in Table 4.2 indicate that the 16x8x1 mesh used in the design of the geodesically stiffened shell loaded in axial compression can predict the lowest eigenvalue within 9.5% of the one obtained with the most refined mesh. To evaluate the impact of this relatively poor accuracy on the results obtained in the design study, new designs have been obtained for the 2x24 and 2x48 configurations subjected to axial compression. These designs are based on a 24x12x1 mesh which allows to predict the lowest eigenvalue within 1.3% of the one obtained with the most refined mesh. The minimum weights obtained are given in Table 5.5. It is seen that the use of a more refined mesh results in weight increases varying between 1% and 4%. Based on these results, it has not been considered necessary to redesign the other configurations with the more refined mesh. Consequently, the discussion of the trends in the design of geodesically stiffened shells will be based on the results obtained with the 16x8x1 mesh.

Table 5.5 – Final Weights Obtained with Two Mesh Refinements.

Configuration		Mesh		Weight Increase %
		16x8x1	24x12x1	
2x24	1000	400.0	404.1	1
	2700	611.6	618.1	1
2x48	1000	328.9	337.2	3
	2700	484.4	502.8	4

5.2.2 Skin Thickness Trends

The trends in the total (not ply) thickness for the skin of the configurations considered in the present study are plotted in Figs. 5.9 and 5.10. The same nomenclature and symbols used in Sections 5.1.1 and 5.1.2 are used. Since the weight depends strongly on the value of the total skin thickness, similar trends are obtained. They will consequently not be repeated here, and only trends in the values of individual design variables will be discussed.

In compression, among the three design variables used to tailor the skin thickness, only the one that designates the thickness of the 0° plies reaches its lowed bound. This occurs for the geodesically stiffened configurations that have 16, 24, 32, and 48 cells in the circumferential direction at both load levels, as well as for the conventionally stiffened cylinders. This indicates that as the angle between the stiffeners and the direction of the load becomes smaller, the design benefits from a more compliant skin which allows a larger portion of the applied load to be carried by the stiffeners. For an increasing number of cells in the axial direction, the increase in skin thickness between 2 and 8 cells in the axial direction is mostly caused by an increase in the thickness of the 90° plies. The 0°, and 45° ply thicknesses remain almost unchanged. As was the case for the other configurations, the design variable representing the thickness of the 0° plies remains at its lower bound. When the angle between the stiffeners and the shell axis is kept constant, the design variable associated with the thickness of the 0° plies also remains at its lower bound.

In the case of pure torsion, the design variable corresponding to the ±45° plies is the only one that tends to its lower bound. This occurs, at 418.5 lb/in, for the 2x24, 3x24, and 4x24 cell configurations and at 1000 lb/in for the configurations that present 16 or more cells in the circumferential direction. By remaining at its lower bound, the design

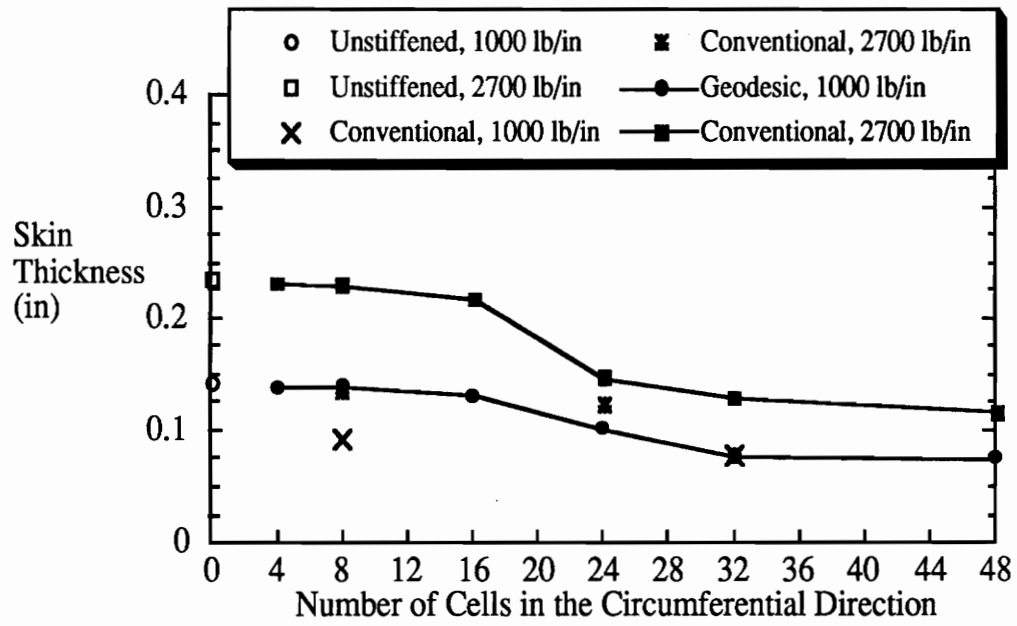

a – Increasing Number of Cells in the Circumferential Direction.

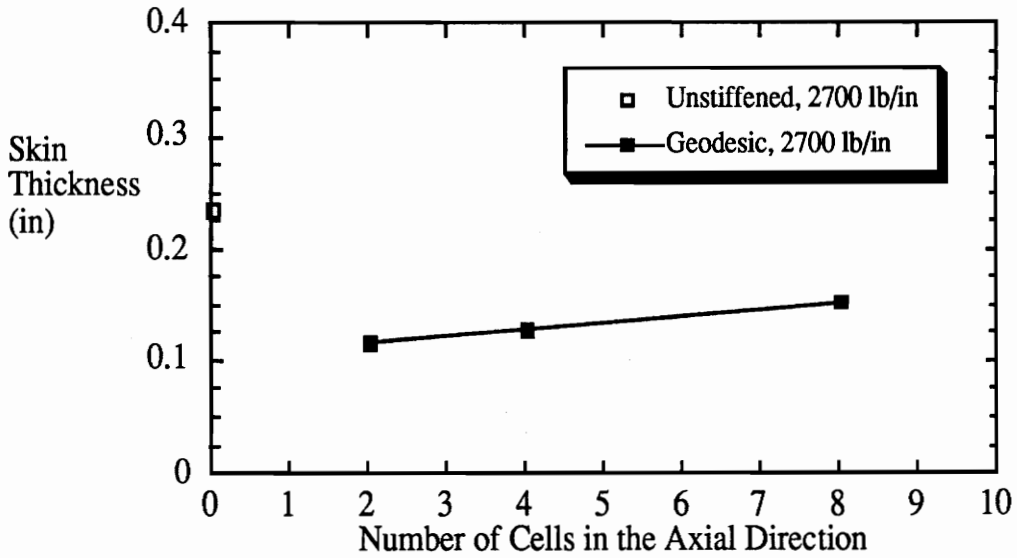

b – Increasing Number of Cells in the Axial Direction.

Fig. 5.9 – Skin Thickness Trends, Axial Compression.

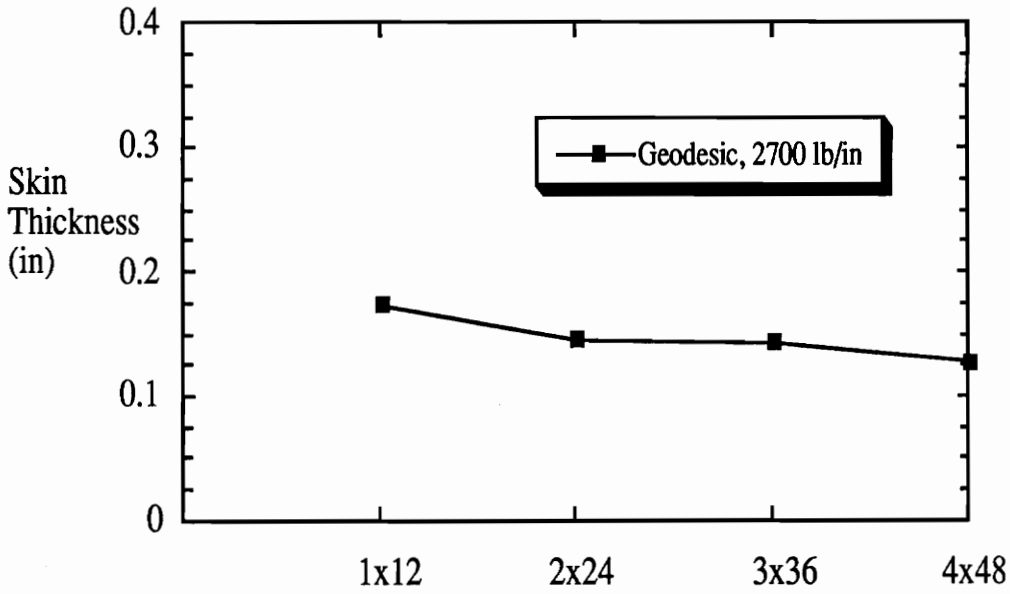

c – Constant Angle Between the Stiffeners and the Shell Axis.

Fig. 5.9 – Skin Thickness Trends, Axial Compression (Continued).

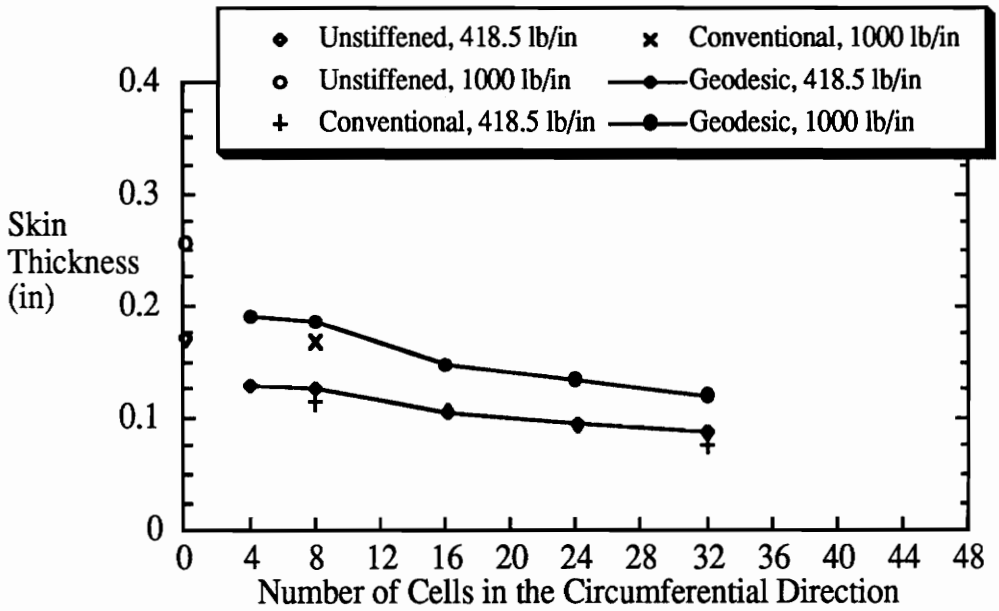

a – Increasing Number of Cells in the Circumferential Direction.

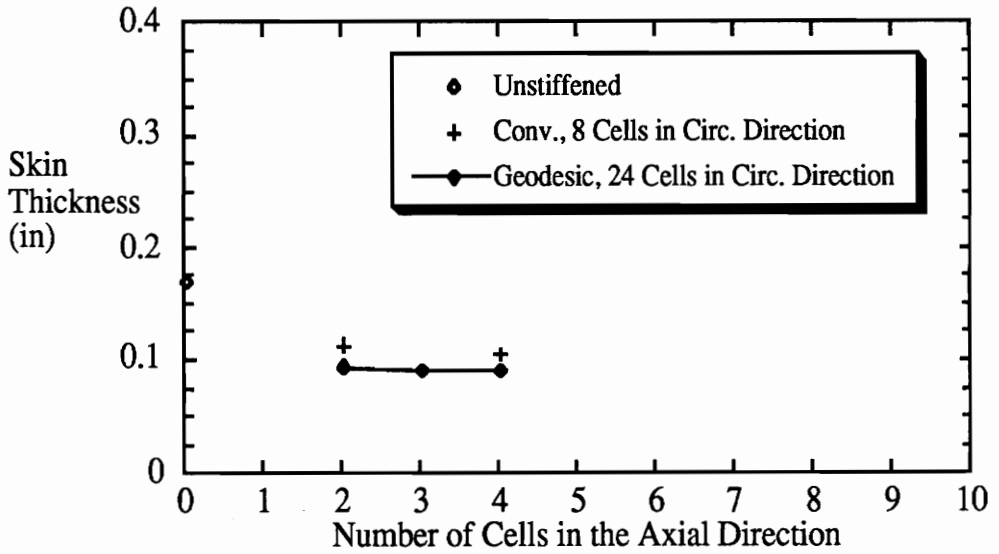

b – Increasing Number of Cells in the Axial Direction.

Fig. 5.10 – Skin Thickness Trends, Torsion.

variable that designates the thickness of the ±45° plies allows more load to be carried by the stiffeners. This is the equivalent of the behavior of the 0° plies in the case of axial compression. More will be said about this aspect of the design study in Section 5.3, titled Skin Laminate Trends.

5.2.3 Stiffener Dimensions, Load and Weight Fractions

The trends in stiffener cross-sectional areas, load and weight fractions are discussed in this section. The stiffener load fraction is defined as the portion of the total applied load carried by the stiffeners; the remainder of the load is carried by the skin. The fraction of the total cylinder weight made up by the stiffeners is called the stiffener weight fraction.

5.2.3.1 Axial Compression

The trends in stiffener cross-sectional areas, load and weight fractions are shown in Figs. 5.11, 5.12, and 5.13. In each of these figures, part a displays the trends obtained by considering an increasing number of cells in the circumferential direction. The trends obtained in the case of an increasing number of cells in the axial direction are shown in part b, and the trends obtained for a constant stiffener angle γ are shown in part c.

Increasing Number of Cells in the Circumferential Direction. For both load levels, all three parameters remain small for 4 and 8 cells in the circumferential direction. This is due to the large angle γ between the stiffeners and the axis of the cylinder which reduces their efficiency to carry the axial load. For 4 cells in the circumferential direction, this angle is so large that the stiffeners are loaded in tension due to the Poission's expansion of the shell. As the angle γ becomes smaller, as a result of an increase in the number of cells in the circumferential direction, the portion of the load carried by the stiffeners, the fraction of the total weight that they represent, as well as their cross-sectional area increase. The stiffener cross-sectional area reaches its maximum for 24 cells. As the

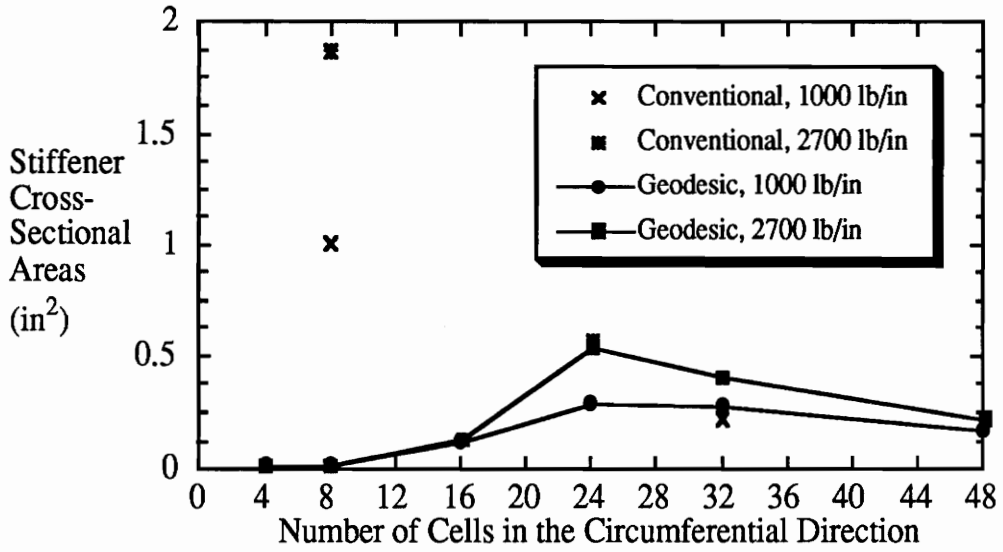

a – Increasing Number of Cells in the Circumferential Direction.

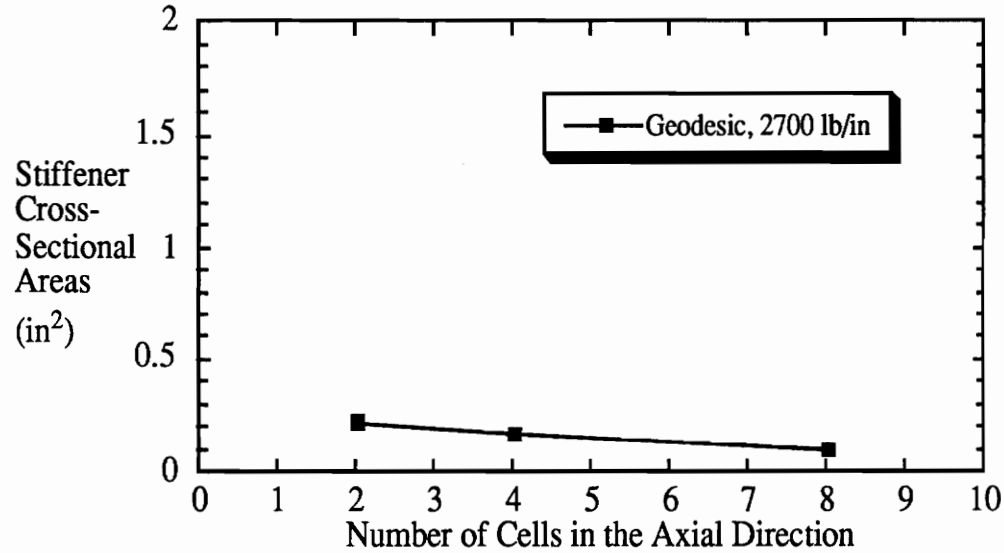

b – Increasing Number of Cells in the Axial Direction.

Fig. 5.11 – Stiffener Cross-Sectional Areas of Stiffened Cylinders Subjected to Axial Compression.

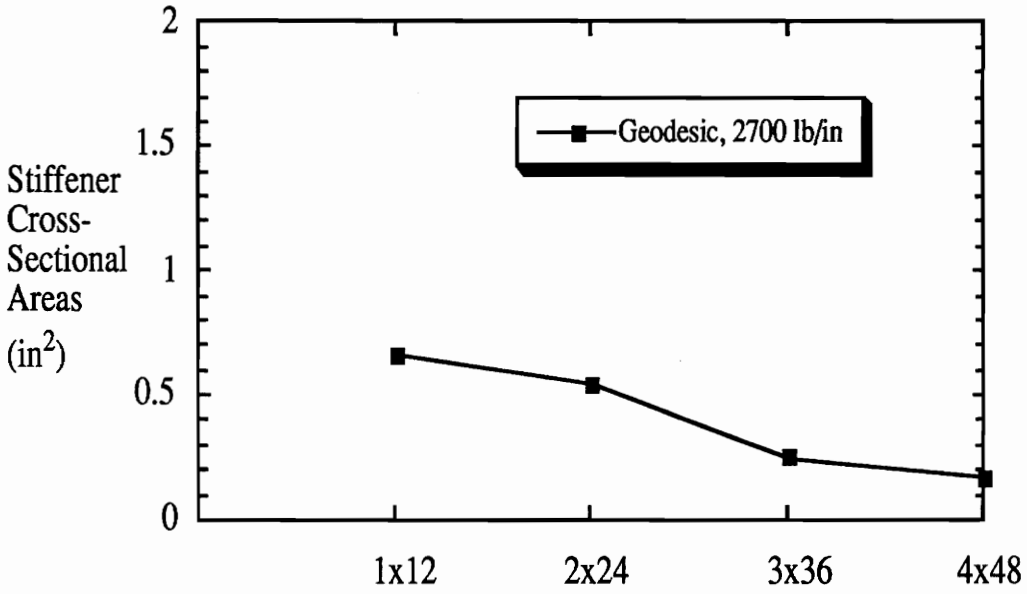

c – Constant Angle Between the Stiffeners and the Shell Axis.

Fig. 5.11 – Stiffener Cross-Sectional Areas of Stiffened Cylinders Subjected to Axial Compression (Continued).

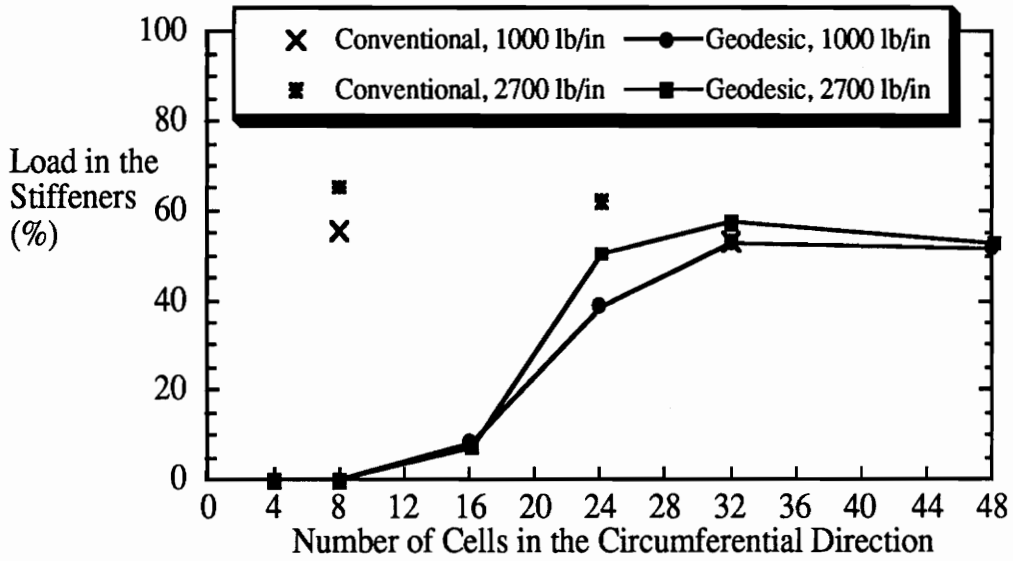

a – Increasing Number of Cells in the Circumferential Direction.

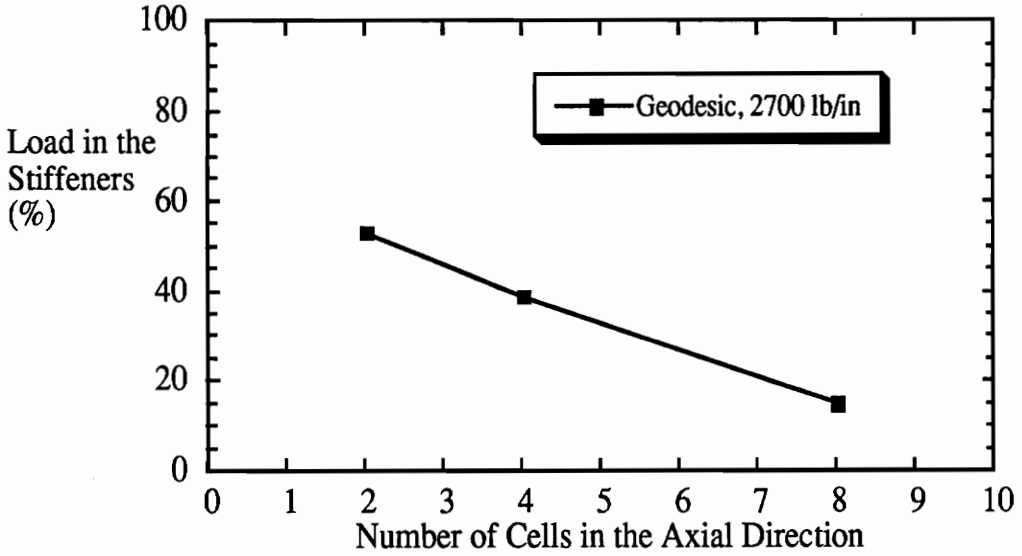

b – Increasing Number of Cells in the Axial Direction.

Fig. 5.12 – Load Carried by the Stiffeners, Axial Compression.

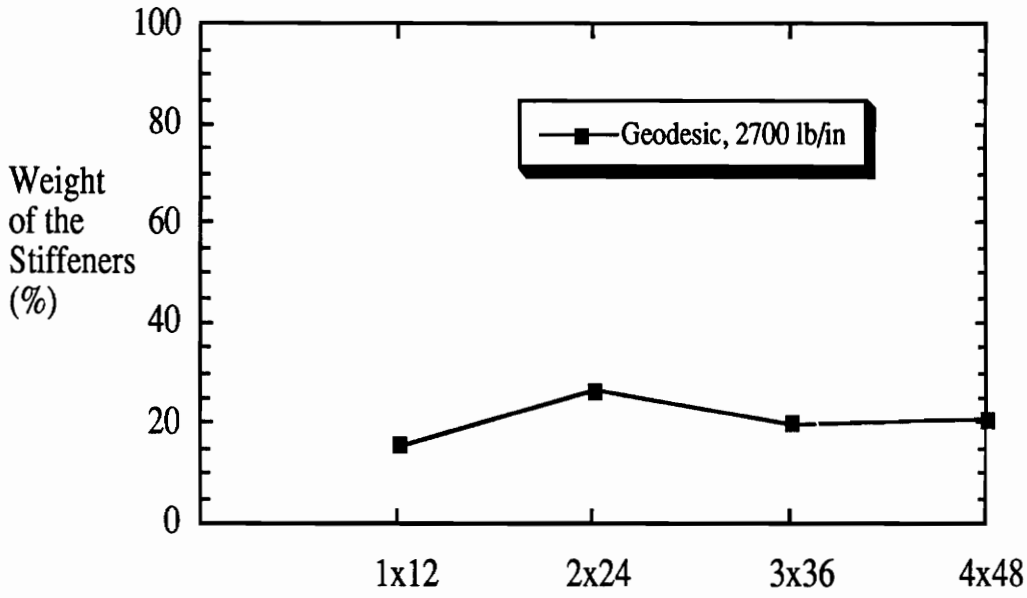

c – Constant Angle Between the Stiffeners and the Shell Axis.

Fig. 5.12 – Load Carried by the Stiffeners, Axial Compression (Continued).

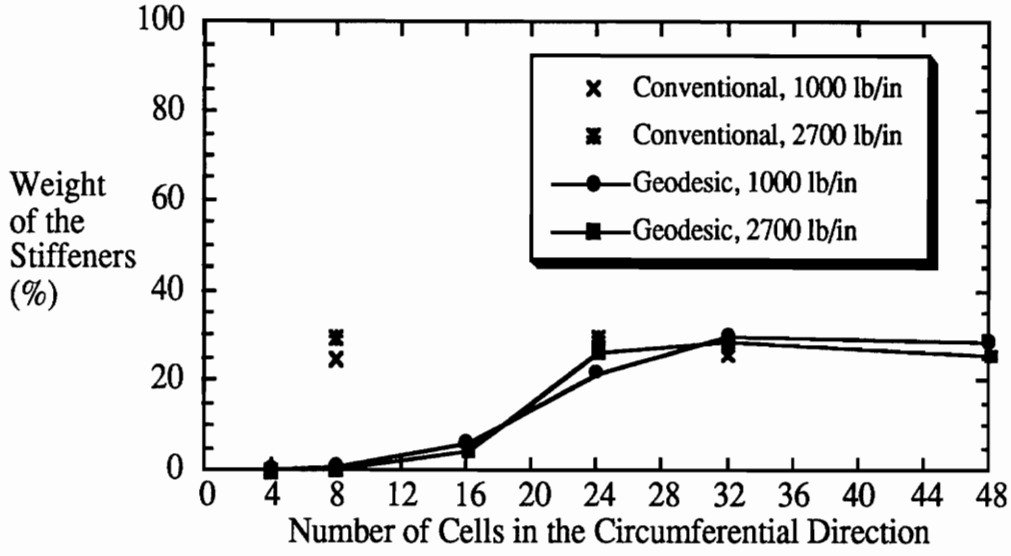

a – Increasing Number of Cells in the Circumferential Direction.

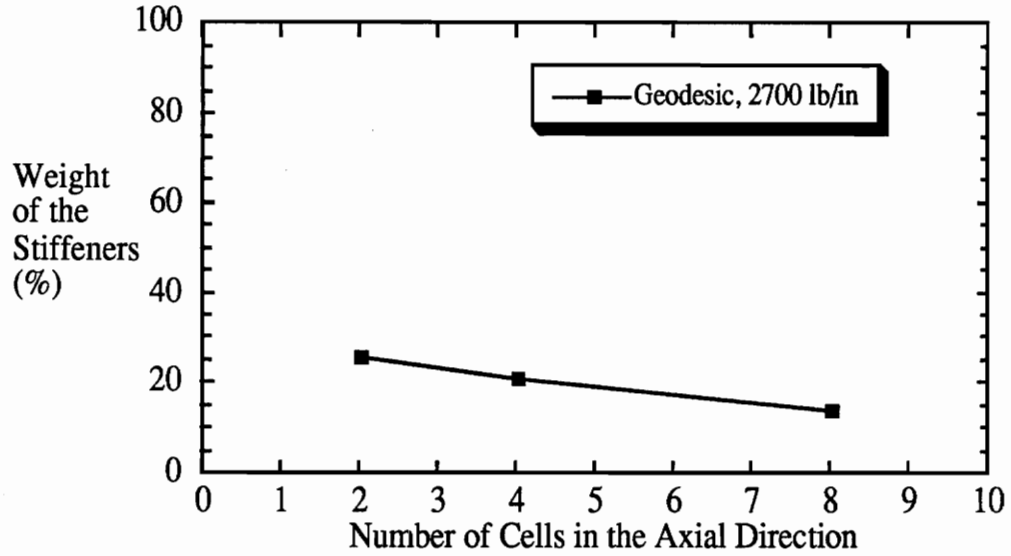

b – Increasing Number of Cells in the Axial Direction.

Fig. 5.13 – Stiffener Weight Fraction, Axial Compression.

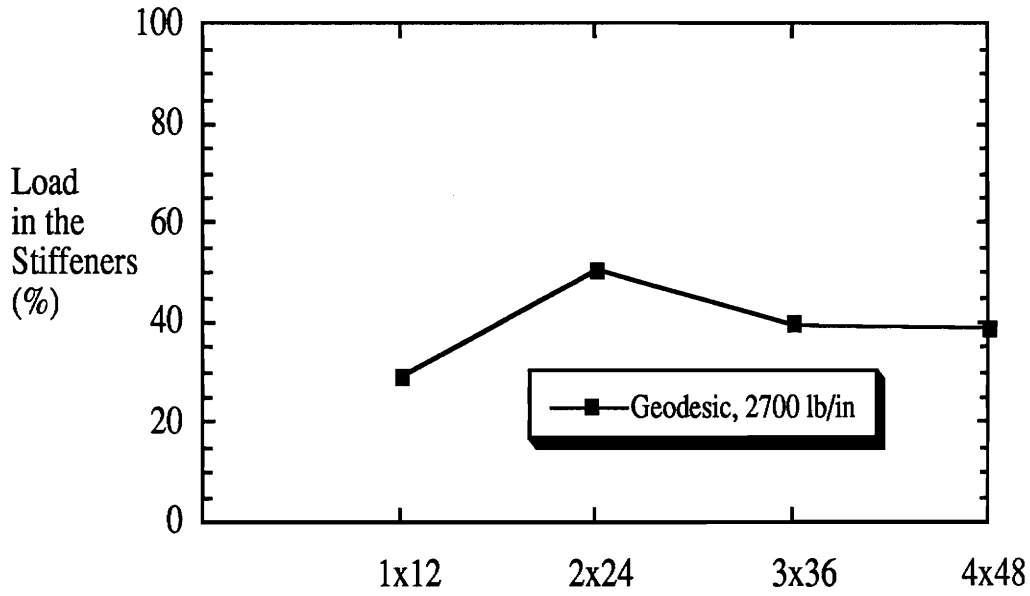

c – Constant Angle Between the Stiffeners and the Shell Axis.

Fig. 5.13 – Stiffener Weight Fraction, Axial Compression (Continued).

number of cells and stiffeners keep increasing, their cross-sectional area becomes smaller since the stiffeners do not have to be as rigid to carry their share of the axial load and stabilize the skin. On the other hand, the stiffener load and weight fractions reach their maximum for 32 cells and decrease slightly for 48 cells. For the 32 cell configuration, the stiffeners carry 58% and 53% of the applied load for 2700 lb/in and 1000 lb/in, respectively, and their weight represents approximately 30% of the total weight of the shell.

Comparing the cross-sectional areas and load fractions carried by the stringers of the conventionally stiffened cylinders to those of the geodesically stiffened shell stiffeners allows to measure the efficiency of the geodesic stiffeners to carry the axial load. For eight cells, the cross-sectional area and the load fraction of the conventionnally stiffened shell stiffeners are substantially larger than the ones of the geodesically stiffened shells. On the other hand, for 32 cells, both stiffening patterns are almost equally efficient as the stiffener cross-sectional areas and the fraction of the load that they carry are only slightly different.

The same trends noted for the cross-sectional areas of the geodesically stiffened shells can be observed for the individual dimensions (thickness and height) of the stiffeners. For 4 and 8 cells in the circumferential direction, both dimensions remain very close to their lower bounds. As the number of cells is increased, both dimensions follow an upward trend until they reach their maximum for 24 cells and then decrease smoothly for 32 and 48 cells. The only exception is for the stiffener thickness at 1000 lb/in for which the maximum occurs for the 2x32 configuration rather than the 2x24.

Increasing Number of Cells in the Axial Direction. As the number of cells in the axial direction is increased, the stiffener cross-sectional areas, weight and load fractions follow a downward trend, see Figs. 5.11b, 5.12b, and 5.13b. This is due to the increasing angle between the axis of the cylinder and the stiffeners which make these members less

efficient in carrying the axial load. For eight cells in the axial direction, the stiffeners carry 15% of the applied load and represent only 14% of the total weight, when compared to 53% and 26%, respectively, for the equivalent 2 cell configuration.

Constant angle between the stiffeners and the shell axis. When the angle between the stiffeners and the shell axis is kept constant ($\gamma = 24°$), the stiffeners are in compression and consequently, the behavior of the stiffened shell falls in the second category described in Section 4.3. For these configurations, the stiffener cross-sectional areas decrease as the number of cells is increased. The stiffener cross-sectional area of the 4x48 configuration represents only 26% of the one obtained for the 1x12 geometry. On the other hand, the percentage of the load that they carry as well as the fraction of the total weight that they represent reach their maximum for the 2x24 configuration and remain almost constant for the 3x36 and 4x48 configurations. This implies that as the density of the stiffeners increases, each stiffener does not need to be as stif to carry its share of the axial load and stabilize the skin. Comparing the results obtained for the 3x36 and 4x48 configurations allows to conclude that although for both configurations the same fraction of the load is carried by the stiffeners, reducing the area of the inter-stiffener skin sections results in a thinner skin and smaller cross-stiffener areas which in turn allow to achieve weight savings. For example, the 4x48 configuration weighs 89% of the 3x36 one.

5.2.3.2 Torsion

In the case of pure torsion, the trends in stiffener cross-sectional areas, load and weight fractions are shown in Figs. 5.14, 5.15, and 5.16. Part a of these figures displays the trends obtained by considering an increasing number of cells in the circumferential direction whereas the trends obtained in the case of an increasing number of cells in the axial direction are shown in part b.

Increasing Number of Cells in the Circumferential Direction. For an increasing number of

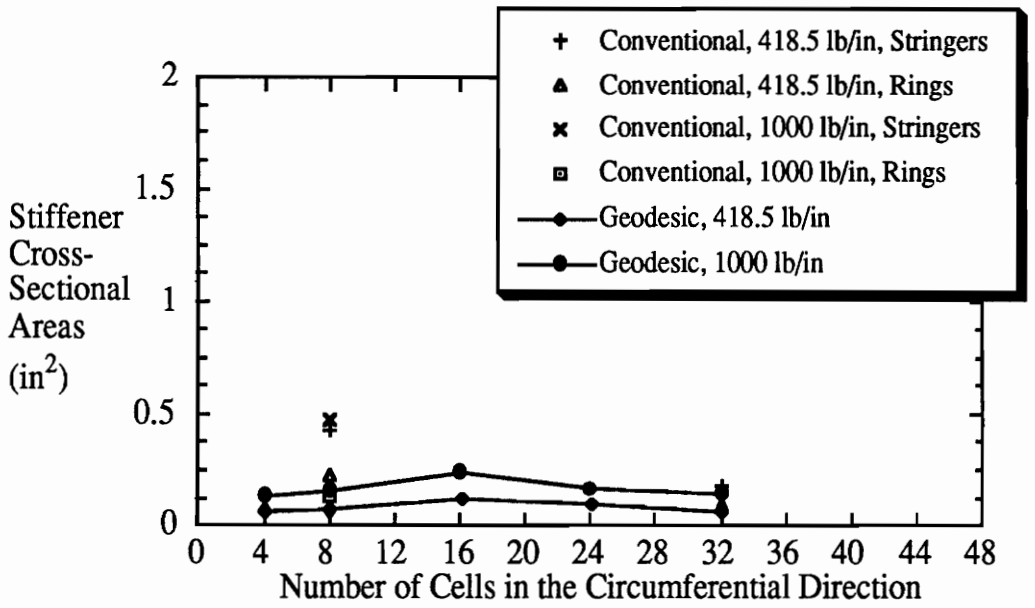

a – Increasing Number of Cells in the Circumferential Direction.

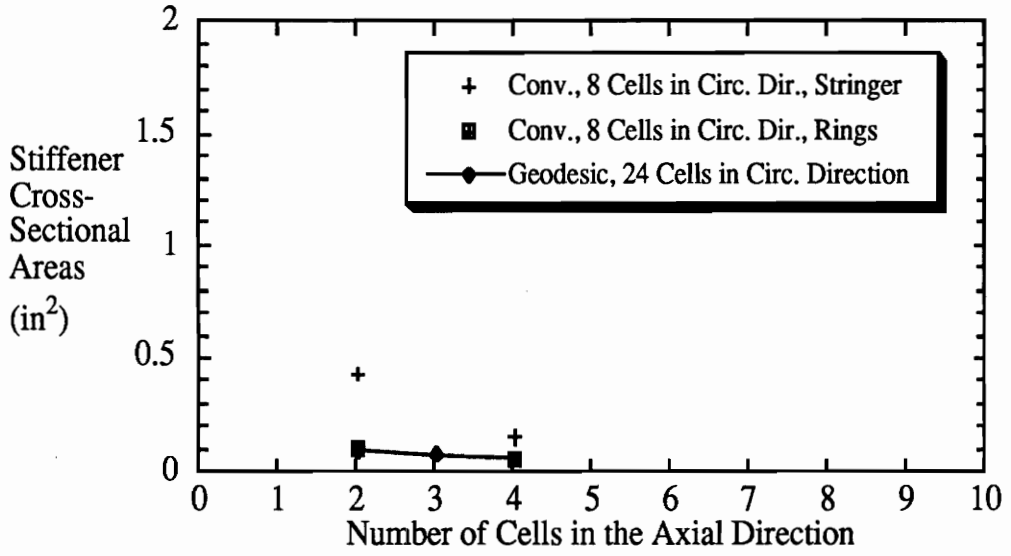

b – Increasing Number of Cells in the Axial Direction.

Fig. 5.14 – Stiffener Cross-Sectional Areas of Stiffened Cylinders Subjected to Torsion.

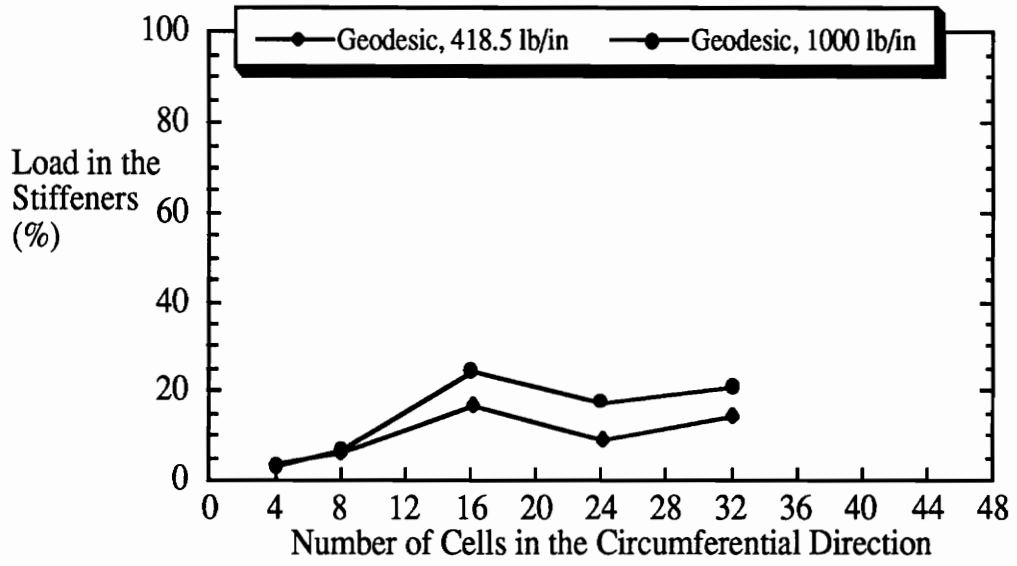

a – Increasing Number of Cells in the Circumferential Direction.

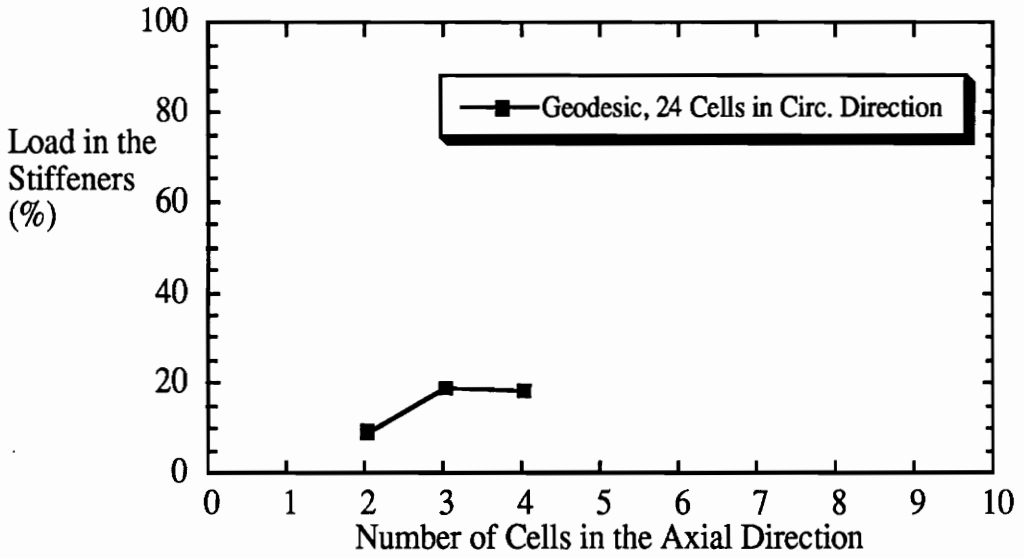

b – Increasing Number of Cells in the Axial Direction.

Fig. 5.15 – Load Carried by the Stiffeners, Torsion.

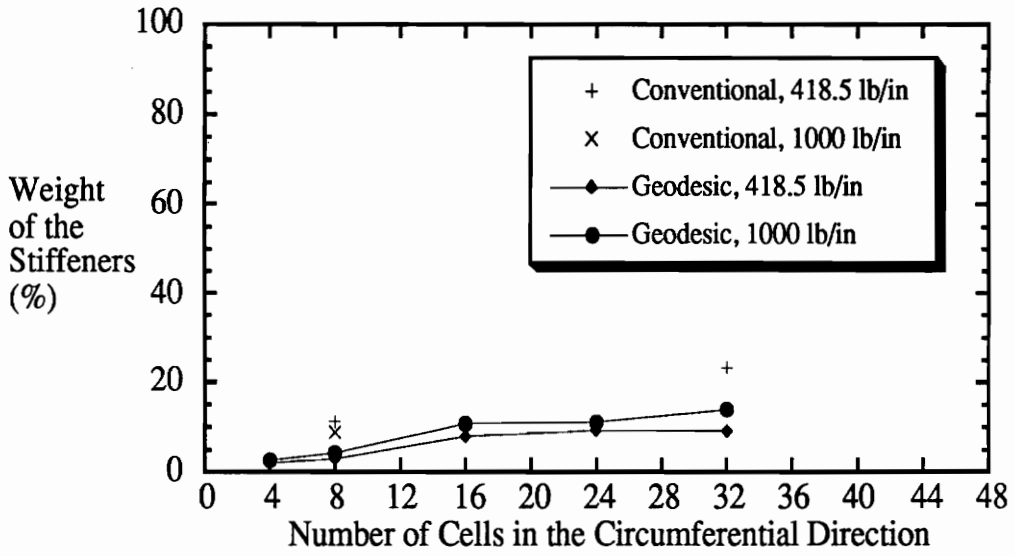

a – Increasing Number of Cells in the Circumferential Direction.

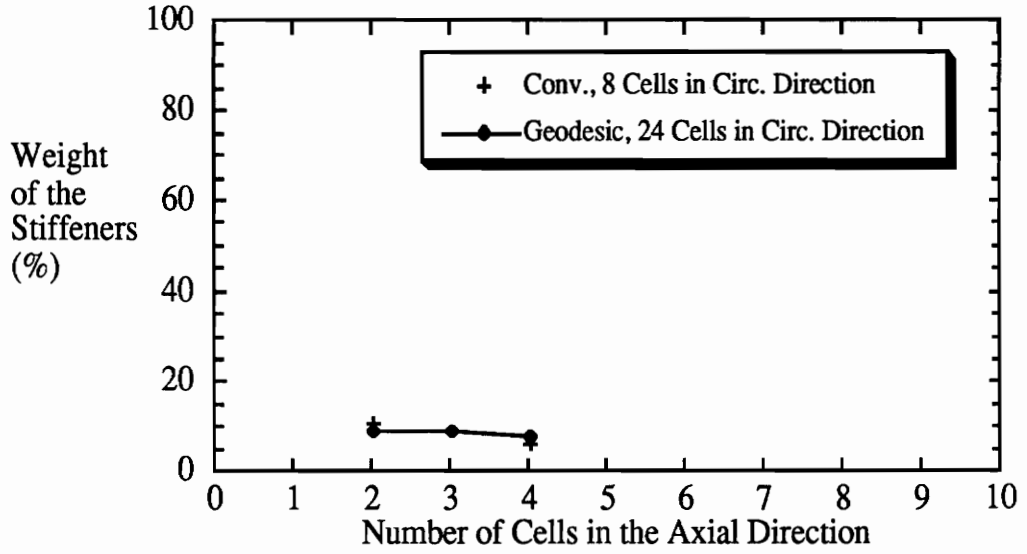

b – Increasing Number of Cells in the Axial Direction.

Fig. 5.16 – Stiffener Weight Fraction, Torsion.

cells in the circumferential direction, the stiffener cross-sectional area increases for 4 and 8 cells. It reaches its maximum for 16 cells, and then decreases smoothly for 24 and 32 cells. The initial increase is explained by the change in the angle of the stiffeners which allows them to carry a larger fraction of the applied load (see Fig. 5.15a). As in the case of the stiffener cross-sectional area, the fraction of the load carried by the stiffeners reaches its maximum for 16 cells in the circumferential direction. It then decreases for 24 cells and increases slightly for 32 cells. The portion of the load carried by the stiffeners is considerably lower than that for compression-loaded cylinders. The highest load fraction is 24% for the 16 cell cylinder under 1000 lb/in. Since the largest stiffener cross-sectional area also occured for 16 cells in the circumferential direction, it appears that the angle γ obtained for this geometry, 34°, corresponds to an optimum in terms of participation of the stiffeners in the carrying of the torsional load. However, contrary to the case of axial compression only, the maximum in the load fraction carried by the stiffeners does not correspond to the minimum-weight design, since reductions in weight still occur for 24 and 32 cells.

For the conventionally stiffened shell, both the cross-sectional areas of the stringers and the rings are shown in Fig. 5.14. In torsion, the stringers carry no axial load, and therefore they tend to be very tall and thin. However, they influence the shape of the buckling modes and increase the critical load of the shell. Therefore, there presence is justified. The cross-sectional area of the stringers for the two conventionally stiffened configurations are, in fact, significantly larger than those obtained for the geodesically stiffened configurations.

Increasing Number of Cells in the Axial Direction. The trends in stiffener cross-sectional area, stiffener load and weight fractions as a function of number of cells in the axial direction are shown in part b of Figs. 5.14, 5.15, and 5.16. Stiffener cross-sectional areas and weight fractions decrease as the number of cells are increased. At four cells, the

stiffener cross-sectional area is 65% of the one obtained for two cells. The first buckling modes obtained for the 3x24 and 4x24 geometries are similar to the one obtained for the 2x24 geometry (see Fig. 5.4). Since, the addition of cells in the axial direction result in a larger number of shorter stiffeners, each one of them does not need to be as stif to stabilize the skin.

The fraction of the load carried by the stiffeners increases sharply between two and three cells and then decrease slightly from three to four cells. For the 3x24 configuration, the portion of the load carried by the stiffeners represents 19% of the applied load. It is recalled that for an increasing number of cells in the circumferential direction, the maximum in stiffener load fraction has been obtained for the 2x16 geometry, a configuration that presents an angle γ between the stiffeners and the axis of the shell equals to the one presented by the 3x24 configuration.

Compared to the conventionally stiffened shell, there is little difference between the ring cross-sectional areas and those of the geodesic stiffeners. On the other hand, the stringer cross-sectional areas are significantly larger than those of the geodesic stiffeners. Since the stringers do not carry any load in torsion, they tend to be very thin and high. As was the case for the cylinder weight, the cross-sectional area of the stringers tends to decrease more rapidly that the cross-sectional area of the geodesic stiffeners.

5.2.4 Summary

In summary, the results obtained for the case of axial compression indicate that for a structurally efficient stiffened shell, the stiffeners must be designed to carry a large portion of the load. The addition of a small number of stiffeners that make large angles from the loading axis does not result in a significant increase in the buckling resistance of the structure. This is due to the small amount of load carried by such stiffeners. Also, since the first buckling mode of an unstiffened cylindrical shell presents a short wavelength

pattern, adding a small number of stiffeners does not significantly affect the buckling pattern and no substantial increase in the buckling load is obtained. The advantage of the conventionally stiffened shell is especially pronounced for a small number of cells in the circumferential direction and for the heavier load. The results obtained by considering a constant angle γ between the skin and the stiffeners have also indicated that weight savings can be achieved by increasing the stiffener density without changing the load distribution between the skin and the stiffeners.

In torsion, the geodesically stiffened shell is weight competitive compared to the conventionally stiffened configurations studied. It is interesting to note that geodesic stiffeners that present a large angle γ between the stiffeners and the axis of the shell significantly change the distribution of static displacements and consequently the shape of the first buckling mode from the one that would be obtained for an unstiffened shell. The first buckling mode then presents a short wavelenght pattern and no significant decreases in weight occur when the unstiffened sections of the skin become smaller. This is illustrated by the results obtained from the 2x16, 2x24, 3x24, and 4x24 configurations. On the other hand, when the angle γ becomes smaller and the stiffeners become more aligned with the shell axis, the first buckling mode switches to long half-waves. These half-waves are slightly inclined with respect to the axis of the shell and they extend over a large portion of the shell's length. In that case, the lack of stiffening members (such as rings) that could break this pattern precludes significant increases in buckling resistance.

5.3 Skin Laminate Trends

In the previous sections, trends in the design were obtained by studying configurations that present different numbers of cells in both the axial and circumferential directions. This study has allowed identification of more efficient configurations for a given loading regime and a comparison of the efficiency of the geodesically stiffened

configurations with more conventional stiffening patterns. To complement these results, it is instructive to examine how the design corresponding to a specific configuration is affected by changes in the skin lamination sequence. This aspect of the design study is discussed in this section for the cases of pure axial compression and pure torsion. For axial compression, it has been noted (see Section 5.2.2) that for the configurations that present 16 or more cells in the circumferential direction, the design variable that designates the thickness of the 0° plies in the skin reaches its lower bound. It is recalled that the angle of lamination of the skin plies is measured with respect to the axis of the cylinder. To study the effect of removing these plies from the skin, the 2x48 configuration subjected to 1000 lb/in of axial compression has been considered. Starting from the optimal design obtained with ±45°, 90°, and 0° plies in the skin, a new optimal design with ±45° and 90° plies only has been obtained. For this new optimal design, the design variable that designates the thickness of the ±45° plies reached its lower bound, and consequently, a skin laminate made of 90° plies only has been considered next. The results obtained are given in Table 5.6a and plotted in Fig. 5.17. In Fig. 5.17, the weight has been normalized with respect to the optimal weight obtained with ±45°, 90°, and 0° plies in the skin. It is seen that as the skin becomes more compliant, as a result of successively removing plies, the weight of the stiffened cylinder follows a downward trend. For example, the cylinder with the $[-45/45/90_{2.9}]_S$ skin laminate weighs 81% of the one with the $[-45_{1.9}/45_{1.9}/90_{2.9}/0]_S$. On the other hand, the portion of the total weight represented by the stiffeners and the fraction of the applied load carried by the stiffeners increase smoothly. This indicates that for axial compression, the design benefits from a more compliant skin which allows more load to be carried by the stiffeners. Note that the design variable that represents the thickness of the 90° plies does not reach its lower bound when only these plies are used in the skin laminate.

The results obtained in the present section also allow to evaluate the sensitivity of

Table 5.6 – Skin Laminate Trends.

a – Axial Compression.

	CASES		
	0°, 90°, and ±45° plies	90° and ±45° plies	90° only
t_0 (in)	0.005	N/A	N/A
t_{90} (in)	0.0143	0.0145	0.0176
$t_{\pm 45}$ (in)	0.00943	0.005	N/A
t_g (in)	0.158	0.191	0.303
h_g (in)	1.09	1.09	0.86
Cylinder Weight (lb)	328.9	266.2	252.8
Skin Laminate[1]	$[-45_{1.9}/45_{1.9}/90_{2.9}/0]_S$	$[-45/45/90_{2.9}]_S$	$[90_{7.0}]_S$

[1] Based on a ply thickness of 0.005 in

b – Torsion.

	CASES	
	0°, 90°, and ±45° plies	0° and 90° plies
t_0 (in)	0.0126	0.0158
t_{90} (in)	0.0339	0.0325
$t_{\pm 45}$ (in)	0.005	N/A
t_g (in)	0.106	0.162
h_g (in)	1.68	1.47
Cylinder Weight (lb)	412.3	384.1
Skin Laminate	$[-45/45/90_{6.8}/0_{2.5}]_S$	$[90_{6.5}/0_{3.2}]_S$

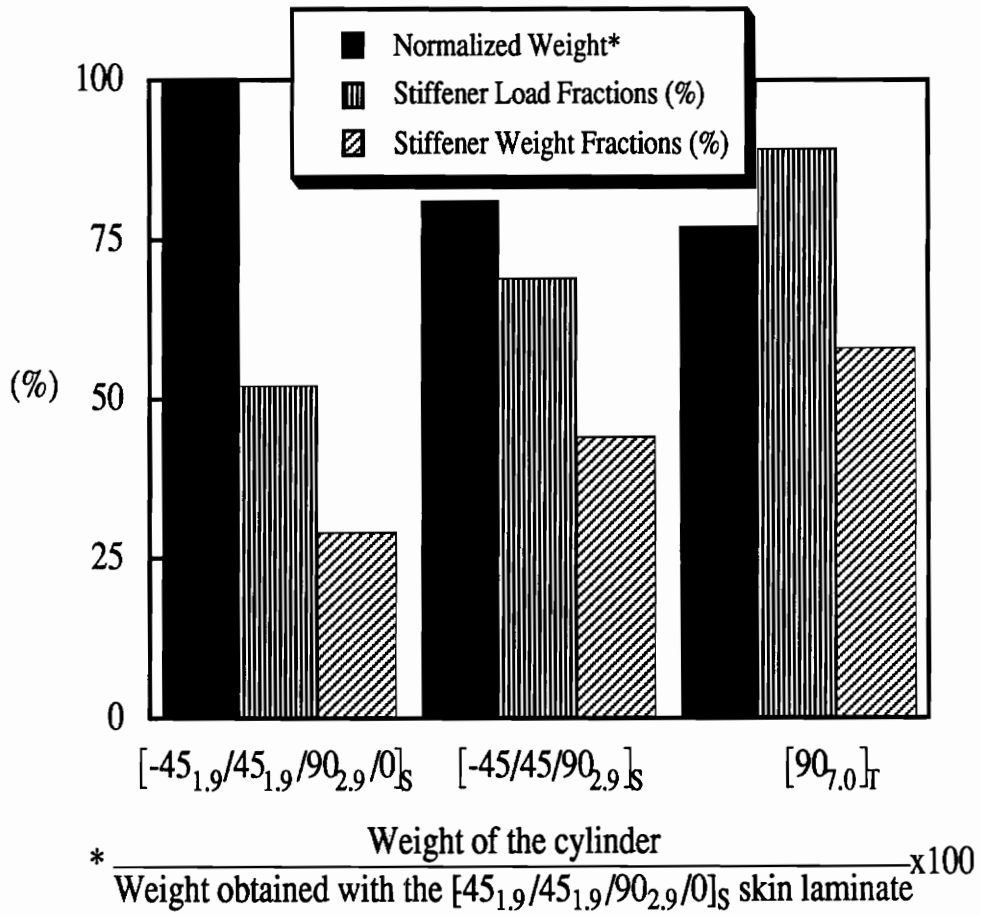

Fig. 5.17 – Skin Laminate Trends, Axial Compression.

the behavior described in Section 4.3 to changes in the ratio of the skin to stiffener stiffnesses. It is recalled that in Section 4.3, the behavior of the shell has been classified in either of two categories depending on the values of the angle γ between the stiffeners and the axis of the cylinder. For the 2x48 configuration, the stiffeners are in compression, and consequently, the behavior of this stiffened shell falls in the second category. As a result, bending stresses which produce important radial displacement gradients develop in the skin. Changes in the ratio of the skin to stiffener stiffnesses will influence this behavior as illustrated in Fig. 5.18 which shows the u_r component of the static displacement solutions corresponding to the optimal designs obtained for each skin laminate considered. In each case, the results correspond to unit axial displacements applied at each end. For the lamination sequence that has ±45°, 90°, and 0° plies, the membrane stiffness of the skin considerably restrains the outward deflections, and consequently, relatively small displacement gradients are obtained. As the skin stiffness decreases and the stiffener cross-sectional area increases (Figs. 5.18b and c), these gradients become more important. For the skin laminate that has 90° plies only, the unstiffened areas of the cylinder even display large negative radial displacements.

In torsion, the thickness of the 45° plies reaches its lower bounds for several of the more densely stiffened configurations (see Section 5.2.2). Consequently, the effect of removing these plies in the skin laminate has also been studied. The 2x32 configuration subjected to 1000 lb/in has been chosen, and the effect of removing the 45° plies in the skin laminate is studied. The results are given in Table 5.6b and plotted in Fig. 5.19. As indicated in Fig. 5.19, removing the 45° plies in the skin results in lighter designs. However the decrease in weight is smaller compared to the example studied for axial compression only. For example, the cylinder with the $[90_{6.5}/0_{3.2}]_S$ skin lamination sequence weighs 93% of the one with the $[-45/45/90_{6.8}/0_{2.5}]_S$ skin laminate. For the lighter design, a larger portion of the applied load is carried by the stiffeners which also

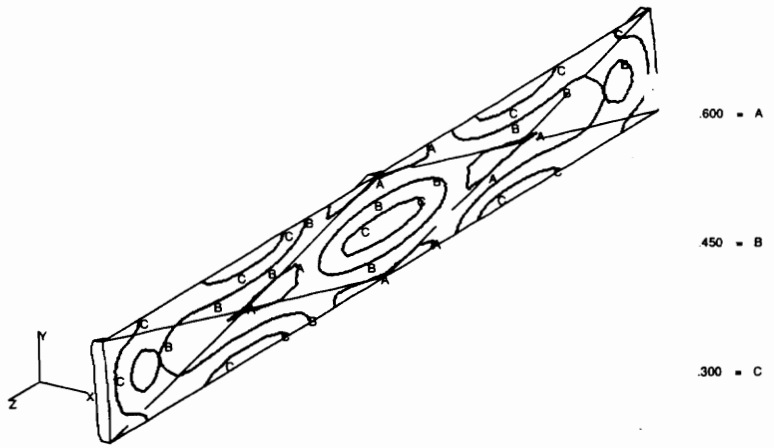

a – $[-45_{1.9}/45_{1.9}/90_{2.9}/0]_S$.

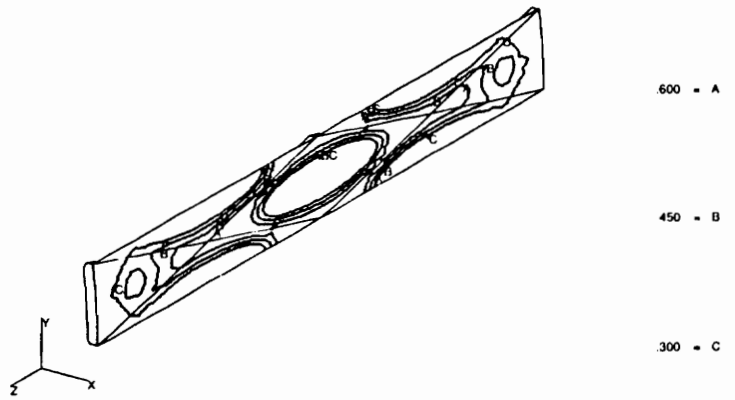

b – $[-45/45/90_{2.9}]_S$.

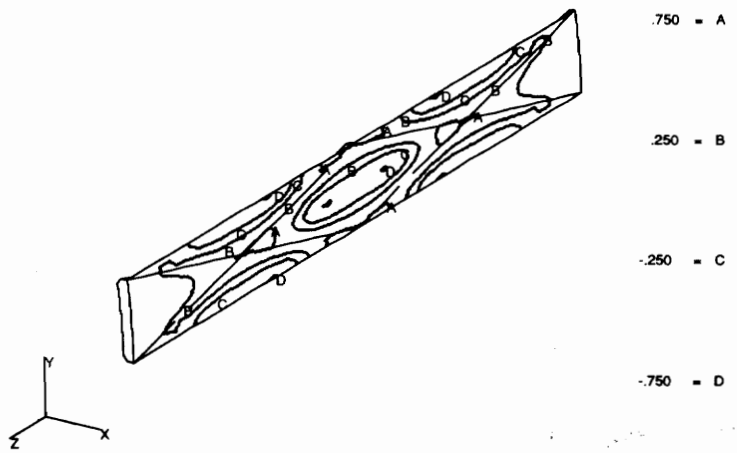

c – $[90_{7.0}]_S$.

Fig. 5.18 – u_r **Component of the Static Displacement Solutions for Three Different Skin Laminates.**

represent a larger fraction of the total cylinder weight. Note that as a result of removing the 45° plies, none of the other design variables went to their lower bounds.

5.4 Verifications

The design results discussed in this chapter have been obtained with the models presented in Chapter 4. Several of these models discretize only a portion of the shell and approximate boundary conditions are applied along lines of geometrical symmetries. In this section, the validity of these models is investigated by considering larger models. In the case of the 2x4 configuration in compression and the 2x8 configuration in compression, torsion and combined compression and torsion the results obtained with the partial models have been verified with the full model. In all the other cases, larger portions of the shell have been considered and the approximate boundary conditions used during the design study (see Chapter 4) have been applied along the lines of geometrical symmetries. Since the lowest eigenvalue of the buckling problem depends on the static solution and it is more difficult to predict than the distribution of the strains, the other component of the structural response used in the design study, it has been chosen as a measure of the accuracy of the finite element model. The results are given in Table 5.7. In the case of axial compression, the results obtained during the design study agree very closely with the one obtained with the larger models. The only deviation is with the 2x8 configuration for which the lowest eigenvalue obtained with the partial model differs by 8% from the one obtained with the full model.

In torsion, the results are also in very good agreement, except for the 2x32 conventionally stiffened shell in torsion for which a difference of 2% in the first eigenvalue has been obtained when comparing the 3 cell model used in the optimization study with a 6 cell model. It must be noted that the choice of the model used to study this particular geometry and loading case has been strongly influenced by the computational require-

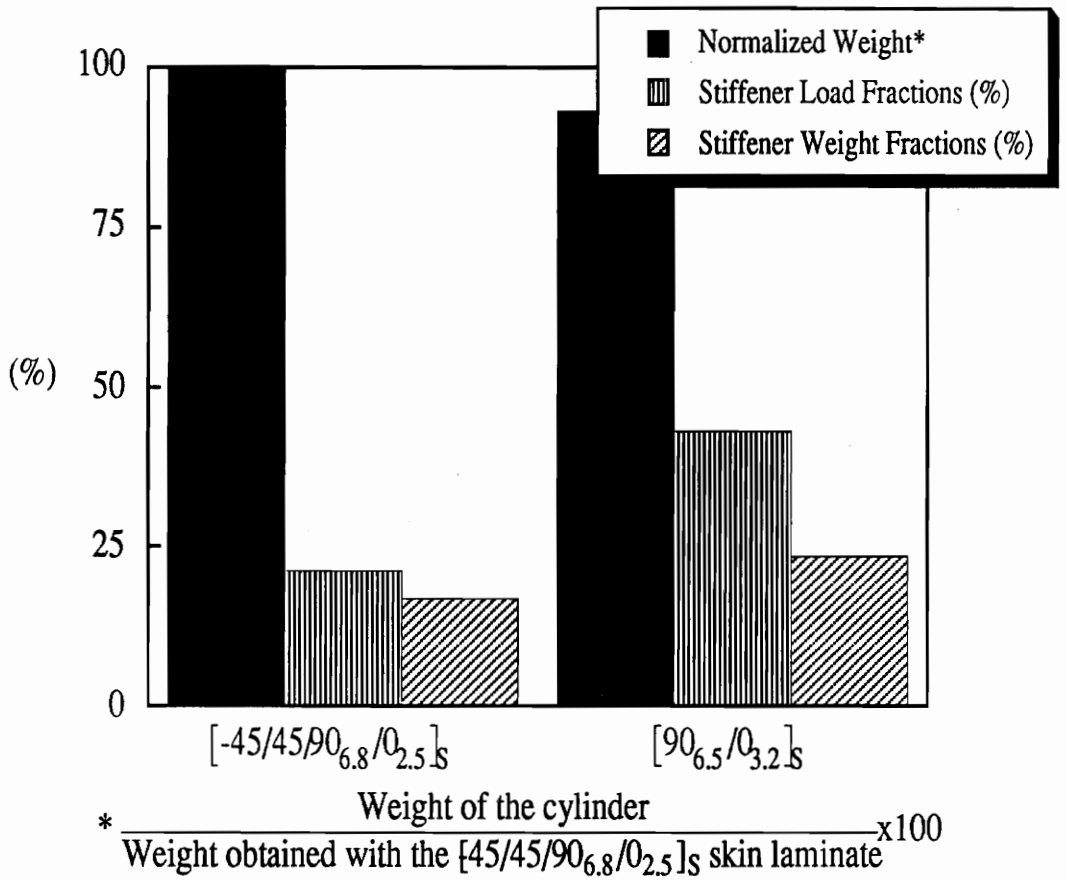

Fig. 5.19 – Skin Laminate Trends,Torsion.

ments. Also, a difference of 2% in the lowest eigenvalue does not necessarily translate itself into a similar increase in weight. Results presented in Section 5.2.1 have shown that changes of less than 4% in weight may occur for models that predict the lowest eigenvalue with as much as 9.5% of error.

5.5 Computational Requirements

In this section, CPU times required for the calculation of some of the optimal configurations presented in Section 5.1 are discussed. These results complement those presented in Section 5.2.1 where convergence characteristics have been discussed and estimates of the numbers of exact analyses required to obtain the optimal configurations have been given. In all the cases, the CSM Testbed processors INV, SSOL, and EIG have been used to calculate the static response and the eigensolution, respectively. Processor INV factors the assembled system matrix stored in sparse-matrix format, and processor SSOL performs forward reduction and back substitution on the factored system matrix. Processor EIG implements an iterative procedure involving a Rayleigh-Ritz approximation and a Stodola-Type method for extracting eigenpairs [16]. In all cases, the eigenvectors obtained at the previous design point have been used to start the calculation of the eigensolution. As the optimization run progresses, this contributes to a significant reduction in the number of iterations required to compute the eigensolution. The runs have been performed on a Convex C220 superminicomputer located at NASA Langley Research Center. The computer consists of two central processing units, each of which can compute from 20 to 40 MFLOPS for a computationally-intensive calculation.

The statistics obtained are presented in Table 5.8. The number of the six-degrees-of-freedom nodes included in the finite element model and the number of design variables considered in the optimization problem are given in the first two columns of the table. The CPU time required for the calculation of the static response, the geometric stiffness

Table 5.7 – Verifications.

Configuration	Loading	Level	Model	λ_1	Mesh
		(lb/in)			m_{ne} x n_{ne} x l_{ne}
Unstiffened	Compression	2700	L x 90°	1.001	12 x 12 x 1
			$L/2$ x 360°	0.9998	12 x 48 x 1
2 x 4	Compression	2700	L x 90°	1.001	16 x 8 x 1
			L x 360°	1.000	16 x 32 x 1
2 x 8	Compression	2700	L x 45°	1.018	12 x 6 x 1
			L x 360°	0.937	12 x 48 x 1
	Torsion	418.5	L x 135°	0.9994	12 x 18 x 1
			L x 360°	1.003	12 x 48 x 1
	Combined	2700 – 418	L x 135°	1.020	12 x 18 x 1
			L x 360°	1.000	12 x 48 x 1
2 x 16	Compression	2700	L x 22.5°	1.035	12 x 6 x 1
			L x 180°	1.043	12 x 48 x 1
	Torsion	418.5	L x 67.5°	1.001	12 x 18 x 1
			L x 135°	0.9990	12 x 48 x 1
2 x 24	Compression	2700	L x 22.5°	1.083	12 x 6 x 1
			L x 120°	1.084	12 x 48 x 1
	Torsion	418.5	L x 45°	0.9991	12 x 18 x 1
			L x 90°	0.9932	12 x 48 x 1
2 x 32	Compression	2700	L x 11.25°	1.118	12 x 6 x 1
			L x 90°	1.113	12 x 48 x 1
2 x 32 Conventional	Torsion	418.5	L x 33.75°	1.000	6 x 24 x 1
			L x 67.5°	0.9796	6 x 48 x 1
2 x 48	Compression	2700	L x 7.5°	1.137	12 x 6 x 1
			L x 60°	1.132	12 x 48 x 1
4 x 48	Compression	2700	$L/2$ x 7.5°	1.062	12 x 6 x 1
			L x 30°	1.058	24 x 24 x 1
8 x 48	Compression	2700	$L/2$ x 7.5°	1.011	24 x 6 x 1
			$L/2$ x 30°	1.019	24 x 36 x 1

matrix and its assembling is given in column 3. In the next column, the CPU time required for one iteration in the eigensolver is given. The number of iterations in the eigensolver required during a specific design run is problem dependent and, as mentioned above, tends to decrease as the optimization run progresses. For the size of problems considered in the design study, between 30 and 40 iterations were required to converge the lowest eigenvalue for the initial design. As the optimization progresses, the number of iterations usually decreased to approximately 8 and, for the last few design points, only 2 iterations (the minimum number of iterations required to measure the degree of convergence) were generally required. For a design run that would require 20 design iterations, it is estimated that approximately 120 iterations would be required in the eigensolver. Finally, the last column gives the CPU time required for the calculation of the derivatives of the constraints with respect to the design variables. In all cases, the semi-analytical strategy (see Section 3.3.3) has been used. As an illustration of the overall computational time required for the calculation of an optimal design, consider the problem that counts 2073 nodes and five design variables. For that problem, almost 11 CPU hrs. are required to perform 20 design iterations.

As indicated by these results, the calculation of optimal designs for the class of structures considered in the present study is computationally very intensive. It has forced the use of partial models which were also required to limit the amount of disk space storage. Finally, since the analysis, without the inclusion of the time required for the eigensolution, is more expensive than the derivative calculations (columns 3 and 5 of Table 5.8), it can be concluded that the use of the SA strategy results in savings over the OFD approach. Also the amount of savings achieved tends to increase with the size of the problem.

Table 5.8 – CPU Times[1] Required for the Calculation of Optimal Designs.

Number of of nodes	Number design variables	CPU time for Analysis[2] (sec.)	CPU time in eigensolver[3] (sec.)	CPU time for derivative calc.[4] (sec.)
659	7	84.8	9.0	81.0
1211	7	182.7	20.0	142.3
2073	5	425.1	41.0	261.6
3299	5	771.7	75.0	415.7

[1] The runs have been performed on a Convex C220 superminicomputer.

[2] Does not include CPU time required for eigensolution.

[3] Per iteration in the eigensolver.

[4] Per design variable.

Chapter 6
Global/Local Analysis and Design

The design study presented in the previous chapter is based on constraints that have been evaluated using the "global" response of the structure. No considerations have been given to localized effects such as the stress concentration around a stiffener intersection or the tendency of the stiffeners to delaminate from the skin. Considering such aspects in a design process would require the use of much refined meshes or even three-dimensional models and such a brute force would likely saturate even the largest computers available today or even in the foreseeable future. This has been recognized by many researchers in the field of structural analysis and several methods have been developed to reduce the cost of predicting the localized effects in complex structural configurations.

These methods are usually known as global/local analysis strategies, and although considerable work has been reported in the literature on the development of such techniques, no work has been documented on the inclusion of a global/local analysis strategy into an optimization process. This is the subject of this chapter which describes the work done to implement a two-dimensional to two-dimensional (sometimes called "zooming") global/local analysis strategy into an optimization process. The justification for addressing this issue in the context of this research is first outlined. Then, the methodology of the global/local analysis and the modifications that have been made to the optimization system previously presented in Chapter 3 are described. Finally, an example that validates the implementation of the strategy is presented.

6.1 Justification

The economy realized in the study of complex structural configurations is normally

the first argument put forward to justify the use of a global/local analysis strategy. These economies result from using a refined mesh, or a computationally more expensive theory, over only a smaller region of the domain to predict the localized effects. For example, the design of stiffened panels may be performed using beam elements to model the behavior of the stiffeners. Consequently, no local buckling of these members can be predicted. In this case, a local model, accommodating plate elements, could be used to predict such buckling modes and provide the design process with information on the stiffener dimensions that must be used to avoid local buckling of the stiffeners. Another example could be the design of composite structures with stress concentrations. It is well-known for composite materials that through-the-thickness stress components are sometimes responsible for delaminations that result into failure of the structural component. The finite element models used in the study of complex structural configurations, however, are usually plate or shell models that cannot predict through-the-thickness effects. In such a case, a local model that would implement either a refined plate or three-dimensional elasticity theory could be used to provide the design with information on the magnitude of the critical through-the-thickness stress components. Other examples, where local models could be used, include the prediction of the strain gradient distribution at the skin stiffener intersection of a stiffened panel [34] and the calculation of the stress concentration factor for panels with cutouts [35]. Another reason for addressing the issue of global/local analysis and design is to allow the assessment of the feasibility and the computational requirements of using such a strategy in a design process.

6.2 Methodology of Global/Local Analysis and Design

In this section, the methodology used for the global/local analysis is first described. This description is based on the work presented in Ref. [35]. Secondly, the formulation of the design problem is presented. This presentation includes the modifications that take

into account the additional term that arises in the calculations of constraint derivatives (see Section 3.3.3) at the local level. The details of the organization of the data base and the new processors required for the implementation of the global/local strategy are described in Appendix C. This work expands the capabilities of the optimization system already presented in Chapter 3 and in Ref. [27].

6.2.1 Global/Local Analysis [35]

The global/local analysis stress strategy used herein is defined as a procedure to determine local, detailed stress states for specific structural regions using information obtained from an independent global stress analysis. It employs separate, locally refined, finite element models for specific regions that need a more detailed interrogation. As a result, *a priori* knowledge of the regions that will eventually need a more detailed interrogation is not required.

Three main reasons may be invoked to justify the choice of this strategy. The first reason concerns the amount of validation work that has been recently published on both two-dimensional to two-dimensional (Ref. [35]) and two-dimensional to three-dimensional global/local analysis (Ref. [36]). Secondly, as a result of the work of Ransom, the interpolation procedures that are used in this study are now available in the CSM Testbed. This considerably reduced the amount of work associated with the generation of refined displacement fields and, as such, shortened the time required for the implementation of the strategy. Finally, the modularity of the resultant implementation constitutes another reason for the choice of this global/local strategy. On parallel computers, this modularity could eventually be used to perform the computations related to each model on different processors.

The local model refers to any structural subregion within the defined global model. The terminology of the global/local methodology presented herein is depicted in Fig. 6.1.

The global model is a finite element model of a structural component. A region requiring a more detailed interrogation is subsequently determined. An interpolation region is then identified around the critical region as indicated in Fig. 6.1b. The global/local interface boundary, indicated in Fig. 6.1c, defines the intersection of the boundary of the local model with the global model. The definition of the interface boundary may affect the accuracy of the interpolation procedure and thus the local stress state. Criteria for defining the interface boundary are discussed in Ref. [35].

To determine local, detailed stress states, the method requires that a finite element analysis of the global structure is first performed to obtain its overall response. Then, a critical region is identified from the results of the global analysis. Finally, the global solution is used to obtain an applied displacement field along the boundary (*i.e.*, boundary conditions) of an independent local model of the critical region. The applied displacement field is computed using a spline interpolation of the displacements and rotations calculated from a global analysis. Spline interpolation is a numerical analysis tool used to obtain the "best" local fit through a set of points. Spline functions are piecewise polynomials of degree m that are connected together at points called knots so as to have $(m-1)$ continuous derivatives. The interpolation problem may be stated as follows:

$$[\mathbf{S}(x_i, y_i)] \begin{Bmatrix} a_1 \\ a_2 \\ \cdot \\ \cdot \\ \cdot \\ a_q \end{Bmatrix} = \begin{Bmatrix} b_1 \\ b_2 \\ \cdot \\ \cdot \\ \cdot \\ b_q \end{Bmatrix}, \tag{6.1}$$

where $[\mathbf{S}(x_i, y_i)]$ is a matrix of interpolated functions evaluated at q points, the vector $\mathbf{a}$ defines the unknown coefficients of the interpolation functions, and the vector $\mathbf{b}$ consists of known values of the field b being interpolated based on q points in the global model.

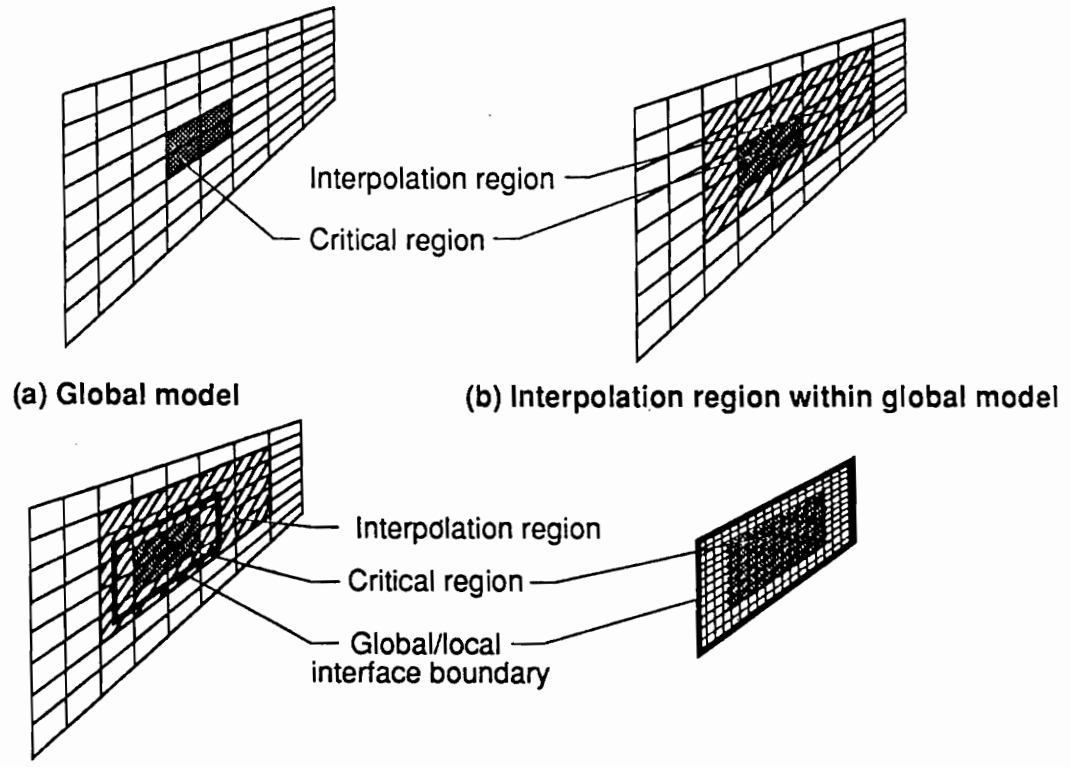

Fig. 6.1 – Terminology of the Global/Local Methodology (from Ref. [35]).

To interpolate local values, the matrix S is formed, inverted, and multiplied by b to compute the vector a. The vector a is then used to interpolate the local values through the following equation:

$$b_{g/l}(x_i, y_i) = a_o + a_1 x_i + a_2 y_i + a_3 x_i^2 + a_4 x_i y_i + a_5 y_i^2 + a_6 x_i^3 + a_7 x_i^2 y_i +$$

$$a_8 x_i y_i^2 + a_9 y_i^3 + \sum_{j=1}^{n} F_j r_{ij}^2 ln(r_{ij}^2), \quad i = 1, 2, \ldots, l, \tag{6.2}$$

where $b_{g/l}$ denotes the refined interpolated field, and l the number of points for which b must be evaluated.

6.2.2 Optimization Problem

Although a two-level global/local strategy is used to predict the structural response, a single optimization problem is formulated. In the terminology of optimization theory, this corresponds to a one-level solution strategy. This implies that a single set of design variables and a single objective function are defined. However, constraints can be evaluated using the structural response obtained from either the global or the local model. The approach used herein is consequently different from the multilevel optimization strategies documented in the literature (see, for example, Refs. [37–39]). As a result of adopting a one-level solution strategy, the formulation of the optimization problem does not significantly differ from what has already been presented in Chapter 3. The only major modification occurs in the calculation of the constraint derivatives at the local level, and the formulation that must be used in this case is now presented.

The formulation used for the calculation of the constraint derivatives with respect to the design variables has already been presented in Section 3.3.3, Eqs. (3.6)–(3.17). For the global model, this formulation is still valid, and the developments presented in the above mentioned section can be directly used to compute the derivatives. The key

information in the computation of the derivatives of the three types of constraints supported by the optimization system (see Eqs. (3.3)–(3.5)) consists of the derivatives of the static displacement solution with respect to the design variables. Once this information is known, simple operations can be performed to obtain the derivatives of the constraints.

In the case of a local model, the equilibrium equations can be written:

$$\begin{bmatrix} \mathbf{K}_{1,1} & \mathbf{K}_{1,2} \\ \mathbf{K}_{1,2}^T & \mathbf{K}_{2,2} \end{bmatrix} \begin{Bmatrix} \mathbf{u}_{lu} \\ \mathbf{u}_{lc} \end{Bmatrix} = \begin{Bmatrix} \mathbf{0} \\ \mathbf{R} \end{Bmatrix} \tag{6.3}$$

(cf. 3.7), where $\mathbf{u}_{lu}$ and $\mathbf{u}_{lc}$ represent the unconstrained and constrained components of the displacement vector obtained from the local analysis, respectively. For a local model, contrary to the case of a global analysis, the displacement vector $\mathbf{u}_{lu}$ obtained by solving Eq. (6.3) does not need to be scaled. Scaling is unnecessary since the vector of nonzero displacement boundary conditions, $\mathbf{u}_{lc}$, has been formed using the static displacement solution corresponding to the design load. Referring to Section 3.3.3, $\mathbf{u}_{lc}$ has been extracted from $\mathbf{u}_d$ which is scaled and represent the static displacements that occur when the structure is subjected to the design load F_d. As a result, in the case of a local model, $s(\mathbf{x})$, the scale factor defined in Eq. 3.10, is always 1. Thus, its derivative with respect to a design variable is 0. In this context, the derivatives of the unconstrained components of the displacement vector are consequently given by:

$$\mathbf{K}_{1,1}\frac{d\mathbf{u}_{lu}}{dx_i} = -\mathbf{K}_{1,1}\frac{d\mathbf{u}_{lc}}{dx_i} - \frac{d\mathbf{K}_{1,2}}{dx_i}\mathbf{u}_{lc} - \frac{d\mathbf{K}_{1,1}}{dx_i}\mathbf{u}_{lu} \tag{6.4}$$

(Compare to Eq. 3.15). In Eq. 6.4, the term $-\mathbf{K}_{1,1}\frac{d\mathbf{u}_{lc}}{dx_i}$ has been added since, in general, the static displacement solution at the boundary of the local model is influenced by a change in the value of the design variable x_i. This term consequently represents the change in the load distribution due to a change in the value of x_i. In the case of a global model, $\mathbf{K}_{1,1}\frac{d\mathbf{u}_{lc}}{dx_i}$ is 0 since the boundary conditions applied to the global model are constant. The term $\frac{d\mathbf{u}_{lc}}{dx_i}$ is computed by extracting from $\frac{d\mathbf{u}_d}{dx_i}$ the components

corresponding to the nodes located on the boundary of the interpolation region. These components are then processed by the interpolation procedure to generate $\frac{d\mathbf{u}_{Ic}}{dx_i}$. Once $\frac{d\mathbf{u}_{Ic}}{dx_i}$ has been obtained, Eq. 6.4 can be solved for $\frac{d\mathbf{u}_{Ix}}{dx_i}$. The vectors $\frac{d\mathbf{u}_{Ic}}{dx_i}$ and $\frac{d\mathbf{u}_{Ix}}{dx_i}$ are then formed into a single one and used to expand the solution vector $\mathbf{u}_I$ into a first-order Taylor series expansion. Then, the steps outlined in Section 3.3.3 for the calculations of the constraint derivatives once the derivative of the solution vector with respect to a design variable is known can be used. It is recalled that the main reason for the sensitivity analysis to result into savings is that no new factorization of the system matrices is required. This holds true in the case of a local model.

6.2.3 General Organization

The general organization of the calculations is shown in Fig. 6.2. The new processors that have been developed are described in Appendix C. This organization presumes that a previous analysis of the global model has been performed. Therefore, the regions that will need a more detailed interrogation have already been identified. As a result, the interpolation regions and the local model are defined immediately after the global model has been set up. This occurs before the first exact analysis of the global model is performed. Then, ADS is fired up and the default values assigned to the parameters that control the optimization process can be reset. The operations necessary for the calculation of an optimum can then be started. These calculations are as indicated in Fig. 6.2. Note that the optimization system supports local models that include several interpolation regions. Such a feature is necessary, for example, in the design of stiffened structures when one of the stiffener intersections represents the local region of interest. Because the interpolation procedure uses surface splines, the definition of separate interpolation regions for the skin and the stiffeners is necessary in such a case.

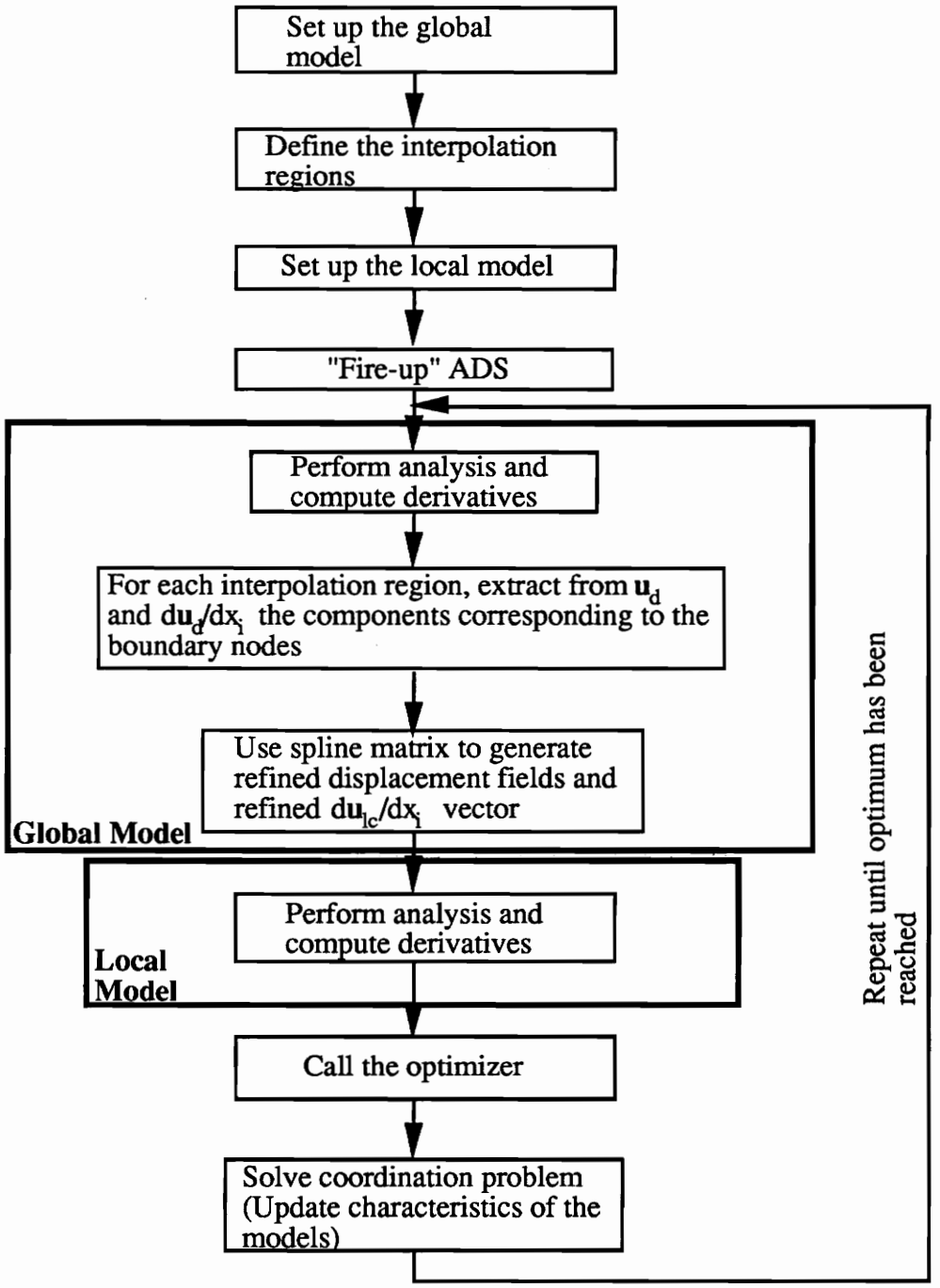

Fig. 6.2 – Organization of the Calculations in the Context of Global/Local Analysis and Design.

6.3 Validation

In this section, an example is presented to validate the formulation presented in the previous sections of this chapter. Since the optimization system has already been validated on several examples in other sections of this study, only the new procedures that perform the calculation of the constraint derivatives and the coordination work between the models (see Appendix C) will be validated here.

6.3.1 Example 1

In this example, the optimal design of a rectangular panel with a central circular cutout is considered. Examples of panels with cutouts have been used extensively by the global/local analysis researchers to validate their strategy. This is partly due to the facts that closed-form elasticity solutions are available, and also because the analysis of these structures benefit particularly from using a global/local strategy. This example problem has been analyzed in Ref. [35].

The isotropic panel considered is shown in Fig. 6.3. The overall panel length L is 20 in, the overall width W is 10 in, and the cutout radius r_o is 0.25 in. This geometry gives a cutout diameter to panel width ratio of 0.05 which corresponds to a stress concentration factor of 2.85 (see Ref. [35]). The loading is uniform axial compression with the loaded ends of the panel clamped and the sides free. The material system for the panel is aluminium with a Young's modulus of 10,000 ksi and Poisson's ratio of 0.3.

The finite element mesh shown in Fig. 6.4 is used to model the global behavior of the panel. It also constitutes a good approximation to its local behavior. The finite element model has a total of 160 9-node quadrilateral elements and 600 nodes. The element corresponds to a curved C^o shell element that has been installed in the CSM Testbed and denoted ES1/EX97.

The in-plane stress resultant distributions obtained with the global model reveal

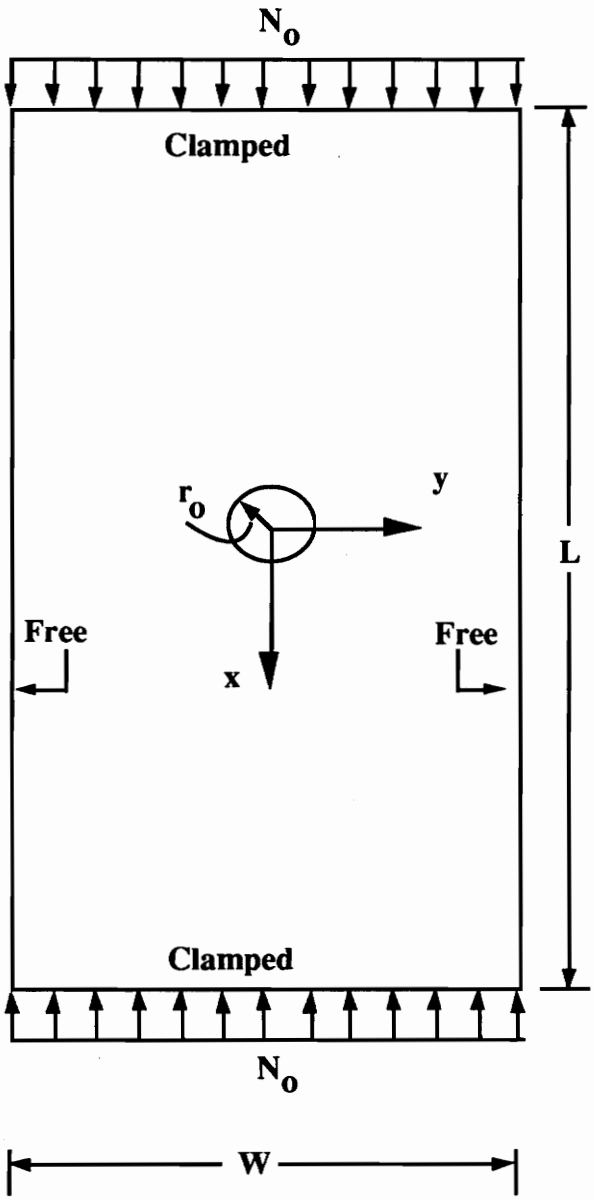

Fig. 6.3 – Isotropic Panel with a Circular Cutout.

several features of the global structural behavior of this panel. They also constitute guidelines for the definition of the boundary for the definition of the local model. Based on these distributions, the shaded area shown in Fig. 6.4 has been identified as a critical region and discretized using a more refined finite element model. However, the interpolation region used to generate the spline matrix corresponds to the entire plate. The local model, shown in Fig. 6.5, has a total of 144 9-node elements and 624 nodes. The same element used for the global model has been used in the refined model.

The optimization system has been applied to the minimum-weight design of the plate. Two constraints are considered: a buckling constraint, and a maximum strain failure criterion constraint evaluated along the edge of the cutout, at panel midlength. They are evaluated using the structural response obtained from the global and the local model, respectively. Since the material is isotropic, the strain at failure of the material has also been assumed isotropic and set to 0.002. A single design variable, the thickness t of the plate, is considered. The initial design corresponds to a thickness of 0.1 in and for this design, both constraints are violated.

For the optimal design, only the buckling constraint is active. The optimal thickness value is 0.226 in. The optimization run has required a total of 7 design iterations, each iteration requiring a total of 363 CPU s on a Convex C220 superminicomputer. The history of the optimization run is shown in Fig. 6.6. In the context of global/local analysis and design, a design iteration includes the calculation of the constraints and their derivatives for each model.

The distribution of the longitudinal stress resultant N_x at the panel midlength normalized by the nominal stress resultant is shown in Fig. 6.7 for the optimum design. Although the shape of the distribution does not change as the design is modified, the plot shown in Fig. 6.7 indicates that to accurately predict the stress concentration factor at the edge of the cutout, a very refined mesh must be used. Predicting this factor using a

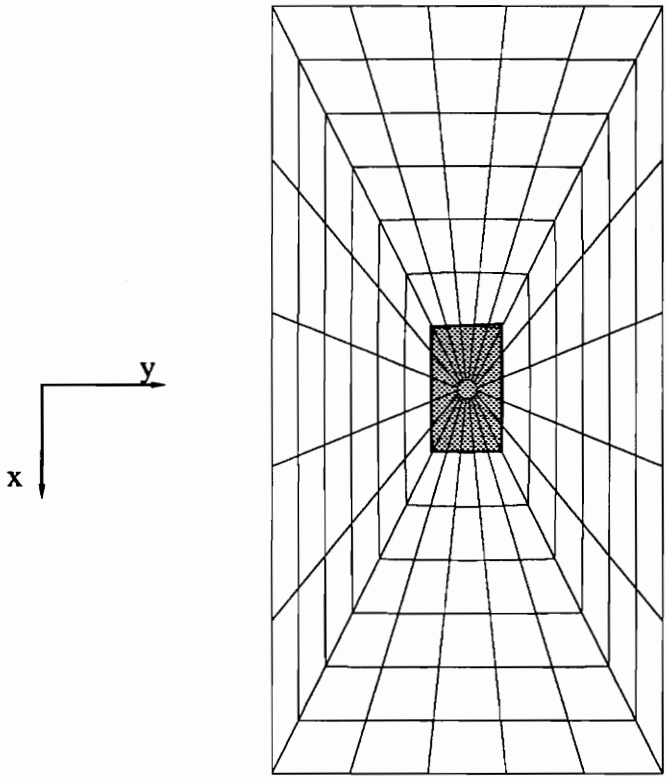

Fig. 6.4 – Global Finite Element Model.

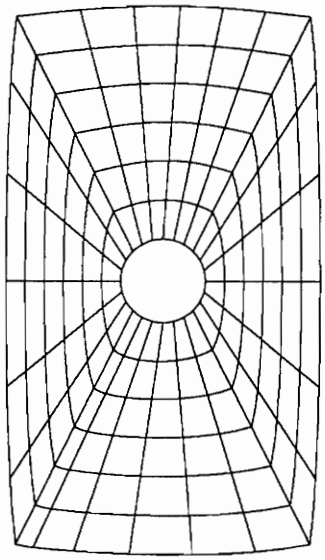

Fig. 6.5 – Local Finite Element Model.

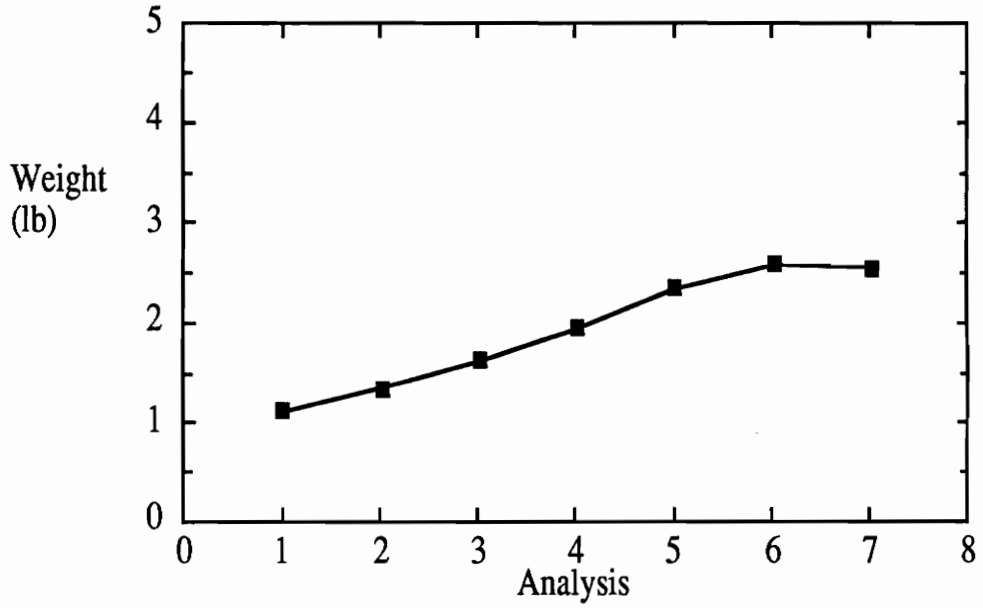

Fig. 6.6 – History of the Optimization Run.

single-level analysis would require a refined mesh around the cutout which would result in a computational cost increase for the optimization run. For example, the cost of the buckling analysis would then substantially increase compared to predicting the buckling load with the model shown in Fig. 6.4.

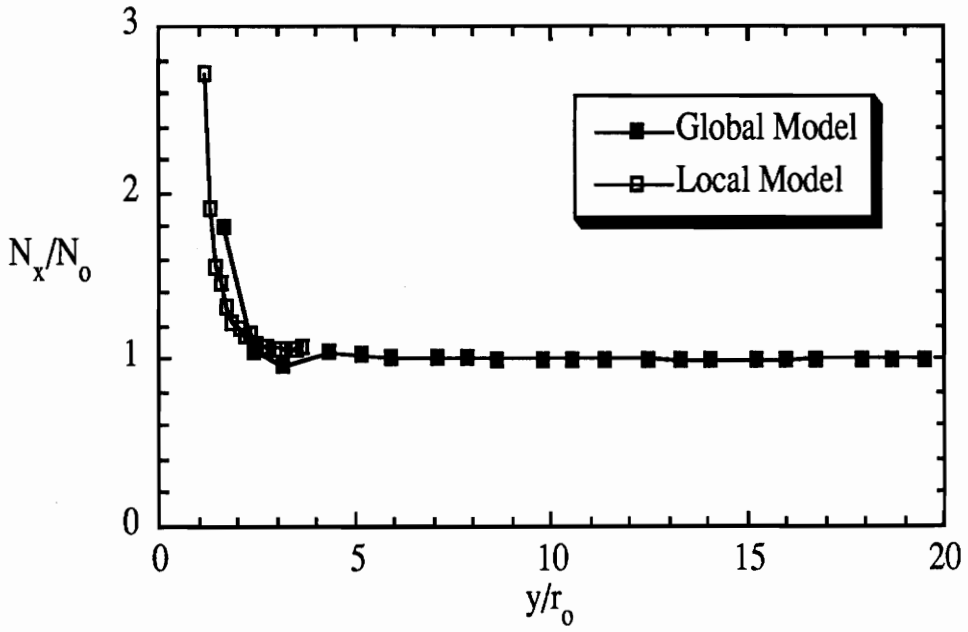

Fig. 6.7 – In-plane Axial Stress Resultant N_x Distributions Obtained for Each Model.

Chapter 7
Concluding Remarks

- A preliminary design study of minimum-weight geodesically stiffened shells for aircraft fuselages has been performed. Because of the need for an optimization tool capable of analyzing complex structural configurations, such as the geodesically stiffened shell, a new optimization system based on the finite element code CSM Testbed and the optimization program ADS has been developed. As such, the optimization system can be used to minimize the weight of any structure that can be analyzed via a finite element model subject to buckling, displacement, and material failure constraints. Three types of design variables can be defined. They correspond to the thicknesses or orientations of individual plies of finite elements or groups of finite elements. The third type of design variable corresponds to the size of finite elements. It consequently allows a limited amount of shape optimization in terms of stiffener heights to be performed. Although, the first type of design variable is referred to as a ply thickness, it can be used to design the thickness of a component in the case of an isotropic material. The loading can be applied using either nodal forces or displacement boundary conditions. In the latter case, an automatic procedure has been implemented to scale the structural response to the level of the design loads. Both overall finite difference and semi-analytical sensitivity derivative schemes have been implemented for the calculation of the constraint derivatives with respect to the design variables. Finally, the number of buckling constraints that must be imposed is determined by a procedure based on the derivatives of the eigenvalues with respect to the design variables. The optimization system has been validated on examples that have shown that it can be used to design structures that present a complex buckling

response subjected to combined load conditions.

- The analysis of geodesically stiffened shells subjected to compressive and torsional loadings has provided an insight into the load distribution and prebuckling deformations of the shells as the angle between the stiffener and the axis of the shell is varied. In compression, for a high value of this angle, tension due to the Poisson's expansion of the shell develops in the stiffeners. As the angle becomes smaller, the stiffeners start carrying a larger portion of the axial load, and, as a result of their curvature, generate substantial radial displacement gradients. In torsion, radial displacement gradients also develop since half of the stiffeners are in tension and the other half are in compression. For this loading condition, the skin section between the stiffeners deforms into a doubly-curved surface as two of the stiffeners that surround it are in tension and tend to pull the skin inward, and the other two tend to push it outward.
- The design study has shown that minimum-weight cylinders have relatively closed spaced stiffeners. Under pure axial compression, the minimum-weight design corresponds to the configuration with the highest number of cells in the circumferential direction. For this loading condition, the conventionally stiffened shell is more efficient that the geodesically stiffened one, especially for the heavier load. Under pure torsion, there is little difference between the minimum weights obtained for both stiffening patterns. The same is true for combined compression and torsion of equal magnitudes. For 2700 lb/in of compression and 418.5 lb/in of torsion, the efficiency of the conventionally stiffened shell under pure axial compression makes the designs obtained for this load combination lighter than the ones obtained for the geodesically stiffened shell.
- In compression, the stiffeners play a more active role as the maximum stiffener load fraction is close to 60% compared to 25% in torsion. This is among the reasons why

the conventionally stiffened shell is so efficient in compression since their stiffeners, even for a small number of them, still carry a large portion of the applied compressive load.

- No consideration has been given to the difference in the manufacturing cost of the different stiffened configurations. It is likely that since the geodesically stiffened configurations can be filament-wound, their manufacturing cost will be lower than a corresponding conventionally stiffened configuration.
- The design study has also shown that achieving convergence in the values of individual design variables requires many more design iterations that converging the value of the weight. The results obtained by replacing the reciprocal approximation used for the buckling constraint by the Sequential Convex Programming strategy by a linear approximation have also shown that convergence in the values of the design variables may be achieved faster with the linear approximation. Although the conservativeness of the reciprocal approximation helps during the first few design iterations by allowing larger move limits to be used, it also decreases the rate of convergence in the values of the design variables once a design for which some of the constraints become critical has been obtained.
- Skin laminate trends have shown that under compressive loading the design benefits from removing the 0° plies from the skin. This is due to the more compliant skin which allows more load to be carried by the stiffeners. The lightest design has been obtained for a skin laminate that includes 90° plies only. For this skin laminate and the 2x48 configuration, 58% of the applied load is carried by the stiffeners. Under torsion, a lighter design has resulted from removing the 45° plies from the skin of the 2x32 configuration.
- The design study has also shown that although weight savings could be achieved by properly choosing the stiffener arrangement of the carrying structure, considerable

savings can also be achieved by properly tailoring the skin laminate. For example, under axial compression, a weight reduction of 20% has been obtained by removing the 0° plies in the skin laminate.

- A global/local analysis and design strategy has also been presented. The strategy employs a single-level optimization problem. The two-level analysis procedure uses a zooming global/local finite element technique. Constraints can be evaluated using either the structural response obtained from the global or the local model. The semi-analytical sensitivity analysis formulation has been modified to account for the extra term that appears in the case of a local model. The implementation of the overall strategy has been validated on an example.

7.1 Recommendations for Future Work

- As indicated in Chapter 5, the calculation of optimal designs for configurations that present several thousands of degrees-of-freedom is a computationally intensive task. The present optimization system uses a direct method for the solution of the equilibrium equations. A possible enhancement could be to add the possibility of using an iterative algorithm. As the optimization progresses, the static solution obtained at the previous design point would become a very good estimate of the solution at the current design point, resulting in a rapid convergence. Another important component in the overall cost of the optimization was the calculation of the eigenvalues of the optimization problem. The present algorithm uses an iterative procedure involving a Rayleigh-Ritz approximation. It could be replaced by the Lanczos algorithm which is especially efficient when only a few of the smallest eigenvalues are desired.
- Concerning the design study, it has been shown that under axial compression and pure torsion important displacement gradients develop due to the curvature of the stiffeners. To better evaluate the impact of these displacements on the buckling

and post-buckling responses of the stiffened shell, nonlinear analyses of the optimal designs should be performed. Such displacements are likely to cause important through-the-thickness stress components at the skin/stiffener interface. To evaluate their magnitude, the zooming global/local strategy could be improved to include a local three-dimensional model that could predict the value of these stress components.

REFERENCES

[1] Reddy, A.D., Valisetty, R.R., and Rehfield, L.W., "Continuous Filament Wound Composite Concepts for Aircraft Fuselage Structures, " Journal of Aircraft, Vol. 22, No. 3, pp. 249-255, 1985.

[2] Rehfield, L.W., Deo, R.B., and Renieri, G.D., "Continuous filament Advanced Composite Isogrid: A promising Structural Concept, " Fibrous Composites in Structural Design, Plenum Publishing Corporation, pp. 215-239, 1980.

[3] Sun, G. and Hansen, J.S., "Optimal Design of Laminated-Composite Circular-Cylindrical Shells Subjected to Combined Loads, " Journal of Applied Mechanics, Vol. 55, pp. 136-142, 1988.

[4] Gajewski, A. and Zyczkowski, M., Optimal Structural Design under Stability Constraints, Kluwer Academic Publishers, 1988.

[5] Meyer, R.R., " Buckling of 45° Eccentric-Stiffened Waffle Cylinders, " Journal of the Royal Aeronautical Society, Vol. 71, pp. 516-520, 1967.

[6] Soong, T.C. , " Buckling of Cylindrical Shells with Eccentric Spiral-Type Stiffeners, " AIAA Journal, Vol. 7, No. 1, pp. 65-72, 1971.

[7] Lee, R.L. and Lu, S.Y.,"General Instability of Inclined-Stiffened Cylinders under Bending, " Journal of Applied Mechanics, pp. 403-407, September 1969.

[8] Pappas, M. and Amba-Rao, C.L., "Structural Synthesis of Thin, Cylindrical Shells with Spiral-Type Stiffeners, " AIAA Journal, Vol. 8, No. 8, pp. 1529-1530, 1970.

[9] Karmakar, R., "Axially Compressed Optimum Cylinder – Comparison of Stiffener Configurations, " Journal of Spacecraft and Rockets, Vol. 17, No. 5, pp. 477-479, 1980.

[10] Rehfield, L.W. and Reddy, A.D., "Damage Tolerance of Continuous Filament Composite Isogrid Structures: A Preliminary Assessment, " Composite Materials, Proc. Japan-U.S. Conference, Tokyo, pp. 471-477, 1981.

[11] Hayashi, T., "Buckling Strength of Cylindrical Geodesic Structures, " Composite Materials, Proc. Japan-U.S. Conference, Tokyo, 1981.

[12] Sandhu, J.S., Stevens, K.A., and Davies, G.A.O., "Torsional Buckling and Post-buckling of Composite Geodetic Cylinders with Special Reference to Joint Flexibility, " Composite Structures, Vol. 15, pp. 301-322, 1990.

[13] Sandhu, J.S., Stevens, K.A., and Davies, G.A.O., "Torsional Buckling and Post-Buckling of a CFC Geodetic Cylinder, " Composite Structures, 5, I.H. Marshall (Editor), Elsevier Science Publishers, 1989.

[14] Phillips, J.L. and Gürdal, Z., "Analysis and Optimum Design of Geodesically Stiffened Composite Panels, " Composite Materials Design and Analysis, Proceedings of the Second International Conference on CAD in Composite Materials Technology, Brussels, April 1990, pp. 509-528.

[15] Ambur, D.R. and Rehfield, L.W., "Effect of Stiffness Characteristics on the Response of Composite Grid-Stiffened Structures, " 32th AIAA/ASME/ASCe/AHS Structures, Structural Dynamics and Materials Conference, Baltimore, Maryland, April 8-10, 1991.

[16] Stewart, C.B. (compiler), "The Computational Structural Mechanics Testbed User's Manual, " NASA TM-100644, 1989.

[17] Knight, N.F., Jr., Gillian, R. E., McCleary, S. L., Lotts, C. G., Poole, E. L., Overman, A. L., and Macy, S. C., "CSM Testbed Development and Large-Scale Structural Applications, " NASA TM-4072, 1989.

[18] Vanderplaats, G.N., "ADS — A Fortran Program for Automated Design Synthesis, " Version 1.00, NASA CR–172460, 1984.

[19] Walsh, J.L., "Application of Mathematical Optimization Procedures to a Structural Model of a Large Finite-Element Wing, " NASA TM-87597, 1986.

[20] Whetstone, W.D. "EISI-EAL Engineering Analysis Language Reference Manual — EISI-EAL System Level 2091, " Engineering Information Systems, Inc., 1983.

[21] Vanderplaats, G.N., "CONMIN - A Fortran Program for Constrained Function Minimization: User's Manual, " NASA TM X-62282, 1973.

[22] Camarda, C.J. and Adelman, H.M., "Static and Dynamic Structural-Sensitivity Derivative Calculations in the Finite-Element-Based Engineering Analysis Language (EAL) System, " NASA TM-85743, 1984.

[23] Nagendra, G.K. and Fleury, C., "Sensitivity and Optimization of Composite Structures in MSC/ NASTRAN, " Finite Elements in Analysis and Design, Vol. 5, pp. 223–235, 1989.

[24] Fleury, C. and Braibant, V.,"Structural Optimization — A New Dual Method Using Mixed Variables, " International Journal for Numerical Methods in Engineering, Vol. 23, No. 3, pp. 409–428,1986.

[25] ABAQUS, Hibbitt, Karlsson and Dorensen, Inc., 100 Medway Street, Providence, RI 02906.

[26] Sikiotis, E., Saouma, V., Long. M., and Rogger, W., "Finite Element Based Optimization of Complex Structures on a Cray X–MP Supercomputer, " Computers & Structures, Vol. 36, No. 5, pp. 901–911, 1990.

[27] Gendron, G., "An Optimization System Based on the Finite Element Code CSM Testbed, " Report VPI-E-91-17, Virginia Polytechnic Institute and State University, Blacksburg, Virginia, 1991.

[28] Gürdal, Z. and Haftka, R.T., "Sensitivity Derivatives for Static Loading Boundary Conditions, " AIAA Journal, Vol. 23, No. 1, pp. 159-160, 1985.

[29] Haftka, R.T., Gürdal, Z., and Kamat, M.P., Elements of Structural Optimization, 2nd Revised Edition, Kluwer Academic Publishers, 1990.

[30] Phillips, J.L., "Structural Analysis and Optimum Design of Geodesically Stiffened Composite Panels, " MS Thesis, Virginia Polytechnic Institute and State University, 1990.

[31] Stanley, G.M., "Continuum Based Shell Elements, " PhD Dissertation, Stanford University, Stanford, CA, 1985.

[32] Park, K.C. and Stanley, G.M., "A Curved C^o Shell Element Based on Assumed Natural-Coordinate Strains, " ASME Journal of Applied Mechanics, Vol. 108, pp. 278-290, 1986.

[33] Jones, R.M., Mechanics of Composite Materials, McGraw-Hill Book Co., New-York, 1975.

[34] Hyer, M.W., Loup, D.C., and Starnes, J.H. Jr., "Stiffener/Skin Interactions in Pressure-Loaded Composite Panels, " AIAA Journal, Vol. 28, No. 3, pp. 532-537, 1990.

[35] Ransom, J.B., "Global/Local Stress Analysis of Composite Structures, " MS Thesis, Old Dominion University, 1989.

[36] Thompson, D.M., "Two-Dimensional to Three-Dimensional Global/Local Finite Element Analysis of Laminated Composites in Compression, " MS Thesis, Virginia Polytechnic Institute and State University, 1990.

[37] Vanderplaats, G.N., Yang, Y.J., and Kim, D.S., "Sequential Linearization Method for Multilevel Optimization, " AIAA Journal, Vol. 28, No. 2, pp. 290-295, 1990.

[38] Schmit, L.A. Jr. and Ramanathan, R.K., "Multilevel Approach to Minimum Weight Design Including Buckling Constraints, " AIAA Journal, Vol. 16, No. 2, pp. 97-104, 1978.

[39] Sobieszczanski-Sobieski, J., James, B.B., and Dovi, A.R., "Structural Optimization by Multilevel Decomposition, " AIAA Journal, Vol. 23, No. 11, pp. 1775-1782, 1985.

[40] Stewart, C. B. (Compiler), "The Computational Structural Mechanics Testbed Data Library Description, " NASA TM 100645, October 1988.

Appendix A
Algorithms for the Computation of an Optimal Design.

This appendix presents the flowcharts of the algorithms that are used for the computation of an optimal design. These algorithms have been implemented into CLAMP procedures. A description of each procedure is given in section 3.3.3.

```
Begin
    Set-up an initial design
        Define the finite element model
        Define sublaminates
        Use BDLM to build lamination sequences
        Specify the nodes where the load is applied
        Define the macros indicated in Table 1.1 of Ref. [27]
        Use OPTI to define:
                The design variables
                The constraints
                The objective function
    Execute TB2O to start ADS
    Do while convergence or the maximum number of iterations have
        not been reached
        Restore the value of info
        If info = 1 then
                Compute the value of the constraints
                and the objective function
        Endif
        If info = 2 then
                Compute the derivatives of the constraints and the
                objective function with respect to the design variables
        Endif
        Call the optimizer
    Enddo
End.
```

Fig. A.1 – Procedure `des_ana_iter`.

```
Begin
        If info = 1 then
                Copy from library 2 to library 1
                        The new values of the constraints
                        The updated information concerning the buckling constraints
                        The buckling modes and eigenvalues datasets
                Delete library 2
                Copy information contained in library 1 to library 2[1]
                Call the procedure analysis
                Use OPTI to compute the objective function
                and evaluate the constraints
        Endif
        If info = 2 then
                Call the procedure derivative.
                Use OPTI to calculate the derivatives of the objective function
                and the constraints with respect to the design variables.
        Endif
End.
```

[1]To save disk space, datasets KMAP..nsubs.ksize and AMAP..ic2.isize are not copied.

Fig. A.2 – Procedure `branch_on_info`.

```
Begin
      Rebuild laminate sections (LAM.OMB.nsect1.1 datasets)
      Build the stiffness matrix
      Factor the stiffness matrix
      If displacements are specified
        For each load case
            Compute the static displacements
            Compute the scale factor
      Else (forces are applied)
        Compute the static displacements
      Endif
      If displacements are specified
        Use the superposition principle
        to obtain the static displacements
        corresponding to the complete loading condition
      Endif
      If strain constraints are imposed
        Compute the strains
      Endif
      If buckling constraints are imposed
        Compute and assemble the geometric stiffness matrix
        Compute the eigenvalues, using, if available, the eigenvectors
        obtained at the previous design point as initial trial vectors
      Endif
End
```

Fig. A.3 – Procedure `analysis`.

```
Begin
    Find the sequence number of the dataset containing the design variables
    Transform the value of the design variables into macrosymbols
    Transform the type of the design variables into macrosymbols
    If an exact analysis is required
      Perform an exact analysis
    Endif
    For each design variable x_i
        Compute Δx_i, 1/Δx_i, and -1/Δx_i
        Perturb x_i
        If the design variable is a height (type = 3)
          Execute processor E
        Endif
        Rebuild the lamination sequences
        (Execute processors BDLM and LAU)
        Copy the new constitutive equations to library 1
        Compute and assemble KP, the stiffness matrix corresponding to the
        perturbed design
        If finite difference formulation is used then
          Factor KP
          If loading is applied using nonzero boundary conditions then
            Compute perturbed displacement vector
            corresponding to each load component
            Retrieve the scale factor
            corresponding to each load component
          Else (Loading is applied using nodal forces)
            Compute perturbed displacement vector
          Endif
          Form the total displacement vector
        Else (sensitivity analysis is used)
          Use a finite difference formula to compute dK/dx_i
          If loading is applied using nonzero boundary conditions then
            For each load component
                Compute du/dx_i
                Compute dR/dx_i (see Eq. 3.14)
          Else
            Compute for du/dx_i
          Endif
          Form the total displacement vector
        Endif
```

Fig. A.4 – Procedure `derivative`.

If buckling constraints are imposed
  Compute and assemble KGP, the geometric stiffness matrix
  corresponding to the perturbed design.
  Retrieve eigenvalues corresponding to the current design
  if a finite difference formulation is used then
    Solve the eigenvalue problem
    Compute the derivative of the computed eigenvalues
    with respect to x_i
  Else (sensitivity analysis is used)
    Use a finite difference formula to compute $d\mathbf{K}_G/dx_i$
    Compute the derivative of the computed eigenvalues
    with respect to x_i
  Endif
  Save the derivatives of the computed eigenvalues on a dataset
  If point strain constraints are imposed then
    Compute strains corresponding to the perturbed design
  Endif
  Set the design variable to its original value
  If the design variable is of type 3 (height) then
    Execute processor E
  Endif
  Execute processor OPTI to compute the derivative of the
  constraints with respect to this design variable
End of the loop on the design variables
End.

Fig. A.4 – Concluded.

Appendix B
Design Data for Optimum Cylinder Configurations

Table B.1 – Unstiffened Cylinder Design Data.

a – Skin Laminate = $[-45/+45/90/0]_S$.

	COMPRESSION		TORSION	
	1000 (lb/in)	2700 (lb/in)	418.538 (lb/in)	1000 (lb/in)
x_1 t_0 (in)	0.00759	0.0130	0.0306	0.0415
x_2 t_{90} (in)	0.0303	0.0483	0.0402	0.0623
x_3 $t_{\pm 45}$ (in)	0.0167	0.0278	0.00734	0.0118
Skin Thickness (in)	0.142	0.235	0.171	0.255
Cylinder Weight (lb)	433.3	712.0	519.9	775.7
Buckling	6E-04, 8E-04	1.4E-03, 8E-04	9E-04	0.003
Skin Strength	-0.83	-0.72	-0.86	-0.78

	COMBINED COMPRESSION AND TORSION	
	$N_x = 1000$, $N_{xy} = 1000\ lb/in$	$N_x = 2700$, $N_{xy} = 418.5\ lb/in$
x_1 t_0 (in)	0.0458	0.0392
x_2 t_{90} (in)	0.0627	0.0487
x_3 $t_{\pm 45}$ (in)	0.0172	0.0254
Skin Thickness (in)	0.286	0.277
Cylinder Weight (lb)	869.1	843.7
Buckling	0.002	3E-04
Skin Strength	-0.86	-0.84

$x_i =$ Design Variables
Constraints $g(i)$ are feasible when negative, violated when positive, range: $-1 \leq g(i) < \infty$

b – Skin Laminate = $[-45/+45/90]_S$.

	COMPRESSION
	1000 (lb/in)
x_1 t_{90} (in)	0.0339
x_2 $t_{\pm 45}$ (in)	0.0201
Skin Thickness (in)	0.148
f Cylinder Weight (lb)	451.3
Buckling	4E-04,-0.13
Skin Strength	-0.91

$x_i =$ Design Variables
Constraints $g(i)$ are feasible when negative, violated when positive, range: $-1 \leq g(i) < \infty$

Table B.2 – Geodesically Stiffened Shell Design Data (Compression, Torsion).

a – Skin Laminate = $[-45/+45/90/0]_S$.

	COMPRESSION		TORSION	
	1000 (lb/in)	2700 (lb/in)	418.538 (lb/in)	1000 (lb/in)
2x4				
x_1 t_0 (in)	0.005	0.00887	0.0201	0.0268
x_2 t_{90} (in)	0.0328	0.0522	0.0302	0.0378
x_3 $t_{\pm 45}$ (in)	0.0157	0.0272	0.00741	0.0151
x_4 t_g (in)	0.04†	0.0457	0.0715	0.0982
x_5 h_g (in)	0.4†	0.424	0.999	1.400
Skin Thickness (in)	0.138	0.231	0.130	0.190
Cylinder Weight (lb)	422.8	704.2	404.3	592.9
Stiff. Load Frac. (%)	T‡	T‡	3.7	3.3
Stiff. Weight Frac. (%)	0.4	0.2	2.0	2.6
Buckling	-0.004, 2E-04, -0.003, -0.003 -0.001, -0.004, -0.009	-6E-04, 0.003, 0.004, 0.001, -0.01	7E-04	8E-04, -0.07
Skin Strength	-0.80	-0.68	-0.83	-0.78
Stiff. Strength T	N/A	N/A	-0.96	-0.93
Stiff. Strength C	-0.99	-0.98	-0.96	-0.92
2x8				
x_1 t_0 (in)	0.005†	0.00559	0.0197	0.0265
x_2 t_{90} (in)	0.0329	0.0551	0.0293	0.0408
x_3 $t_{\pm 45}$ (in)	0.0159	0.0271	0.00730	0.0128
x_4 t_g (in)	0.04†	0.0431	0.0838	0.122
x_5 h_g (in)	0.4†	0.432	0.881	1.295
Skin Thickness (in)	0.139	0.230	0.127	0.186
Cylinder Weight (lb)	427.2	702.5	398.4	589.9
Stiff. Load Frac. (%)	0.2	0.1	6.5	7.1
Stiff. Weight Frac. (%)	1.0	0.4	2.9	4.2
Buckling	0.006	8E-04,-9E-04, 1E-03,-0.01, -0.01	6E-04,-0.02, -0.05	7E-04
Skin Strength	-0.80	-0.65	-0.83	-0.75
Stiff. Strength T	N/A	N/A	-0.92	-0.87
Stiff. Strength C	-0.95	-0.92	-0.91	-0.86

† Lower bound.
‡ Stiffeners are in tension.
x_i = Design Variables
Constraints $g(i)$ are feasible when negative, violated when positive, range: $-1 \leq g(i) < \infty$

Table B.2 – Geodesically Stiffened Shell Design Data (Continued).

	COMPRESSION		TORSION	
	1000 (lb/in)	2700 (lb/in)	418.538 (lb/in)	1000 (lb/in)
2x16				
x_1 t_0 (in)	0.005†	0.005†	0.0117	0.0162
x_2 t_{90} (in)	0.0360	0.0557	0.0315	0.0474
x_3 $t_{\pm 45}$ (in)	0.0124	0.0238	0.00505	0.005†
x_4 t_g (in)	0.100	0.113	0.0991	0.146
x_5 h_g (in)	1.238	1.223	1.28	1.682
Skin Thickness (in)	0.131	0.217	0.1065	0.147
Cylinder Weight (lb)	427.5	690.1	352.4	502.0
Stiff. Load Frac. (%)	8.8	7.4	17.2	24.5
Stiff. Weight Frac. (%)	6.3	4.5	8.0	10.7
Buckling	0.004	9E-04,-0.08, -0.04	8E-04	8E-04
Skin Strength	-0.80	-0.69	-0.81	-0.66
Stiff. Strength T	N/A	N/A	-0.89	-0.81
Stiff. Strength C	-0.90	-0.79	-0.88	-0.79
2x24				
x_1 t_0 (in)	0.005†	0.005†	0.0105	0.0205
x_2 t_{90} (in)	0.0298	0.0483	0.0271	0.0366
x_3 $t_{\pm 45}$ (in)	0.00822	0.0102	0.005	0.00501
x_4 t_g (in)	0.180	0.296	0.0732	0.117
x_5 h_g (in)	1.64	1.85	1.35	1.447
Skin Thickness (in)	0.102	0.147	0.0952	0.134
Cylinder Weight (lb)	400.0	611.6	319.4	458.9
Stiff. Load Frac. (%)	39	50.7	9.5	17.8
Stiff. Weight Frac. (%)	22	26.7	9.3	11.0
Buckling	8E-04,-7E-03, -0.02,-0.01, -0.03,-0.03	8E-04, -0.074	9E-04	3E-04
Skin Strength	-0.83	-0.70	-0.80	-0.62
Stiff. Strength T	N/A	N/A	-0.91	-0.83
Stiff. Strength C	-0.88	-0.78	-0.90	-0.80

† Lower bound.
x_i = Design Variables
Constraints $g(i)$ are feasible when negative, violated when positive, range: $-1 \leq g(i) < \infty$

Table B.2 – Geodesically Stiffened Shell Design Data (Continued).

	COMPRESSION		TORSION	
	1000 (lb/in)	2700 (lb/in)	418.538 (lb/in)	1000 (lb/in)
2x32				
x_1 t_0 (in)	0.005†	0.005†	0.00929	0.0126
x_2 t_{90} (in)	0.0245	0.0357	0.0243	0.0339
x_3 $t_{\pm 45}$ (in)	0.00599	0.0120	0.005†	0.005†
x_4 t_g (in)	0.213	0.267	0.0607	0.106
x_5 h_g (in)	1.32	1.54	1.34	1.68
Skin Thickness (in)	0.0779	0.130	0.0874	0.1130
Cylinder Weight (lb)	360.2	552.8	298.2	412.3
Stiff. Load Frac. (%)	53	57.6	14.8	21.1
Stiff. Weight Frac. (%)	30	28.6	10.8	16.7
Buckling	0.001, -0.06	9E-04	8E-4, -3E-4, 7E-4, -0.17, -0.007	3E-4, 0.001, -3E-4, -0.002, -0.002, -0.01
Skin Strength	-0.85	-0.74	-0.78	-0.58
Stiff. Strength T	N/A	N/A	-0.92	-0.85
Stiff. Strength C	-0.88	-0.78	-0.91	-0.83
2x48				
x_1 t_0 (in)	0.005†	0.005†		
x_2 t_{90} (in)	0.0143	0.0266		
x_3 $t_{\pm 45}$ (in)	0.00943	0.0135		
x_4 t_g (in)	0.158	0.180		
x_5 h_g (in)	1.093	1.261		
Skin Thickness (in)	0.0762	0.117		
Cylinder Weight (lb)	328.9	484.4		
Stiff. Load Frac. (%)	52	53		
Stiff. Weight Frac. (%)	29	26		
Buckling	7E-04,-0.03, -0.04,-0.05, -0.05	8E-04, -0.06		
Skin Strength	-0.87	-0.73		
Stiff. Strength T	N/A	N/A		
Stiff. Strength C	-0.88	-0.74		

† Lower bound.
$x_i =$ Design Variables
Constraints $g(i)$ are feasible when negative, violated when positive, range: $-1 \leq g(i) < \infty$

Table B.2 – Geodesically Stiffened Shell Design Data (Continued).

	COMPRESSION
	2700 (lb/in)
4x48	
x_1 t_0 (in)	0.005†
x_2 t_{90} (in)	0.0329
x_3 $t_{\pm 45}$ (in)	0.0133
x_4 t_g (in)	0.177
x_5 h_g (in)	0.974
Skin Thickness (in)	0.129
Cylinder Weight (lb)	495.3
Stiff. Load Frac. (%)	39.0
Stiff. Weight Frac. (%)	21.0
Buckling	7E-04
Skin Strength	-0.65
Stiff. Strength	-0.73
8x48	
x_1 t_0 (in)	0.005†
x_2 t_{90} (in)	0.0465
x_3 $t_{\pm 45}$ (in)	0.0126
x_4 t_g (in)	0.1436
x_5 h_g (in)	0.735
Skin Thickness (in)	0.154
Cylinder Weight (lb)	544.1
Stiff. Load Frac. (%)	15.0
Stiff. Weight Frac. (%)	14.0
Buckling	9E-04
Skin Strength	-0.54
Stiff. Strength	-0.77

† Lower bound.
x_i = Design Variables
Constraints $g(i)$ are feasible when negative, violated when positive, range: $-1 \leq g(i) < \infty$

Table B.2 – Geodesically Stiffened Shell Design Data (Continued).

	TORSION
	418.538 (lb/in)
3x24	
x_1 t_0 (in)	0.00642
x_2 t_{90} (in)	0.0296
x_3 $t_{\pm 45}$ (in)	0.005†
x_4 t_g (in)	0.0969
x_5 h_g (in)	0.886
Skin Thickness (in)	0.0920
Cylinder Weight (lb)	309.3
Stiff. Load Frac. (%)	19.4
Stiff. Weight Frac. (%)	9.4
Buckling	0.002
Skin Strength	-0.80
Stiff. Strength Tension	-0.89
Stiff. Strength Comp.	-0.87
4x24	
x_1 t_0 (in)	0.0837
x_2 t_{90} (in)	0.0272
x_3 $t_{\pm 45}$ (in)	0.005†
x_4 t_g (in)	0.0734
x_5 h_g (in)	0.876
Skin Thickness (in)	0.0912
Cylinder Weight (lb)	301.5
Stiff. Load Frac. (%)	18.8
Stiff. Weight Frac. (%)	7.9
Buckling	-0.001, -0.15
Skin Strength	-0.80
Stiff. Strength Tension	-0.88
Stiff. Strength Comp.	-0.86

† Lower bound.
x_i = Design Variables
Constraints $g(i)$ are feasible when negative, violated when positive, range: $-1 \leq g(i) < \infty$

Table B.2 – Geodesically Stiffened Shell Design Data (Continued).

	COMPRESSION
	2700 (lb/in)
1x12	
x_1 t_0 (in)	0.005†
x_2 t_{90} (in)	0.0486
x_3 $t_{\pm 45}$ (in)	0.0167
x_4 t_g (in)	0.355
x_5 h_g (in)	1.87
Skin Thickness (in)	0.174
Cylinder Weight (lb)	628.7
Stiff. Load Frac. (%)	29.5
Stiff. Weight Frac. (%)	15.8
Buckling	9E-4, -0.06
Skin Strength	-0.67
Stiff. Strength Comp.	-0.78
3x36	
x_1 t_0 (in)	0.005†
x_2 t_{90} (in)	0.0386
x_3 $t_{\pm 45}$ (in)	0.0144
x_4 t_g (in)	0.235
x_5 h_g (in)	1.07
Skin Thickness (in)	0.145
Cylinder Weight (lb)	554.0
Stiff. Load Frac. (%)	39.9
Stiff. Weight Frac. (%)	20.3
Buckling	-9E-4, -0.004, -0.006, -0.01, -0.04, -0.04
Skin Strength	-0.69
Stiff. Strength Comp.	-0.75

† Lower bound.
x_i = Design Variables
Constraints $g(i)$ are feasible when negative, violated when positive, range: $-1 \leq g(i) < \infty$

Table B.2 – Geodesically Stiffened Shell Design Data (Continued).

b – Skin Laminate = $[-45/+45/90]_S$.

	COMPRESSION
	1000 (lb/in)
2x48	
x_1 t_{90} (in)	0.0145
x_2 $t_{\pm 45}$ (in)	0.005†
x_3 t_g (in)	0.191
x_4 h_g (in)	1.09
Skin Thickness (in)	0.049
Cylinder Weight (lb)	266.2
Stiff. Load Frac. (%)	69.0
Stiff. Weight Frac. (%)	44.0
Buckling	8E-04
Skin Strength	-0.92
Stiff. Strength	-0.85

c – Skin Laminate = $[90]_T$.

	COMPRESSION
	1000 (lb/in)
2x48	
x_1 t_{90} (in)	0.0176
x_2 t_g (in)	0.303
x_3 h_g (in)	0.860
Skin Thickness (in)	0.035
Cylinder Weight (lb)	252.8
Stiff. Load Frac. (%)	89.0
Stiff. Weight Frac. (%)	57.7
Buckling	3E-04, -0.007
Skin Strength	-0.97
Stiff. Strength	-0.89

† Lower bound.
x_i = Design Variables
Constraints $g(i)$ are feasible when negative, violated when positive, range: $-1 \leq g(i) < \infty$

Table B.2 – Geodesically Stiffened Shell Design Data (Continued).

d – Skin Laminate = $[90/0]_S$.

	TORSION
	1000 (lb/in)
2x32	
x_1 t_0 (in)	0.0158
x_2 t_{90} (in)	0.0325
x_3 t_g (in)	0.162
x_4 h_g (in)	1.47
Skin Thickness (in)	0.0967
Cylinder Weight (lb)	384.1
Stiff. Load Frac. (%)	43.1
Stiff. Weight Frac. (%)	23.4
Buckling	6E-4, 6E-4, -0.015
Skin Strength	-0.70
Stiff. Strength Tension	-0.76
Stiff. Strength Comp.	-0.73

x_i = Design Variables
Constraints $g(i)$ are feasible when negative, violated when positive, range: $-1 \leq g(i) < \infty$

Table B.2 – Geodesically Stiffened Shell Design Data (Continued).

e – 24x12x1 Mesh.

	COMPRESSION	
	$N_x = 1000$	$N_x = 2700$
2x24		
x_1 t_0 (in)	0.005†	0.005†
x_2 t_{90} (in)	0.0301	0.0494
x_3 $t_{\pm 45}$ (in)	0.0100	0.0116
x_4 t_g (in)	0.160	0.291
x_5 h_g (in)	1.43	1.68
Skin Thickness (in)	0.110	0.155
Cylinder Weight (lb)	404.1	618.1
Stiff. Load Frac.(%)		
Stiff. Weight Frac. (%)	16.7	23.6
Buckling	5E-4, -3E-4, -0.02, -0.05	6E-04, -0.01, -0.03, -0.03 -0.04
Skin Strength		
Stiff. Strength T		
Stiff. Strength C		
2x48		
x_1 t_0 (in)	0.005†	0.005†
x_2 t_{90} (in)	0.0178	0.0278
x_3 $t_{\pm 45}$ (in)	0.0105	0.0142
x_4 t_g (in)	0.140	0.183
x_5 h_g (in)	0.906	1.27
Skin Thickness (in)	0.0875	0.122
Cylinder Weight (lb)	337.2	502.8
Stiff. Load Frac. (%)		
Stiff. Weight Frac. (%)	21.0	25.9
Buckling	9E-4, -7E-4, -0.04	7E-04, -0.02, -0.08, -0.09, -0.09, -0.1
Skin Strength		-0.70
Stiff. Strength T		-0.83
Stiff. Strength C		-0.73

† Lower bound.
x_i = Design Variables
Constraints $g(i)$ are feasible when negative, violated when positive, range: $-1 \leq g(i) < \infty$

Table B.3 – Geodesically Stiffened Shell Design Data Combined Compression and Torsion.

	COMBINED COMPRESSION AND TORSION	
	$N_x = 1000$, $N_{xy} = 1000\ lb/in$	$N_x = 2700$, $N_{xy} = 418.5\ lb/in$
2x8		
$x_1\ t_0\ (in)$	0.0251	0.00935
$x_2\ t_{90}\ (in)$	0.0478	0.0581
$x_3\ t_{\pm 45}\ (in)$	0.0188	0.0288
$x_4\ t_g\ (in)$	0.122	0.0651
$x_5\ h_g\ (in)$	1.48	1.24
Skin Thickness (in)	0.221	0.250
Cylinder Weight (lb)	699.5	773.3
Stiff. Load Frac. Tors. (%)	7.2	3.8
Stiff. Load Frac. Comp. (%)	0.8	0.5
Stiff. Weight Frac. (%)	3.9	1.5
Buckling	9E-4, -0.02	-8E-04, 1E-3, -0.01, -0.03
Skin Strength	-0.84	-0.70
Stiff. Strength T	-0.92	-0.97
Stiff. Strength C	-0.87	-0.90
2x24		
$x_1\ t_0\ (in)$	0.00501	0.005†
$x_2\ t_{90}\ (in)$	0.0596	0.0526
$x_3\ t_{\pm 45}\ (in)$	0.00651	0.00787
$x_4\ t_g\ (in)$	0.155	0.312
$x_5\ h_g\ (in)$	1.50	1.73
Skin Thickness (in)	0.142	0.147
Cylinder Weight (lb)	542.4	605.2
Stiff. Load Frac. Tors. (%)	26.1	37.5
Stiff. Load Frac. Comp. (%)	40.0	31.6
Stiff. Weight Frac. (%)	20.2	26.2
Buckling	0.001, -0.01	8E-04, -0.08
Skin Strength	-0.71	-0.70
Stiff. Strength T	-0.96	-0.83
Stiff. Strength C	-0.72	-0.73

† Lower bound.
$x_i =$ Design Variables
Constraints $g(i)$ are feasible when negative, violated when positive, range: $-1 \leq g(i) < \infty$

Table B.4 – Geodesically Stiffened Shell Design Data Other Designs Obtained in Torsion.

	TORSION
	418.5 (lb/in)
2x4	
x_1 t_0 (in)	0.0206
x_2 t_{90} (in)	0.0285
x_3 $t_{\pm 45}$ (in)	0.00716
x_4 t_g (in)	0.146
x_5 h_g (in)	1.063
Skin Thickness (in)	0.127
Cylinder Weight (lb)	404.8
Stiff. Load Frac. (%)	6.2
Stiff. Weight Frac. (%)	4.6
Buckling	7E-04
Skin Strength	-0.83
Stiff. Strength T	-0.96
Stiff. Strength C	-0.96
2x8	
x_1 t_0 (in)	0.0182
x_2 t_{90} (in)	0.0273
x_3 $t_{\pm 45}$ (in)	0.005†
x_4 t_g (in)	0.180
x_5 h_g (in)	2.37
Skin Thickness (in)	0.111
Cylinder Weight (lb)	401.4
Stiff. Load Frac. (%)	14.6
Stiff. Weight Frac. (%)	115.8
Buckling	0.003
Skin Strength	-0.83
Stiff. Strength T	-0.87
Stiff. Strength C	-0.86

† Lower bound.
x_i = Design Variables
Constraints $g(i)$ are feasible when negative, violated when positive, range: $-1 \leq g(i) < \infty$

Table B.4 – Geodesically Stiffened Shell Design Data Other Designs Obtained in Torsion (Continued).

	TORSION
	418.5 (lb/in)
2x16	
x_1 t_0 (in)	0.0107
x_2 t_{90} (in)	0.0272
x_3 $t_{\pm 45}$ (in)	0.00502
x_4 t_g (in)	0.150
x_5 h_g (in)	1.95
Skin Thickness (in)	0.0958
Cylinder Weight (lb)	355.4
Stiff. Load Frac. (%)	35.9
Stiff. Weight Frac. (%)	27.3
Buckling	8E-04
Skin Strength	-0.84
Stiff. Strength T	-0.91
Stiff. Strength C	-0.90

$x_i =$ Design Variables
Constraints $g(i)$ are feasible when negative, violated when positive, range: $-1 \leq g(i) < \infty$

Table B.5 – Conventionally Stiffened Shell,(Compression and Torsion).

	COMPRESSION		TORSION	
	1000 (lb/in)	2700 (lb/in)	418.5 (lb/in)	1000 (lb/in)
2x8				
x_1 t_0 (in)	0.005†	0.005†	0.0164	0.0236
x_2 t_{90} (in)	0.0258	0.0424	0.0304	0.0442
x_3 $t_{\pm 45}$ (in)	0.00767	0.00976	0.00516	0.00821
x_4 t_s (in)	0.479	0.655	0.176	0.0959
x_5 h_s (in)	2.11	2.87	2.49	5.00
x_6 t_r (in)	0.04†	0.0575	0.0922	0.0951
x_7 h_r (in)	0.4†	0.592	1.20	1.4537
Skin Thickness (in)	0.0922	0.134	0.114	0.169
Cylinder Weight (lb)	373.9	580.9	392.3	563.0
Stiff. Load Frac. (%)	55.7	65.5	N/A	N/A
Stringer Weight Frac. (%)	24.7	29.5	10.2	7.9
Ring Weight Frac. (%)	0.2	0.3	1.0	0.9
Buckling	-0.002, 8E-4, -3E-4, -0.003, -0.009	-8E-4, 9E-4, 7E-4, -0.009, -0.01, -0.015	4E-4, -0.002, -0.06, -0.23	-0.005, -0.002, 0.02, -1.9
Skin Strength	-0.87	-0.79	-0.79	
Stringer Strength	-0.88	-0.79		
2x24 and 2x32	2x32	2x24	2x32	
x_1 t_0 (in)	0.005†	0.005†	0.00934	
x_2 t_{90} (in)	0.0170	0.0325	0.0190	
x_3 $t_{\pm 45}$ (in)	0.00899	0.0119	0.005†	
x_4 t_s (in)	0.228	0.402	0.08†	
x_5 h_s (in)	1.06	1.43	2.30	
x_6 t_r (in)	0.04†	0.0725	0.0843	
x_7 h_r (in)	0.4†	0.882	1.13	
Skin Thickness (in)	0.0799	0.123	0.0767	
Cylinder Weight (lb)	332.3	532.6	304.3	
Stiff. Load Frac. (%)	53.5	62.3	N/A	
Stringer Weight Frac. (%)	29.4	27.5	22.0	
Ring Weight Frac. (%)	0.2	0.5	1.3	
Buckling	-0.003, -8E-4, -0.001, -0.001, -0.002, -0.004, -0.007	-0.003, -0.001, 7E-4, 0.001, -0.003, -0.01, -0.01	-1E-4, -0.03, -0.05 -0.06 -0.1	
Skin Strength	-0.87	-0.78	-0.74	
Stringer Strength	-0.87	-0.78	N/A	

Table B.5 – Conventionally Stiffened Shell, (Continued).

	TORSION
	418.5 (lb/in)
4x8	
x_1 t_0 (in)	0.0115
x_2 t_{90} (in)	0.0243
x_3 $t_{\pm 45}$ (in)	0.00852
x_4 t_s (in)	0.08†
x_5 h_s (in)	2.00
x_6 t_r (in)	0.0674
x_7 h_r (in)	0.925
Skin Thickness (in)	0.0958
Cylinder Weight (lb)	343.7
Stiff. Load Frac. (%)	N/A
Stringer Weight Frac. (%)	4.2
Ring Weight Frac. (%)	2.2
Buckling	-0.003, 0.001, -9E-4, -0.005, -0.02, -0.02
Skin Strength	-0.84

† Lower bound.
x_i = Design Variables
Constraints $g(i)$ are feasible when negative, violated when positive, range: $-1 \leq g(i) < \infty$

Table B.6 – Conventionally Stiffened Shell Design Data Combined Compression and Torsion.

	COMBINED COMPRESSION AND TORSION	
	$N_x = 1000$, $N_{xy} = 1000\ lb/in$	$N_x = 2700$, $N_{xy} = 418.5\ lb/in$
2x8		
$x_1\ t_0\ (in)$	0.0300	0.00500
$x_2\ t_{90}\ (in)$	0.0520	0.0590
$x_3\ t_{\pm 45}\ (in)$	0.0110	0.00881
$x_4\ t_g\ (in)$	0.151	0.733
$x_5\ h_g\ (in)$	3.26	2.57
$x_6\ t_r\ (in)$	0.114	0.0611
$x_7\ h_r\ (in)$	1.18	0.710
Skin Thickness (in)	0.208	0.163
Cylinder Weight (lb)	684.1	671.4
Stringer Load Frac. Comp. (%)	15.4	64.1
Stringer Weight Frac. (%)	6.6	25.6
Ring Weight Frac. (%)	1.0	0.4
Buckling	0.001,	-0.003,
	0.001	0.001,
	-0.01	6E-4,
	-0.02	4E-4
		-0.002
		-0.007
		-0.02
Skin Strength	-0.79	-0.79
Stiff. Strength C	-0.93	-0.79

x_i = Design Variables
Constraints $g(i)$ are feasible when negative, violated when positive, range: $-1 \leq g(i) < \infty$

Appendix C
Organization of the Data Base in the Context of Global/Local Analysis and Design

The modifications made to TBOP to accomodate a global/local analysis strategy are described in this appendix. Although the implementation of these new capabilities share several subroutines with TBOP, it is run as a separate program called TBOPGL. The additional information required for the implementation of the new capabilities is stored in different libraries that contain either new datasets or datasets that have already been documented in Refs. [27,40]. Consequently, only the new libraries and datasets are described in this Appendix. This description is followed by a discussion of the new processors that have been developed.

C.1 New Libraries and New Datasets

The organization of the libraries is shown in Fig. C.1. As indicated in this figure, the database now includes a master library and several sets of two libraries. Each set contains the information concerning either a model or an interpolation region. In this figure, the generic name for the file that contains the data base is "EX". This is the only part of the filenames that can changed. For example, if "EX" is changed for "TEST", then TBOPGL will expect the data concerning the global model to be in libraries named "TEST1.L01" and "TEST1.L02". Note that the filenames of the libraries must be in capital letters. Among all the libraries required by TBOPGL, the ones that contain the information concerning the interpolation regions are those that require the most input from the user. All the other libraries are either identical to those required by TBOP or automatically set up by TBOPGL.

The master library shown at the top of Fig. C.1 contains the information related

to the optimization problem. The datasets stored in this library are listed in Table C.1. As indicated in this table, the datasets that define the design variables, the constraints, the objective functions, as well as the values of the constraints and their gradients are all stored in the master library. Moreover, this library also contains the information concerning the coordination work that must be performed between the global and local models following a move in the design space. It is important to remember that this is the only library from which TB2O reads data before calling the optimization program.

The data concerning the finite element analysis and the optimization problem of each model, being global or local, are defined using 2 libraries. As already explained in Ref. [27], the reason for using two libraries is to avoid using the *PACK directive to delete the information that has become obsolete following a move in the design space. Except for few datasets that are automatically installed by TBOPGL, this library contains the same datasets that are contained in the two libraries used by TBOP to define the finite element model and the optimization problem.

Finally, each local model has several sets of two libraries associated with it. They contain the information necessary for the interpolation of the static displacement fields from the global model to the local model. The reason for using several sets of two libraries, rather than only one set, is to allow TBOPGL to design models that contain several interpolation regions which necessitate the utilization of as many spline matrices. For example, consider the design of a stiffened panel where one of the skin-stiffener intersections must be studied using a local model. In this case, the skin and the stiffener contained in the local model are defined using separate interpolation regions. The interpolation of the displacement fields must be performed for each interpolation region and each of these sets of libraries contains all the information required for these calculations. The library whose name ends with "C.L01" contains the information concerning the coarse mesh that discretizes the interpolation region and the library whose name ends

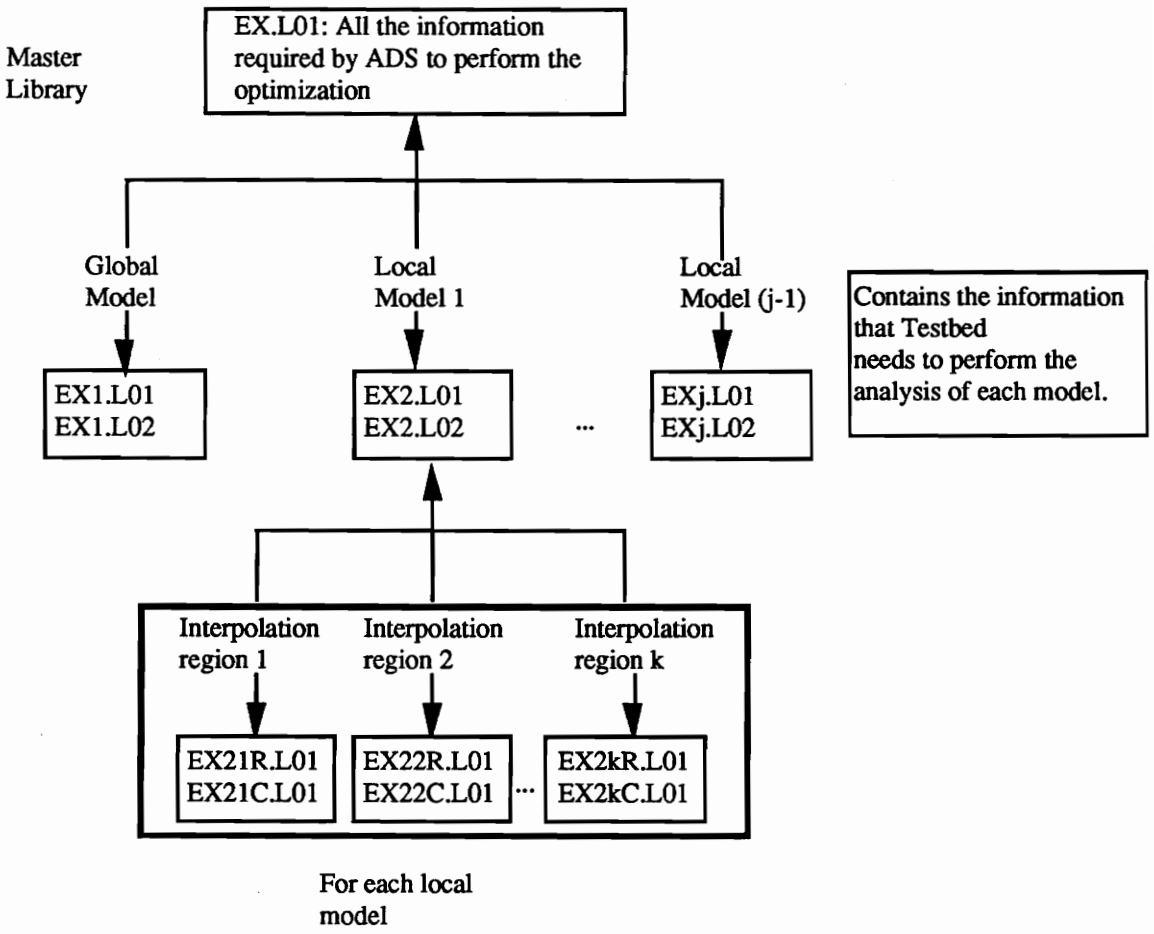

Fig. C.1 – Organization of the Libraries.

with "R.L01" contains the information concerning the refined mesh that discretizes the same region. The datasets contained in each library are listed in Tables C.2 and C.3. In these tables, the datasets indicated as input datasets must be provided by the user. Also, the dimensions of several datasets are indicated at the end of the description of their content.

C.2 New Processors

The implementation of the global/local analysis and design procedure has also required the development of two new processors. The first new processor developed is called MISC. This processor realizes two different operations. The first operation consists of extracting, from a nodal solution vector corresponding to the global model, the components associated with a specific interpolation region. This operation is required twice for every design iteration. It must first be performed after the exact analysis of the global model to extract, from the static displacement solution, the components corresponding to the nodes belonging to each interpolation region. Each of these vectors is then processed by INTS [16], the processor in charge of computing the spline interpolation required to the generation of refined displacement fields. The same operation must also be performed during the computation of the constraint derivatives with respect to the design variables. For each design variable, the static displacements corresponding to a perturbed design must be extracted from the global nodal solution and separate nodal vectors must be created for each interpolation region. This is required for the calculation of the term $-\mathbf{K}_{1,1}\frac{d\mathbf{u}_{1c}}{dx_i}$ in Eq. 6.4.

The second operation realized by the processor MISC consists of forming nonzero boundary condition vectors for each local model. This operation follows the extraction operation described above. It consists of assembling the total vector of nonzero boundary conditions for each local model. This is accomplished by reading the refined vectors of

boundary conditions generated by INTS for each interpolation region.

The second new processor is called CRDN. CRDN sets up and realizes the coordination work that must be performed between the different models following a move in the design space. It is first called to set up the coordination work. This initial step consists of specifying what characteristics of a model must be updated when the value of a design variable defined in another model is changed. Secondly, CRDN is also called by the procedure `des_ana_iter` to realize the coordination work. This call occurs immediately after a new design point has been computed by the optimizer.

The global/local analysis and design strategy has also been built using CLAMP procedures. Two of these procedures implement the iterative scheme required for the calculation of an optimal design. Two others perform the calculation of the quantities required for the computation of the constraints and their derivatives. The same procedures already described in Chapter 3 and in Ref. 27 are used here. Only minor changes have been made to accomodate multiple models and compute the term $-\mathbf{K}_{1,1}\frac{d\mathbf{u}_{1c}}{dx_i}$ of Eq. 6.4. These procedures will consequently not be discussed here.

An example of a runstream that can be used to perform the global/local analysis and design of a structural model is shown in Fig. C.2. The runstream corresponds to the example presented in Section 6.3.1. In-line documentation that details the steps that are performed by each block of commands have been added to the runstream.

Table C.1 – Datasets Stored in Master Library.

Dataset Name	Content
ADS.RTN.1.1	Variable `info` returned by ADS
ADS.PMTR.1.1	Tables wk and iwk returned by ADS
OBJ.FCN.*im*.1	Definition of the objective function for model *im*
DESN.VARS.*im*.1	Definition of the design variables for model *im*
BUCK.CONS.*im*.1	Definition of the buckling constraints imposed on model *im*
BCON.EVAL.*im*.1	Values of the buckling constraints and gradients of the computed eigenvalues for model *im*
DISP.CONS.*im*.1	Definition of the displacement constraints imposed on model *im*
DCON.EVAL.*im*.1	Values and gradients of the displacement constraints for model *im*
PSTR.CONS.*im*.1	Definition of the point strain constraints imposed on model *im*
PCON.EVAL.*im*.1	Values and gradients of the point strain constraints for model *im*
COOR.DINA.*from_model.to_model*	Definition of the coordination work that must be performed between model *from_model* and model *to_model*

Table C.2 – Datasets Corresponding to the Coarse Mesh for Each Interpolation Region (...C.L01).

Dataset Name	Content
JLOC.BTAB.2.5 (input)	The coordinates of the nodes mapped onto a 2D plane surface. Node 1 is located at the origin of the coordinate frame (nncs†x3).
ALTR.BTAB.2.4	The orientation of the reference frame with respect to the global reference frame‡
GLOB.NODE.1.1 (input)	Node numbers in the global model (nncs)
SPLI.*.1	All the datasets generated by the processor SPLN
STAT.DISP.1.1	Static displacements of the nodes contained in this interpolation region extracted from the static response computed with the global model (nncsx6).
APPL.MOTI.8.idv	where idv represents the design variable number. Static displacements of the nodes contained in this interpolation region extracted from the static response computed with the global model and corresponding to a configuration where the idv design variable has been perturbed (nncsx6).

†nncs represents the number of nodes in the coarse mesh discretizing the interpolation region. Similarly, nnrs represents the number of nodes in the refined mesh discretizing the interpolation region.

‡ This dataset is not actually used. The processors SPLN and INTS check for the occurrence of this dataset in the library but, in our case, the information that it contains is not actually read.

Table C.3 – Datasets Corresponding to the Refined Mesh for Each Interpolation Region (...R.L01).

Dataset Name	Content
JLOC.BTAB.2.5 (input)	The coordinates of the nodes mapped onto a 2D plane surface. Node 1 is located at the origin of the coordinate frame (nnrsx3).
BOUN.NODE.1.1 (input)	Nodes located on the boundary of the local model. The node numbers correspond to the numbering used in the local model. This information is used to build the applied motion dataset for the local model (number of nodes on the boundary of the interpolation region).
LOCA.NODE.1.1 (input)	Nodes located on the boundary of the local model. The node numbers correspond to the numbering used in the interpolation region. This information is used to build the applied motion dataset for the local model (number of nodes on the boundary of the interpolation region).
JDF1.BTAB.1.8	Number of nodes contained in the interpolation region and the number of degrees of freedom at each node. This information is used to build the applied motion dataset for the local model
APPL.MOTI.1.1	Boundary conditions that must be applied at the boundary of the interpolation region. This dataset is used to form the applied motion dataset for the local model (nnrsx6).
APPL.MOTI.9.idv	where idv represents the design variable number. Refined static displacement field for this interpolation region The original displacement field corresponds to the the static response computed with the global model and corresponding to a configuration where the idv design variable has been perturbed (nnrsx6).

```
cd /scr/gendron
cp /csm/prc/proclib.gal proclib.aug
chmod u+w proclib.aug
/bin/time testbed << \*EOI*
*set echo off
.
.  Assume only 1 library procedure is used.
.  all the procedures must have different names!!!
.
*open 28 proclib.aug
.
*open 1 EX3.L01 /new .  Must use capital letters for
.    all library names
.  This is the master library, it contains:
.                  Design variables
.                  Constraints
.                  ADS parameters
.                  Coordination
*set plib = 28
*define/a filename='EX3' .  Capital letters
.  The following information is model independent
.    .
*add '/usr/u1/gendron/expe/branch_on_info.prc'
*add '/usr/u1/gendron/expe/des_ana_iter.prc'
*add '/usr/u1/gendron/expe/analysis.prc'
*add '/usr/u1/gendron/expe/derivative.prc'
.
*def/i numb_models = 2 .  number of local models is assumed
.    to be = to numb_models - 1.
*define/i nosm[1:2] == 0,1 .  An array that indicates the
.        Number Of SubModels
.        associated with each local model.
.        Dimension:  number of models
.        First component goes with the global model
.        which does not have any
.        submodels associated with it
.        (Consequently, first component always 0)
.
.  Assume library names are <filename>//<im>.101
.  and <filename>//<im>.102,
.  where <filename>//<im>.101 and
.  <filename>//<im>.102 contain the
.  information regarding model <im>
*add '/usr/u1/gendron/expe/pwholeg.data'
*add '/usr/u1/gendron/expe/pwholel.data'
.
*define/a filename='EX3' .  Capital letters
*define/i maxiter=10
```

Fig. C.2 – Runstream Used for Global/Local Analysis and Design.

```
.
.  Control of ADS
.
*def/i strat=9      .  Strategy number
*def/i opt=5        .  Optimization algorithm
*def/i oned=7       .  1D search algorithm
*def/i print=3552   .  Printing index
*def/i ndv=0        .  Temporarily (Computed by DDVR)
*def/i ncon=0       .  Temporarily (Computed by TB20)
.
*put 1 ADS.RTN.1.1  !  Capital letters
*put 1 'ADS.PMTR.1.1'
*find dataset 1 ADS.PMTR.1.1 /seq=es_idss
.
*m2g /name==ndv     /type=i   1 <es_idss> PARAM.1
*m2g /name==ncon    /type=i   1 <es_idss> PARAM.2
*m2g /name==strat   /type=i   1 <es_idss> PARAM.3
*m2g /name==opt     /type=i   1 <es_idss> PARAM.4
*m2g /name==oned    /type=i   1 <es_idss> PARAM.5
*m2g /name==print   /type=i   1 <es_idss> PARAM.6
.
.  libraries containing the information regarding model 1
.
.  The following information is model dependent
.
*close 1
*open 1 EX31.L01 /new
*open 2 EX31.L02 /new
.
*define/f load_u[1]=0.0
*define/f load_v[1]=10000.0e+00
*define/f load_w[1]==0.0e+00
*define/i set_u[1]==0
*define/i set_v[1]==1
*define/i set_w[1]==0
*define/i fin_diff[1]==0
*define/i ntel[1]== 1
*define/i nsubl[1]==1
*def/i imp_disp[1]==1
.
[xqt opti
load_ratio
initialize ldi=1 nodes=175,316:325:1
end
stop
.
```

Fig. C.2 – (Cont'd).

```
[xqt tab
*call MESH_JLOCG
*call BNDYG
[xqt AUS
TABLE(NI=16,nj=1):  OMB DATA 1 1  .  Table of mat.  prop.
I=1,2,3,4,5,6,7,8,9,10,11,12,13,14,15
J=1:  10.0e+06 0.3 10.0e+06 3.8462e+06 3.8462e+06  >
3.8462e+06 .0 .0 1.55e-05 >
.01330 .01270 0.01355 0.01184 0.003386 0.01355
.
TABLE (NI=3,NJ=1,itype=0):  SUB LAM 1 1
J = 1 :  1 0.10 0.0
.
*open 3 EX321G.L01
[xqt dcu
copy 1 3 JLOC BTAB 2 5
stop
*close 3
[xqt bdlm
*put 1 BLD.LAM.1.1
build=1 using=1
stop
[xqt LAU
*call MESH_CONG
*call ES ( function = 'DEFINE FREEDOMS'; --
es_proc = <es_proc>; --
es_name = <es_name[1]>; --
es_pars = <es_pars[1]> )
[xqt E
[xqt RSEQ
reset maxcon=75
[xqt TOPO
reset maxsub = 60000
reset lramap = 9000
[xqt AUS
sysvec:  appl motion 1 1
*call MOTIONG
```

Fig. C.2 – (Cont'd).

```
.
[xqt OPTI
ddvr
.
.      Defining design variables
.
dv=1 thickness  sectionnumber=1  plynumber=1 --
in= 0.01,5.0
save THIRD_WORD=1
end
.
.      Define the constraints
.
constraint
define buckling=1 eval=1 value=1.0
save THIRD_WORD=1
end
objective
define weight rho=0.057 third_word=1
end
stop
.
.  don't need kmap and amap in library 2
*delete 1 KMAP..*.*
*delete 1 AMAP..*.*
.
[xqt DCU
copy 1 2
stop
*enable 1 KMAP..*.*
*enable 1 AMAP..*.*
*open 2 EX321C.L01
[xqt dcu
copy 1 2 ALTR BTAB 2 4
[xqt SPLN
RESET INLIB=2
RESET SLIB=2
RESET DEGREE=1
```

Fig. C.2 – (Cont'd).

```
.
.  Setting up the spline interpolation
.
SURF 1 XLOC=1, YLOC=2, SYM=0
INPUT
BOUN 1
0.0,0.0,0.0      10.0,20.0,0.0
stop
*close 2
.  Need to copy the definition of the
.  optimization problem in master library
*open 3 EX3.L01   .  This is the master library
[xqt DCU
copy 1 3 DESN VARS 1 1
copy 1 3 BUCK CONS 1 1
copy 1 3 BCON EVAL 1 1
copy 1 3 OBJ  FCN 1 1
stop
.
.  Need to close the libraries
.  corresponding to model 1
*close 1
.
.  and open the library
.  corresponding to model 2.
.
*open 1 EX32.L01 /new
*open 2 EX32.L02 /new
.
*def/i imp_disp[2]==1
*define/i set_u[2]==1
*define/i set_v[2]==0
*define/i set_w[2]==0
*define/e load_u[2]==0.0
*define/e load_v[2]==0.0
*define/e load_w[2]==0.0e+00
*define/i fin_diff[2]==0
*define/i ntel[2]== 1
*define/i nsubl[2]==1
.
[xqt opti
load_ratio
initialize ldi=1
end
stop
```

Fig. C.2 – (Cont'd).

```
[xqt tab
*call MESH_JLOCL
*call BNDYL
[xqt AUS
TABLE(NI=16,nj=1):  OMB DATA 1 1  .  Table of material properties
I=1,2,3,4,5,6,7,8,9,10,11,12,13,14,15
J=1:  10.0e+06 0.3 10.0e+06 3.8462e+06 3.8462e+06  >
3.8462e+06 .0 .0 1.55e-05 >
.01330 .01270 0.01355 0.01184 0.003386 0.01355
.
TABLE (NI=3,NJ=1,itype=0):  SUB LAM 1 1
J = 1 :  1 0.1 0.0
.
*open 3 EX321R.L01
[xqt dcu
copy 1 3 JLOC BTAB 2 5
stop
*close 3
[xqt bdlm
*put 1 BLD.LAM.1.1
build=1 using=1
stop
[xqt LAU
*call MESH_CONL
*call ES ( function = 'DEFINE FREEDOMS'; --
es_proc = <es_proc>; --
es_name = <es_name[1]>; --
es_pars = <es_pars[1]> )
[xqt E
[xqt RSEQ
reset maxcon=75
[xqt TOPO
reset maxsub = 60000
reset lramap = 9000
.
[xqt opti
ddvr
dv=1 thickness  sectionnumber=1  plynumber=1 in= 0.01,1.0
save THIRD_WORD=2
end
```

Fig. C.2 – (Cont'd).

```
constraint
define pointstrain=1 integ_pt=9  --
value1t=0.002 value1c=0.002 --
value2t=0.002 value2c=0.002 value12=0.005 --
type=EX97 group=1 --
element=69
save THIRD_WORD=2
end
stop
.
.  don't need kmap and amap in library 2
*delete 1 KMAP..*.*
*delete 1 AMAP..*.*
.
[xqt DCU
copy 1 2
stop
*enable 1 KMAP..*.*
*enable 1 AMAP..*.*
*close 2
.
.  Need to copy the definition of the
.  optimization problem in master library
*open 3 EX3.L01   .  This is the master library
[xqt DCU
copy 1 3 PSTR CONS 2 1
copy 1 3 PCON EVAL 2 1
stop
.
.  End of model dependent definitions
.
*close 3
*open 1 EX3.L01
.  setting up the coordination problem
[xqt CRDN
initialize
from_model=1
to_model=2
.             model 1     model 2
dv=1         thickness sectionnumber=1 plynumber=1
save
end
stop
```

Fig. C.2 – (Cont'd).

```
.
[xqt TB20
initialize /modify
modify /itrmop=2 .       itrmop=2
modify /itrmst=2 .  itrmst=1
modify /iscal=0
modify /jtmax=50 .           jtmax = 50
modify /delobj=0.01
modify /delstr=0.01
modify /rmvlmz=0.20
stop
[xqt TB20
OPTIMIZE
stop
.
.
.  Start the iterative process:  Analysis <-> Design
.
*call des_ana_iter ( ldi          = 2; --
numb_models = <numb_models>; --
maxiter     = <maxiter>; --
filename     = <filename>)
[xqt exit
\*EOI*
```

Fig. C.2 – (Concluded).

Vitae

Guy Gendron was born in Rivière-du-Loup, Canada on February 9, 1962. He studied Civil Engineering at Université Laval, Québec City, Canada where he obtained his B.S. and master's degree in 1985 and 1987, respectively. After he graduated from his master's degree, he worked for two years for TAO Simulations Inc. He then attended the Engineering Science and Mechanics Department at Virginia Polytechnic Institute and State University where he was a Graduate Research and Teaching Assistant. After completing his Ph. D. in Fall 1991, he will take a position with Spar Aerospace, in Ste-Anne de Bellevue, Québec, Canada.